5-2019

Ediacaran Depositional Age and Subsequent Fluid-Rock Interactions in the Mutual and Browns Hole Formations of Northern Utah

Ashley W. Provow
Utah State University

EDIACARAN DEPOSITIONAL AGE AND SUBSEQUENT FLUID-ROCK INTERACTIONS IN THE MUTUAL AND BROWNS HOLE FORMATIONS OF NORTHERN UTAH

by

Ashley W. Provow

A thesis submitted in partial fulfillment
of the requirements for the degree

of

MASTER OF SCIENCE

in

Geology

Approved:

_____	_____
Dennis Newell, Ph.D.	Alexis Ault, Ph.D
Major Professor	Committee Member
_____	_____
Carol Dehler, Ph.D.	Kevin Mahan, Ph.D.
Committee Member	Committee Member

_____
Richard Inouye, Ph.D.
Vice Provost School of Graduate Studies

UTAH STATE UNIVERSITY
Logan, Utah

2019

ABSTRACT

Ediacaran depositional age and subsequent fluid-rock interactions in the Mutual and Browns Hole formations of northern Utah

by

Ashley W. Provow, Master of Science

Utah State University, 2019

Major Professor: Dr. Dennis L. Newell
Department: Geology

Constraining the depositional age of Neoproterozoic stratigraphy in western North America has implications for correlating global glaciation and tectonic events. The depositional ages of the Neoproterozoic Mutual and Browns Hole formations of northern Utah are uncertain, constrained by two conflicting datapoints. However, new U-Pb geochronological data from 95 detrital apatite grains refines the maximum depositional age of the volcanic member of the Browns Hole Formation to 613 ± 12 Ma (2σ). This places new restrictions on the time available for the deposition of underlying units. Due to debate regarding the age models for underlying stratigraphy, two scenarios are explored that result in sediment accumulation rates of ~38 mm/kyr or ~64 mm/kyr. These results highlight a need for further exploring regional unconformities.

Evidence for several post-depositional diagenetic events are observed in the Mutual and Browns Hole formations. Cross-cutting relationships identified via petrography, scanning electron microscopy, and electron microprobe analysis show at least seven diagenetic events: (1) early grain-rimming hematite cement, (2) quartz

overgrowth and cement development, (3) feldspar dissolution, (4) phosphate dissolution, (5) partial quartz dissolution, (6) authigenic mineral precipitation including clays, sericite, monazite, and apatite cement, and (7) later hematite cementation. Constraining the timing of these events is challenging due to a paucity of datable material. Using basic geochemical modeling in PHREEQC and consideration of expected mineral formation conditions, a paragenetic sequence is placed into context of the known geologic history. Early hematite and development of quartz overgrowths and cements are coincident with early burial diagenesis soon after deposition. Feldspar dissolution and hydrolysis to clays and sericite is protracted through most of the burial history and likely escalate during pulses of saline fluid infiltration corresponding with formation of the Oquirrh basin. Saline fluids also dissolve and alter detrital phosphates, like monazite and apatite. Continued feldspar dissolution and burial heating create conditions favorable to partial quartz dissolution. Lastly, cooling via exhumation during the Sevier-Laramide Orogenies and growth of the Wasatch Anticlinorium allow authigenic minerals, including clays, monazite, and apatite and hematite cements, to precipitate from solution.

(94 pages)

PUBLIC ABSTRACT

Ediacaran depositional age and subsequent fluid-rock interactions in the Mutual and Browns Hole formations of northern Utah

Ashley W. Provow

Constraining the depositional age of Neoproterozoic stratigraphy in western North America has implications for correlating global glaciation and tectonic events. The depositional ages of the Neoproterozoic Mutual and Browns Hole formations of northern Utah are controlled by two conflicting datapoints. However, new U-Pb geochronological data from 95 detrital apatite grains refines the maximum depositional age of the volcanic member of the Browns Hole Formation to 613 ± 12 Ma (2σ). This places new restrictions on the time available for the deposition of underlying units. Due to debate regarding the age models for underlying stratigraphy, two scenarios for sediment accumulation rates are explored. These results highlight a need for further exploring regional unconformities.

Evidence for several post-depositional fluid-rock interaction events are observed in the Mutual and Browns Hole formations. Cross-cutting relationships identified via petrography, scanning electron microscopy, and electron microprobe analysis show at least seven fluid mediated events: (1) early grain-rimming hematite cement, (2) quartz overgrowth and cement development, (3) feldspar dissolution, (4) phosphate dissolution, (5) partial quartz dissolution, (6) authigenic mineral precipitation including clays, sericite, monazite, and apatite cement, and (7) later hematite cementation. Constraining the timing of these events is challenging due to a limited of datable material. Using basic

geochemical modeling and consideration of expected mineral formation conditions, a paragenetic sequence is placed into context of the known geologic history.

CONTENTS

Page

LIST OF TABLES

LIST OF FIGURES

INTRODUCTION

Neoproterozoic rocks record major tectonic, climatic, and biologic events in Earth's history, which include the timing and duration of Laurentian rifting from Rodinia, as well as global glaciations and the proliferation of multicellular life (Hoffman et al., 2017; Li et al., 2008). However, regional and global correlations of these events are challenging, particularly on the western margin of Laurentia, due to a paucity of detailed geochronology in rocks with limited datable material (e.g. Yonkee et al., 2014; Mahon et al., 2014; Smith et al., 2015; Dehler et al., 2017). Improving the chronology of sedimentary rocks from this time period is necessary for evaluating regional and global stratigraphic correlations, which are the backbone for testing models for Neoproterozoic events.

Climatic and tectonic events of the middle Neoproterozoic provided accommodation space for the preservation of regionally expansive, thick sedimentary packages of glacial sediments, siliciclastic rocks, and some volcanic material (Christie-Blick and Levy, 1989; Crittenden Jr and Wallace, 1973; Li et al., 2008; Shields-Zhou, Graham et al., 2016; Yonkee et al., 2014). The Brigham Group of southeast Idaho-northern Utah represents a one of these sedimentary packages and is key for improving regional correlations along the western Laurentian margin because it contains potentially dateable volcanic material. The Brigham Group is a thick package (>3 km) of quartzite, siltstone, conglomerate, and volcanic rocks (Fig. 1; Christie-Blick et al., 1988; Levy et al., 1994; Yonkee et al., 2014). These units are underlain by sequences of rocks (e.g., diamictites and cap carbonates) assigned to global glaciations (Snowball Earth) with temporal constraints provided by zircons from interbedded tuffs and other clastic units

(Figs. 2; 3; Fanning and Link, 2004; Balgord et al., 2013). However, new sedimentological and geochronological data suggest that the existing age models may require reinterpretation (Isakson, 2017; Isakson et al., in review). Additionally, some locations of the upper Brigham Group contain a volcaniclastic unit that yields sparse geochronology with conflicting results (Figs. 2; 3b; Crittenden Jr and Wallace, 1973; Christie-Blick and Levy, 1989; Verdel, 2009).

Here, we target the Mutual and Browns Hole formations located near Huntsville, UT (Figs. 1; 3b) to better understand the depositional and post-depositional history of these units. We integrate geochronologic and geochemical data, focusing primarily on the volcanic member of the Browns Hole Formation. Data from detrital apatite U-Pb geochronology are used to improve the age model of the Brigham Group and explore the implications of this new depositional age surrounding the interpretation of related regional strata and Laurentian rifting. Additionally, field observations, thin section microscopy, and electron microprobe analysis (EMPA) on authigenic monazite are used to present evidence for post-depositional fluid-rock interaction and construct a relative paragenetic sequence in the context of the known geological history.

GEOLOGIC SETTING

Laurentia, or the North American craton, was shaped by tectonic and climatic processes throughout the Neoproterozoic. By ca. 900 Ma most known continental land masses assembled around Laurentia (Hoffman, 1991) to form the supercontinent Rodinia (Li et al., 2008). Break-up of Rodinia initiated ca. 870 Ma (Dalziel and Soper, 2001; Paulsson and Andreasson, 2002; Li et al., 2003), but did not affect western Laurentia until the Gunbarrel event at ca. 780 Ma (Harlan et al., 2003). Laurentia fully separated from the Amazonia and Rio de la Plaza cratons (Cawood et al., 2006) and the assembling supercontinent, Gondwanaland, by ca. 590 Ma (Fitzsimons, 2003; Meert, 2003; Boger and Miller, 2004; Jacobs and Thomas, 2004; Collins and Pisarevsky, 2005; Cawood et al., 2006).

At least two global glaciations (Snowball Earth) occurred during the Neoproterozoic (Fig. 2; i.e. Rooney et al., 2014 and references within). These include the Sturtian glaciation (~720 – 660 Ma; Hoffman and Li, 2009) and the subsequent Marinoan glaciation (~650 – 635 Ma; Levy et al., 1994). These tectonic and glaciation events worked in concert to create accommodation space for thick packages of Neoproterozoic sedimentary rocks that are the focus of this study.

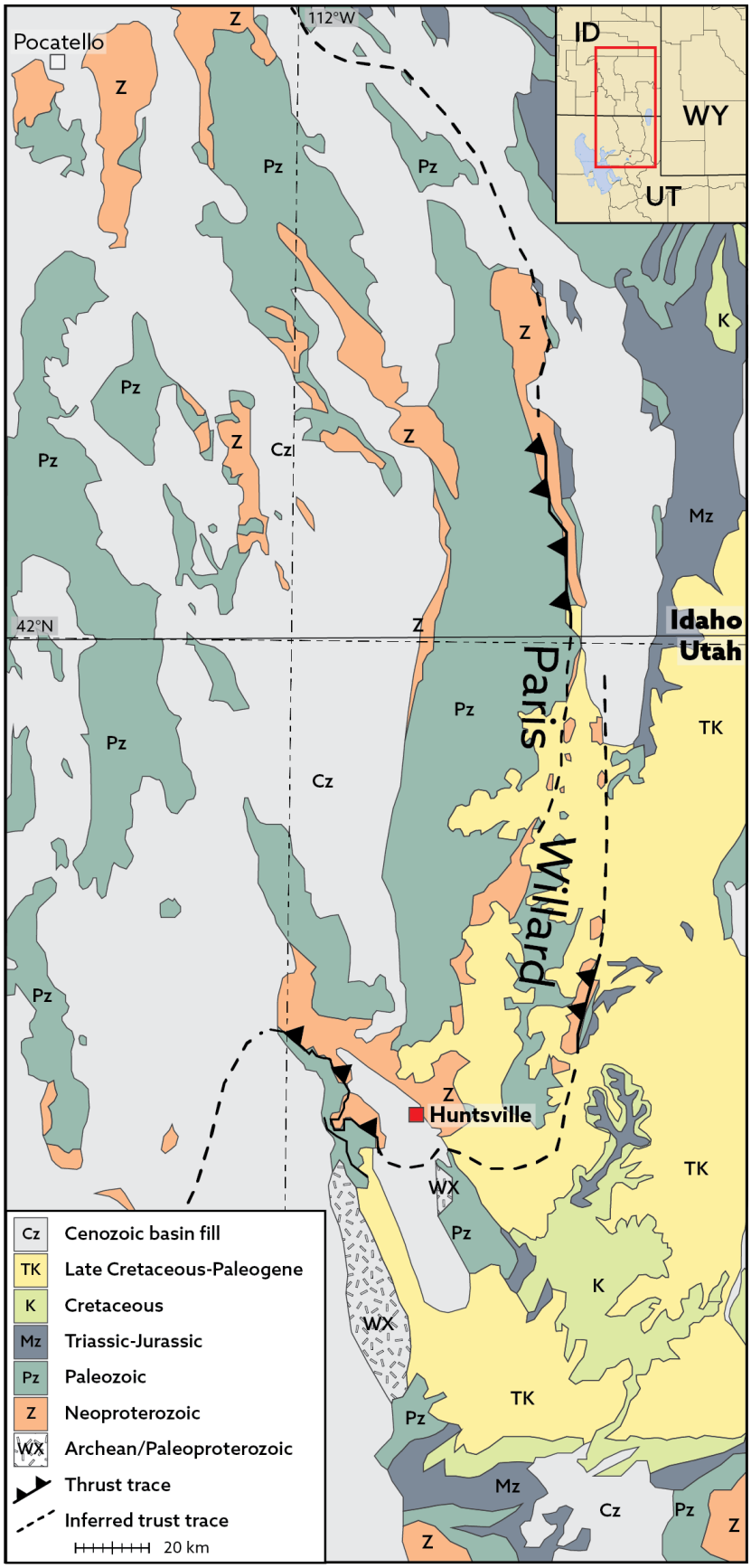

Figure 1. Generalized regional geologic map. Locations of stratigraphic column in Figure 3 are marked with grey box; box for the location of the study area has a red fill. Modified from Yonkee et al. (2014) and Yonkee and Weil (2015).

Stratigraphy

Neoproterozoic sedimentary rocks preserved along the western margin of Laurentia comprise diamictites, marine shales and carbonates, and fluvial clastic and volcaniclastic rocks. In southeastern Idaho, the base of the Neoproterozoic section is represented by the Scout Mountain Member of the Pocatello Formation. This unit contains ≤800 m of quartz-, arkosic-, and lithic-arenites along with argillite, clast supported conglomerates, at least two diamictites, and minor limestone and dolostone. This grades upwards into the informal upper member of the Pocatello Formation, a >600 m thick laminated argillite with sandy beds (Dehler et al., 2011). The upper member of the Pocatello Formation also contains a ~1 m thick pink dolostone that is in sharp contact with the underlying diamictite (Link, 1982) and thickens southward (Figs. 2; 3a; Dehler et al., 2011).

In northern Utah, correlative units include the Perry Canyon, Maple Canyon, and Kelley Canyon formations. The Perry Canyon Formation contains diamictites that are <120 m thick and directly overly Proterozoic crystalline basement. The diamictite is overlain by the <460 m thick informal greywacke member (Sorensen and Crittenden, 1979). The Perry Canyon Formation contains a ~10 m thick pink dolostone that overlies sandstone interpreted to be a reworked diamictite in other parts of northern Utah (Dehler et al., 2012). The Maple Canyon and Kelley Canyon formations are correlative with the informal upper member of the Pocatello Formation in southern Idaho. The Maple Canyon Formation comprises <450 m of fluvial olive argillite, fine grained green arkose, and interbedded conglomerates and quartzites. This is overlain by Kelley Canyon Formation, ~600 m of marine argillite, minor carbonates, and shales (Figs. 2; 3b; Crittenden et al.,

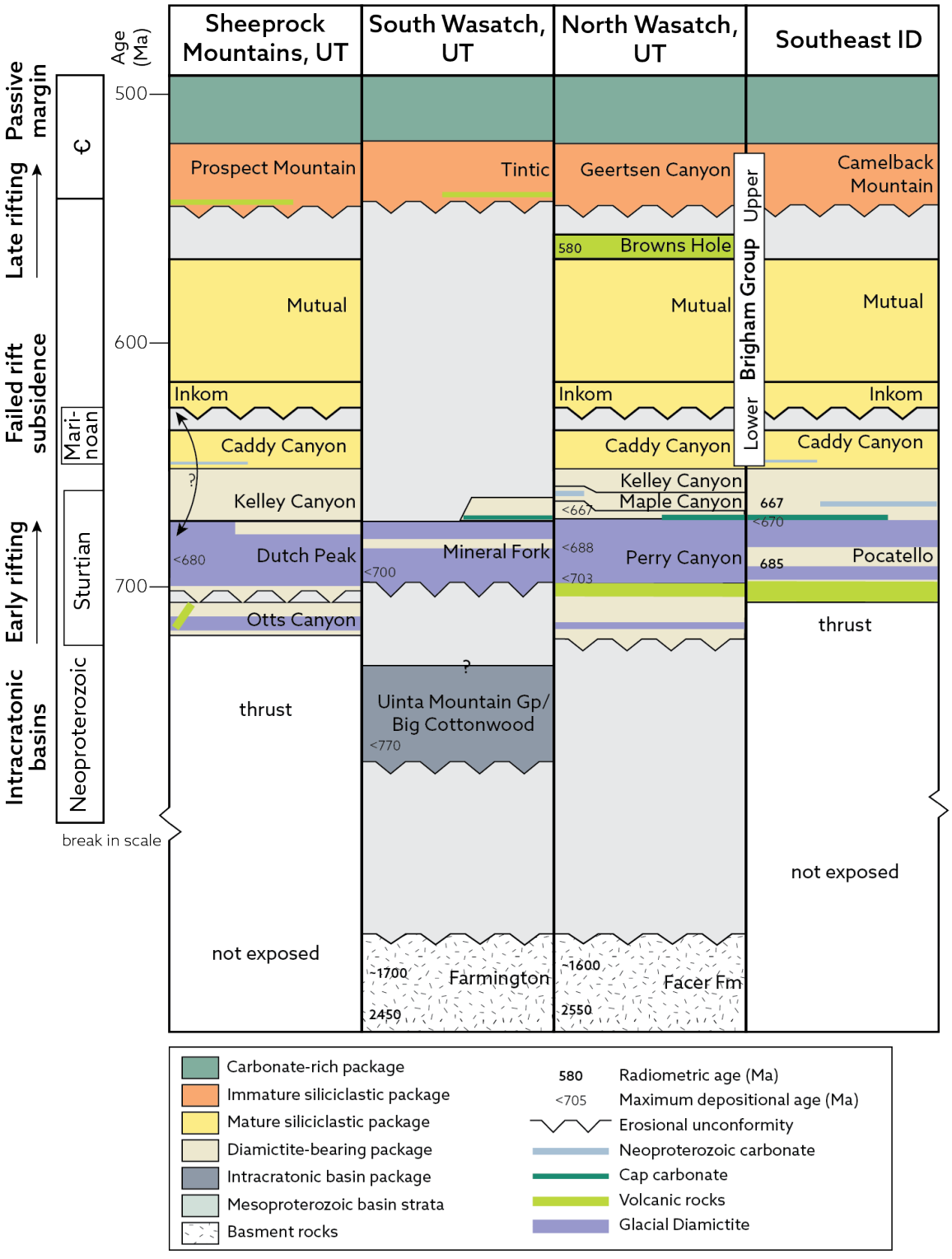

Figure 2. Wheeler diagram with relevant representative stratigraphic sections from around North America. Figure is modified from Yonkee et al. (2014).

1971). These units were likely deposited in a glacier-fed basin (Stewart, 1972; Link, 1982) created by the northward rifting of the South China Craton from Laurentia (Li et al., 2003).

The Brigham Group, a mature siliciclastic sequence of fluvial, shallow marine, and offshore marine strata, overlies the Kelly Canyon and Pocatello formations (Christie-Blick et al., 1988; Yonkee et al., 2014). The Caddy Canyon Formation is the base of the Brigham Group and composed of <760 m of quartzite and siltstone deposited in a nearshore marine, braided delta, or braided fluvial system. The Inkom Formation unconformably overlies the Caddy Canyon Formation and comprises <150 m of siltstone deposited in a low-energy marine environment (Crittenden et al., 1971; Christie-Blick, 1982; Levy et al., 1994; Yonkee et al., 2014). The base of the Inkom Formation is characterized by paleovalleys filled with <60 m of pebble conglomerate that cut into the underlying Caddy Canyon Formation (Levy et al., 1994). The overlying Mutual Formation is >360 m of pink to red fluvial and shallow marine quartzite (Figs. 2; 3; Crittenden et al., 1971; Crittenden, 1972a; Christie-Blick, 1982; Levy et al., 1994; Yonkee et al., 2014). In northern Utah, the Browns Hole Formation locally overlies the Mutual Formation. This unit is informally divided into two members, the lower volcanic member and the upper Terracotta quartzite member. The volcanic member is <140 m of dark red to purple volcaniclastic sediments and mafic-volcanic flows. Importantly, the presence of volcanically-derived sediment and volcanic flows provide age control for this otherwise relatively poorly constrained sequence of the ~1400 m of sedimentary rocks that comprises the Brigham Group (Crittenden, 1972a). The Terracotta quartzite member is ≤45 m of “terracotta colored” hematite-cemented quartzite, interpreted as fluvial in

origin (Christie-Blick and Levy, 1989). The Brigham Group is capped by the ~550 m thick Geertsen Canyon Formation, a shallow marine to fluvial, conglomeratic coarse sandstone unit (Crittenden, 1972a). Near Huntsville, UT, the contact with the underlying Browns Hole Formation is covered but marked by a significant influx of feldspar grains (Figs. 2; 3b). In Idaho, the base of the Camelback Mountain Formation, correlative with Geertsen Canyon, is marked by an approximately 60-m-deep paleovalley cut into the Mutual Formation, which is interpreted to represent a stratigraphic sequence boundary (Figs. 2; 3a; Christie-Blick and Levy, 1989; Levy et al., 1994; Yonkee et al., 2014).

Age Model

The lack of material for absolute age control makes constraining the age and stratigraphic correlations within later Neoproterozoic rocks in western Laurentia challenging. Young zircons from volcanic tuffs and volcaniclastic-rich diamictites in the Scout Mountain Member of the Pocatello Formation (southern Idaho) yield a U-Pb age of ~710 - 660 Ma, indication that the lower diamictite correlates with Sturtian glaciation (Figs. 2; 3a; Keeley et al., 2012; Yonkee et al., 2014; Isakson, 2017; Isakson et al., in review). Zircons from a tuff bed in the upper Scout Mountain Member, above the upper diamictite, yield a U-Pb date of 667 ± 5 Ma. This date was interpreted as an absolute age, suggesting that the second diamictite is also associated with Sturtian glaciation (Fanning and Link, 2004). In Utah, correlative volcanic rocks below and within the upper diamictite of the Perry Canyon Formation yield young detrital zircon populations with U-Pb ages of 706 ± 6 Ma and 667 ± 5 Ma, respectively. These zircon age populations suggest that this diamictite is also related to Sturtian glaciation (Figs. 2; 3b; Balgord et al., 2013).

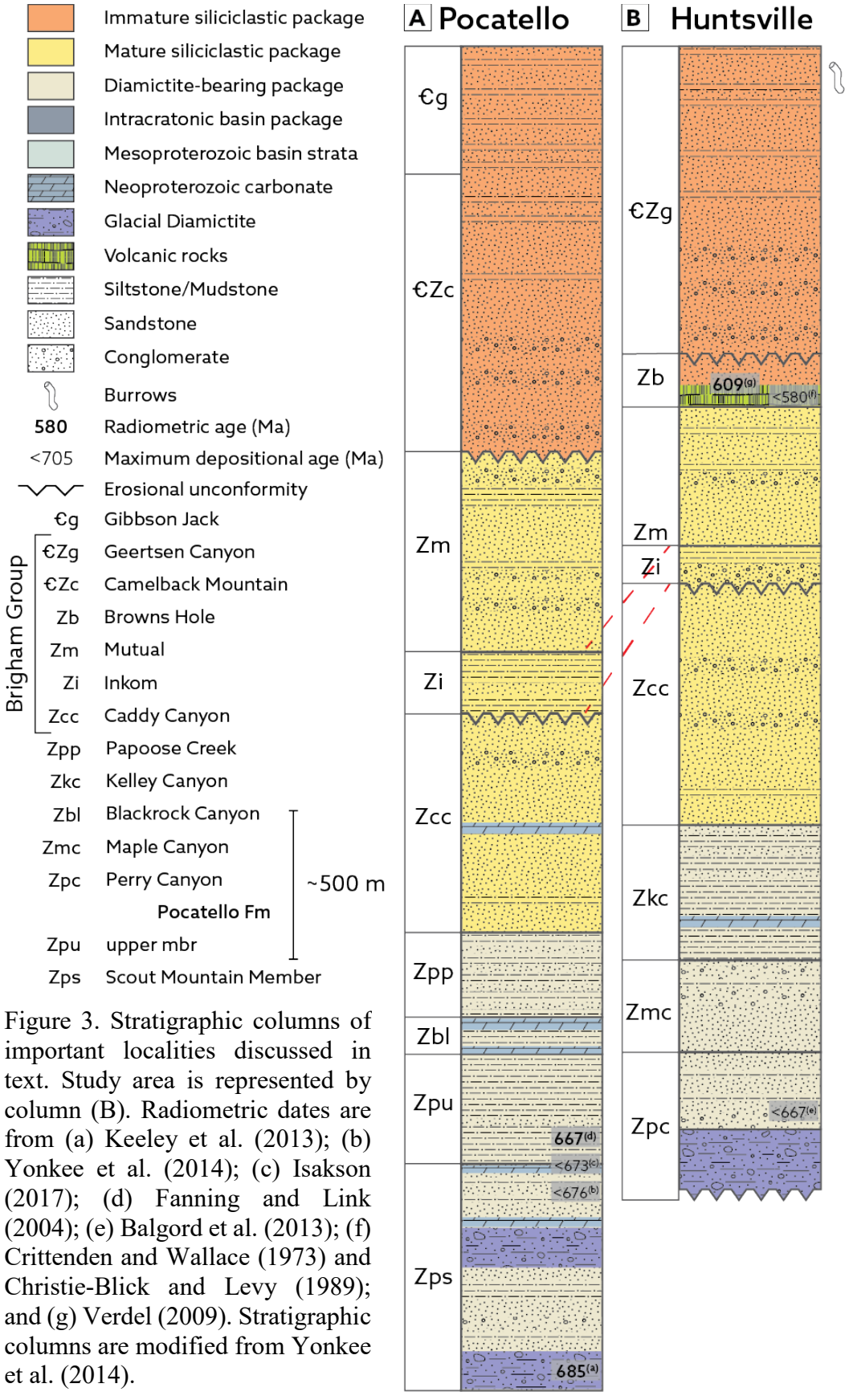

Figure 3. Stratigraphic columns of important localities discussed in text. Study area is represented by column (B). Radiometric dates are from (a) Keeley et al. (2013); (b) Yonkee et al. (2014); (c) Isakson (2017); (d) Fanning and Link (2004); (e) Balgord et al. (2013); (f) Crittenden and Wallace (1973) and Christie-Blick and Levy (1989); and (g) Verdel (2009). Stratigraphic columns are modified from Yonkee et al. (2014).

Tying diamictites and other glacial features to the later Marinoan glaciation is challenging due to limited datable material. However, new U-Pb zircon geochronology from the volcanic tuff in the upper Scout Mountain Member (e.g. Fanning and Link, 2004) and the reinterpretation as a reworked unit suggests that this unit has a maximum depositional age of ≤673 Ma (Isakson, 2017; Isakson et al., in review). Isakson (2017) posits that the underlying diamictite could therefore be much younger and related to Marinoan glaciation, instead of Sturtian glaciation as Fanning and Link (2004) interpreted. Additionally, chemo- and lithostratigraphic characteristics of the cap-like carbonates overlying the upper diamictites in these units, such as laminated pink dolostone and negative δ13C excursions, strongly resemble those definitively linked with the Marinoan glaciation (Fig. 3a; Hoffmann et al., 2004; Condon et al., 2004; Dehler et al., 2011, 2012).

Absolute age control for the Maple Canyon and Kelly Canyon formations and Brigham Group is limited due to little volcanic material, but some interpretations have been made based on stratigraphy. The paleovalleys at the base of the Inkom Formation are interpreted to represent a sequence boundary related to sea level fluctuations during Marinoan glaciation (Fig. 2; Levy et al., 1994). Existing geochronology for the Brigham Group is restricted to the volcanic member of the Browns Hole Formation. A hornblende from a volcanic clast in an agglomerate, located approximately 40 m above the base of the Browns Hole - Mutual contact near Huntsville, UT, yields a bulk $^{40}Ar/^{39}Ar$ date of 580 ± 7 Ma (Crittenden Jr and Wallace, 1973; Christie-Blick and Levy, 1989). A thin basalt flow located several meters above the agglomerate in this location yields an apatite U-Pb date of 609 ± 25 Ma (Fig. 3b; Verdel, 2009). This juxtaposition of younger dates

below older dates is problematic for interpreting the timing of deposition for the Browns Hole volcaniclastics and related strata. Finally, the Cambrian-Precambrian boundary lies within the upper member of the Geertsen Canyon, ~480 m above the contact with underlying units, evident in presence of trace fossils *Skilithus* and *Plagiomus* (Figs. 2; 3b; Crittenden et al., 1971; Peterson and Clark, 1974; Link et al., 1987).

Post-Deposition

After deposition, the Brigham Group and underlying strata experienced ≤10 km of burial from the Cambrian to Early Cretaceous. The sedimentary wedge that comprises the Brigham Group and the strata above and below, was exhumed during the Sevier and Laramide orogenies (ca. 140 – 50 Ma; Yonkee and Weil, 2015). The Sevier and Laramide orogenies were a result of the protracted accretion of microterranes and the subsequent subduction of the Farallon oceanic plate beginning in the Jurassic and lasting into the Paleogene (DeCelles, 2004; Yonkee and Weil, 2015). In the Early Cretaceous, this package of rocks was displaced approximately 60 km eastward within the Paris-Willard thrust sheet (Fig. 1; Crittenden, 1972b; Yonkee, 2005). Tilting and ongoing east-vergent thrusting during the growth of the Wasatch anticlinorium during the Paleogene marks the transition from the mostly shallower western thrusts of the Sevier Orogeny to the eastern basement cored uplifts of the Laramide (Yonkee, 1992). Beginning in the Neogene, Basin and Range extension initiated as an isostatic response to crustal thickening after the Sevier-Laramide orogenies (Dickinson, 2002). Normal faulting along the Wasatch Fault Zone caused by extensional processes tilted and exhumed footwalls to finally expose Neoproterozoic sedimentary and underlying basement rocks in a range of structural contexts (Yonkee et al., 2014).

SAMPLES AND METHODS

We obtained 21 samples along an approximately 150 m wide and 230 m long stratigraphic transect from the upper Mutual Formation to the base of the Geertsen Canyon Formation in Huntsville, UT (Figs. 1; 4). Using field mapping and stratigraphic descriptions as a framework, samples were collected in a semi-regular interval to include a wide range of representative rock types. Thin sections for 11 of the 21 samples were prepared with microprobe polish for petrographic and potential EMPA. Thin sections were selected with emphasis placed on samples from key outcrops representing contacts between units and locations that had macroscopic evidence of fluid-related alteration.

Chemical analysis of monazite [$(Ce,La)PO_4$] using EMPA was conducted on eight samples at the Electron Microprobe Laboratory at University of Colorado Boulder. Thin sections were coated in Al prior to EMPA for increased conductivity, precision, and accuracy. Quantitative analyses were completed using a JEOL JXA-8230 Superprobe with five wavelength dispersive spectrometers (WDS) and a detection limit of ~10 ppm or better. Whole thin section WDS maps for P$K\alpha$, La$L\alpha$, Y$L\alpha$, and Si$K\alpha$ were used to locate monazite. Four samples contained sufficient monazite for further spot EMPA on individual grains: AP17_66MF_4, AP17_66MF_5, AP17_66MF_7, and AP17_66MF_11. Potential grains were located using back scattered electron (BSE) imagery and verified for composition using spot analysis with energy dispersive X-ray spectroscopy (EDS) by allowing the counter to collect data for several seconds until composition could be confidently determined. Concentrations of common and rare earth elements (REE) were acquired for each grain by analyzing two to five spots per grain, depending on grain size and texture, with a LaB6 electron gun with a beam size of 0.2 to

0.7 μm at 15 kV for up to 160 seconds per spot. The monazite consistency standard used during analyses was the Moacyr monazite from eastern Brazil (Gonçalves et al., 2016).

To provide better depositional age constraints for the volcanic member of the Browns Hole Formation, U, Th, and Pb-bearing accessory phases were obtained from sample AP17_66MF_9 using standard crushing, sieving, density, and magnetic separation methods. Resulting mineral separates contained few zircons and abundant apatite; thus, apatite mineral separates were selected for U-Pb dating. Chips of the original sample were analyzed with the FEI Quanta FEG 650 scanning electron microscope (SEM) at the Utah State University Microscopy Core Facility to determine the lithological context of apatite separates. An Oxford EDS attachment was used to make composite element maps to determine the locations of apatite grains by focusing on locations with significant concentrations of P and Ca. Spot EDS analysis was also used to determine if any chemical differences existed that would indicate overgrowths or alteration rims.

Apatite U-Pb dating and cathodoluminescence (CL) imaging were completed at the University of Arizona LaserChron Center. Approximately 250 grains were poured and arranged on double stick tape to avoid bias that may be introduced during individual grain selection. Grains were mounted in epoxy and polished to their approximate mid-section and cleaned, similar to methods used for zircons (Gehrels et al., 2008). A subset of apatite crystals was analyzed for U and Pb using a Nu Plasma high resolution multi-collector laser ablation inductively coupled plasma mass spectrometer (LA-ICP-MS). LA-ICP-MS was done with a Photon Machines Analyte G2 excimer laser with a spot diameter of 30 μm for 15 seconds with 8 mJ output energy and pulse frequency of 7 Hz,

creating an ablation pit approximately 15 - 20 μm deep. Following LA-ICP-MS, CL images of apatite grains to evaluate apatite chemical zonation and locate mineral inclusions that may have interfered with spot analyses were acquired using a Gatan ChromaCL2 detector on a Hitachi 3400N SEM. Apatite standards used during analysis were the McClure Mountain and Madagascar apatite (Thomson et al., 2012). Apatite U-Pb data was corrected for common Pb using the $^{206}Pb/^{204}Pb$ data for 500 Ma of 17.915 (Stacey and Kramers, 1975). Final data reduction and calculations for Tera-Wasserberg concordia were completed using Isoplot (Ludwig, 2011) and RadialPlotter software (Vermeesch, 2009).

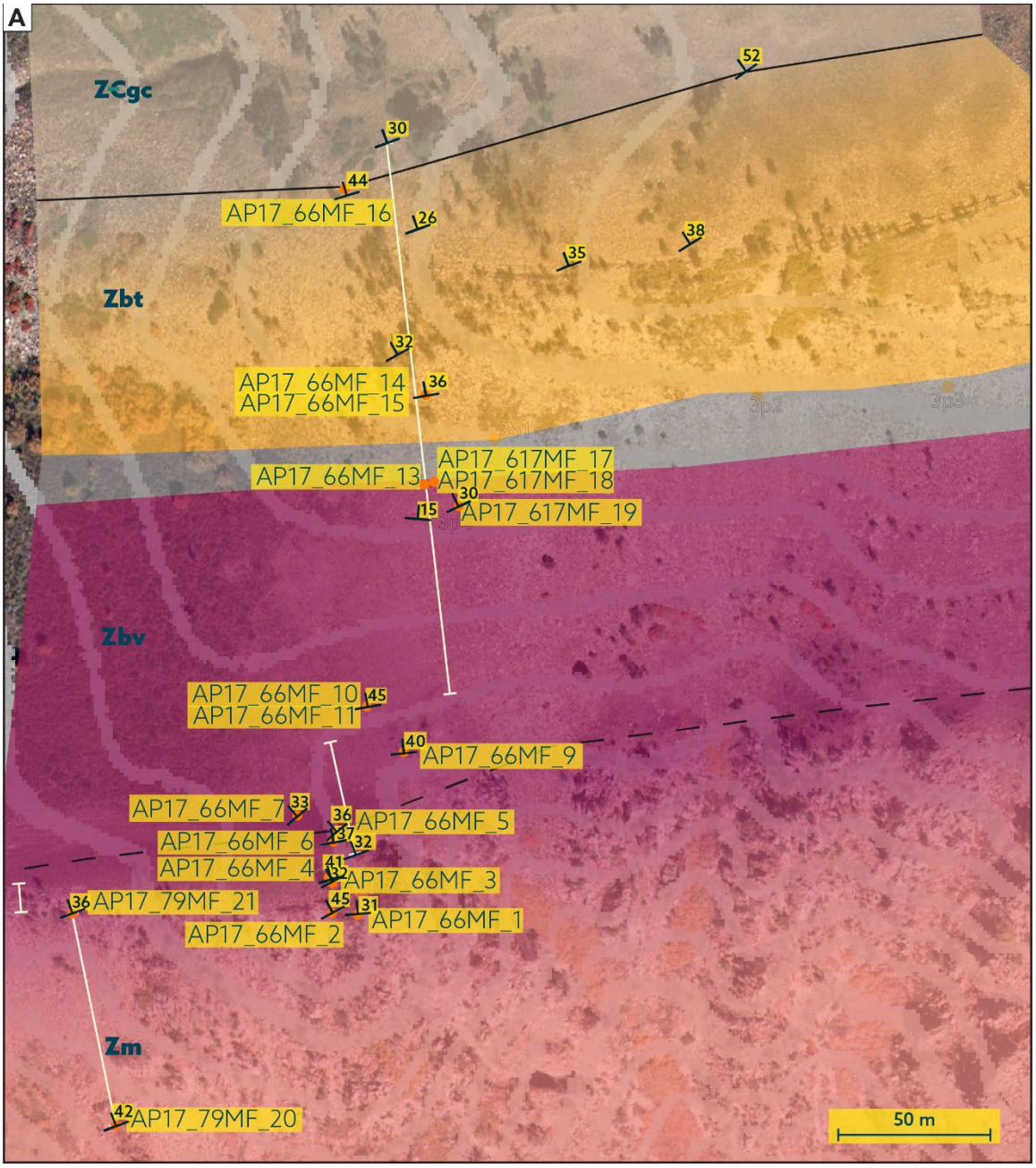

Figure 4. Field map and measured stratigraphic section. (A) Field map with locations of samples noted. Locations where section was measured are shown with white lines. (B) (following page) Full measured section with approximate sample locations indicated. (C) (following page) Zoom in on part of measured section where geochronological and geochemical samples were obtained. Dates in orange are of geochronology taken from this area: [1] hornblende bulk Ar-Ar date, Crittenden Jr and Wallace (1973) and Christie-Blick and Levy (1989); [2] apatite U-Pb date, Verdel (2009); [3] apatite U-Pb, this study.

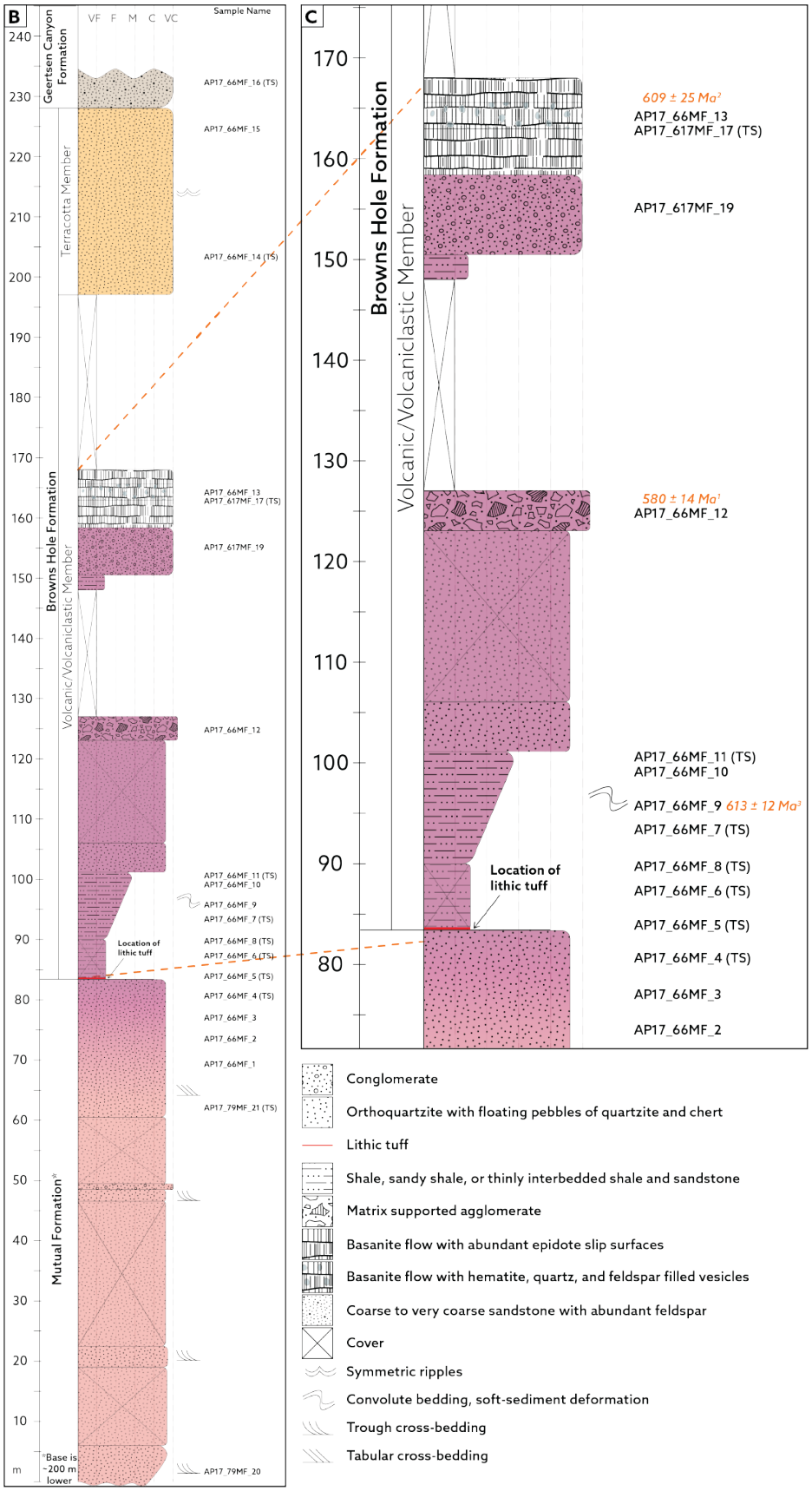
B
Sample Name
VF F M C VC
Geertsen Canyon Formation
Terracotta Member
Browns Hole Formation
Volcanic/Volcaniclastic Member
Mutual Formation*
AP17_66MF_16 (TS)
AP17_66MF_15
AP17_66MF_14 (TS)
AP17_66MF_13
AP17_617MF_17 (TS)
AP17_617MF_19
AP17_66MF_12
AP17_66MF_11 (TS)
AP17_66MF_10
AP17_66MF_9
AP17_66MF_7 (TS)
AP17_66MF_8 (TS)
AP17_66MF_6 (TS)
AP17_66MF_5 (TS)
AP17_66MF_4 (TS)
AP17_66MF_3
AP17_66MF_2
AP17_66MF_1
AP17_79MF_21 (TS)
AP17_79MF_20
Location of lithic tuff
*Base is ~200 m lower
m
C
Browns Hole Formation
Volcanic/Volcaniclastic Member
609 ± 25 Ma2
AP17_66MF_13
AP17_617MF_17 (TS)
AP17_617MF_19
580 ± 14 Ma1
AP17_66MF_12
AP17_66MF_11 (TS)
AP17_66MF_10
AP17_66MF_9 613 ± 12 Ma3
AP17_66MF_7 (TS)
AP17_66MF_8 (TS)
AP17_66MF_6 (TS)
AP17_66MF_5 (TS)
AP17_66MF_4 (TS)
AP17_66MF_3
AP17_66MF_2
Location of lithic tuff
Conglomerate
Orthoquartzite with floating pebbles of quartzite and chert
Lithic tuff
Shale, sandy shale, or thinly interbedded shale and sandstone
Matrix supported agglomerate
Basanite flow with abundant epidote slip surfaces
Basanite flow with hematite, quartz, and feldspar filled vesicles
Coarse to very coarse sandstone with abundant feldspar
Cover
Symmetric ripples
Convolute bedding, soft-sediment deformation
Trough cross-bedding
Tabular cross-bedding

RESULTS

Field Relationships

In the study area, the Mutual Formation is ~350 m (Crittenden, 1972a) of pink to dark pink, well cemented, medium to coarse grained quartzite with local chert and quartzite pebbles (Fig. 4). It contains thin pebbly channel fills and some crossbedding. Pebble channel fills become thicker and more abundant towards the top of the unit but the dominant grain size remains medium to coarse sand. Approximately one meter below the contact with the overlying Browns Hole Formation, this unit changes from pink to a dark purple-red that continues throughout the entire volcanic member of the Browns Hole Formation. Other workers have not described the nature of the contact between the Mutual and Browns Hole formations, but we have interpreted it as the location of a thin, 1 to 1.5 cm, gray-purple siltstone. This thin bed marks the change from well-cemented quartzite to the appearance of volcaniclastic sediments (Fig. 5a).

The volcanic member of the Browns Hole Formation consists of ~83 m of interbedded dark purple to red volcaniclastic siltstone, sandstone, and agglomerate that overall coarsens upward. Fine-grained beds usually contain laminations that sometimes appear convolute, indicating soft-sediment deformation (Fig. 5b). Sandstone beds locally contain long, flat intraclasts of finer-grained material aligned approximately parallel to bedding (Fig. 5c). Agglomerates are composed of rounded to subrounded clasts of primarily vesicular basalt and porphyritic andesite. Pebble- to cobble-sized clasts are supported by a coarse sandstone matrix composed of sand-sized quartz grains and volcanic grains of the same material as the larger volcanic clasts (Fig. 5d).

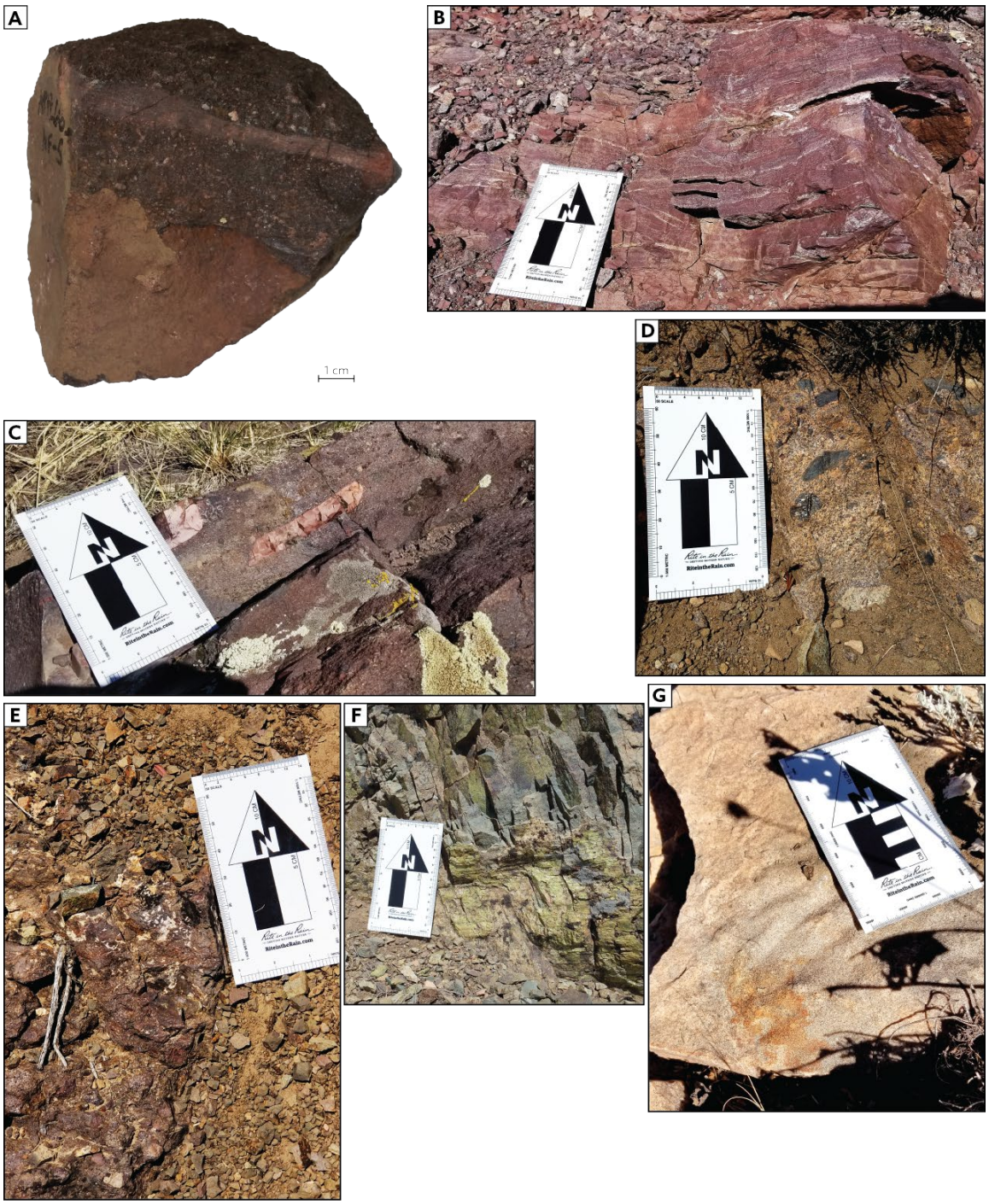

Figure 5 Field and hand sample photographs. (A) Hand sample representing the contact between the Mutual and Browns Hole formations. (B) Example of fine-grained convolute bedding. (C) Example of long, flat finer grained rip up clasts. (D) Example of agglomerate. (E) Outcrop representing the contact between the basalt and underlying sandstone. (F) Example of epidote coated slip surface on basanite flow. (G) Example of symmetrical ripples found on the top of some beds of the Terracotta member of the Browns Hole Formation.

The top of this unit is marked by a poorly-exposed basalt flow that is partially obscured by foliage and unconsolidated material but based on the last occurrence of basalt clasts along the hillside it is inferred to be ~10 m thick. Verdel (2009) used bulk geochemistry and determined that it compositionally qualifies as a basanite, a silica undersaturated basalt (Le Maitre et al., 1989), but for clarity and consistency with prior literature we will continue to use the term basalt. The basal contact of the basalt, where exposed, is with a coarse volcaniclastic sandstone. The contact is also characterized by irregular quartz and zeolite (likely analcime) veins, 0.5 - 1.0 cm-thick, lined with micron-scale specular hematite, that interfinger with the basalt and a siltstone (Fig. 5e). The basalt has several circular to sub circular shaped vesicular zones, no larger than ~0.33 m in diameter, with sub-cm-scale vesicles filled with quartz, plagioclase, and specular hematite. The remaining basalt surrounding the vesicular zones is massive with no evidence of sedimentary features like flow banding. Locally, the basalt has veins of epidote up to several mm-thick. Epidote up to several mm-thick is also associated with local slip surfaces (Fig. 5f).

The top of the basalt and contact between the Terracotta member and underlying volcanic member of the Browns Hole is covered throughout the study area. Based on the last occurrence of basalt clasts along the hillside, the overlying Terracotta member is ~50 - 60 m-thick. This unit is a coarse- to medium-grained, quartzite that is well-cemented with silica and hematite. Sedimentary features are limited to faint crossbedding and symmetric ripples (Fig. 5g). The Terracotta member of the Browns Hole Formation is visually similar to the overlying Geertsen Canyon Formation and can only be differentiated in this location by the high percentage of feldspar that is characteristic of

the basal Geertsen Canyon Formation.

Petrography

The Mutual Formation comprises moderately sorted, subrounded to subangular quartz grains with quartz overgrowths, rare sericitized feldspar, minor zircon, and few lithic grains. Where feldspar grains are present, they are often porous with fine-grained sericite filling pore spaces (Fig. 6b). Grains are variably cemented by hematite and clay (Fig. 6a). Hematite cement occurs as dust rims along relict grain boundaries and coats new boundaries created by quartz overgrowths (Fig. 6a-inset).

The interpreted contact between the Mutual and Browns Hole formations is a thin (1 - 1.5 cm) light purple-gray bed of siltstone. This band comprises dominantly angular quartz grains with pitted edges, which are lined with fibrous clay minerals (Fig. 6c-6e) and tabular monazite grains (Fig. 8a). Grains are supported by a matrix of anastomosing microcrystalline apatite (confirmed with SEM-EDS and EMPA), hematite, and lesser fine-grained clay and sericite cement (Fig. 6d, 6e). Stratigraphically above and below this siltstone, quartz grains are more rounded, less pitted, less frequently coated with fibrous clay, and more densely packed with less microcrystalline apatite cement (Fig. 6c). Volcanic grains, generally porphyritic andesite, are a component of the siltstone contact and contain fine-grained sericite and clay minerals that are pseudomorphic to feldspar grains (Fig. 6f). Few intact feldspar grains are found outside of volcanic clasts and, where present, are degraded with fine-grained sericite and clays in pore spaces (Fig. 6c). Accessory minerals include titanite (Fig. 6e) and barite.

Quartz, volcanic clasts, and hematite cement are the dominant constituents in the sandstones and siltstones of the volcanic member of Browns Hole Formation (Fig. 7a).

An ~5 m thick agglomerate bed contains a minor sandstone component and rounded volcanic lapilli with feldspar phenocrysts (Fig. 7b). The basalt flow capping the volcanic member of the Browns Hole Formation is locally vesicular. Most vesicles are filled with quartz and lined with specular hematite grains, ranging from ≤1 - 200 μm-long and 10 - 20 μm-thick, and anorthite laths ≤400 μm-long and 100 μm-thick (Fig. 7c). The groundmass of the basalt is dominantly calcium plagioclase, as revealed with EDS and WDS, with lesser amounts of augite and patches of irregular fine-grained clay and hematite (Fig. 7d).

The overlying Terracotta member is a quartz sandstone with some hematite cement. Quartz grains are moderately rounded with fractures that do not cross grain boundaries. As with other parts of the section, hematite cements tend to fill larger pore spaces, coat grain boundaries, and infiltrate fractures. Quartz overgrowths observed in this member form crude triple junctions between grains but, unlike the Mutual Formation, overgrowths do not preserve relict grain boundaries. Clay cement is conspicuously absent in this member (Fig. 7e).

Figure 6. Photomicrographs from the Mutual and Browns Hole formations. (A) Cross-polarized (XPL) image of Mutual Formation sample AP17_66MF_4, taken from near the contact with the Browns Hole Formation. Note the clay cements that infiltrates between grain boundaries. Note the hematite cement pooling in larger pore spaces and lining grain boundaries in both the main image and circular inset, plane-polarized light (PPL). Quartz overgrowths are also present. (B) XPL image of Mutual Formation sample AP17_79MF_21. Observe the fine-grained clays surrounding and within the feldspar grain, likely replacing the original grain, in the center of the image. (C) XPL image of sample AP17_66MF_5, which represents the contact between the Mutual and Browns Hole formations. Circular insets are PPL image of the same location, used to highlight the stippled texture of the apatite cement. Notice the pitting of quartz grains and amount of fibrous clay increases to the right, or towards the Browns Hole Formation. Also observe the abundant hematite cement that permeates between grains and pools in larger pore spaces, as well as the anastomosing apatite cement. Orange circle in both images shows the location of a partially dissolved feldspar grain that is being replaced by fine grained clays. (D) An XPL image of the same sample showing fibrous clay minerals, pitted quartz grains, and apatite cement in more detail. (E) Another XPL image of the same sample showing titanite grains and abundant apatite and hematite cements. Also regard the distinct lack of quartz grains compared the previous two images. (F) XPL image of a volcanic clast in the same sample with fine grained clays in the shape of feldspar laths. Q=quartz; fs=feldspar; hem=hematite cement; cl=clay cement; og=quartz overgrowths; dust rims=hematite dust rims; ap=apatite cement; t=titanite.

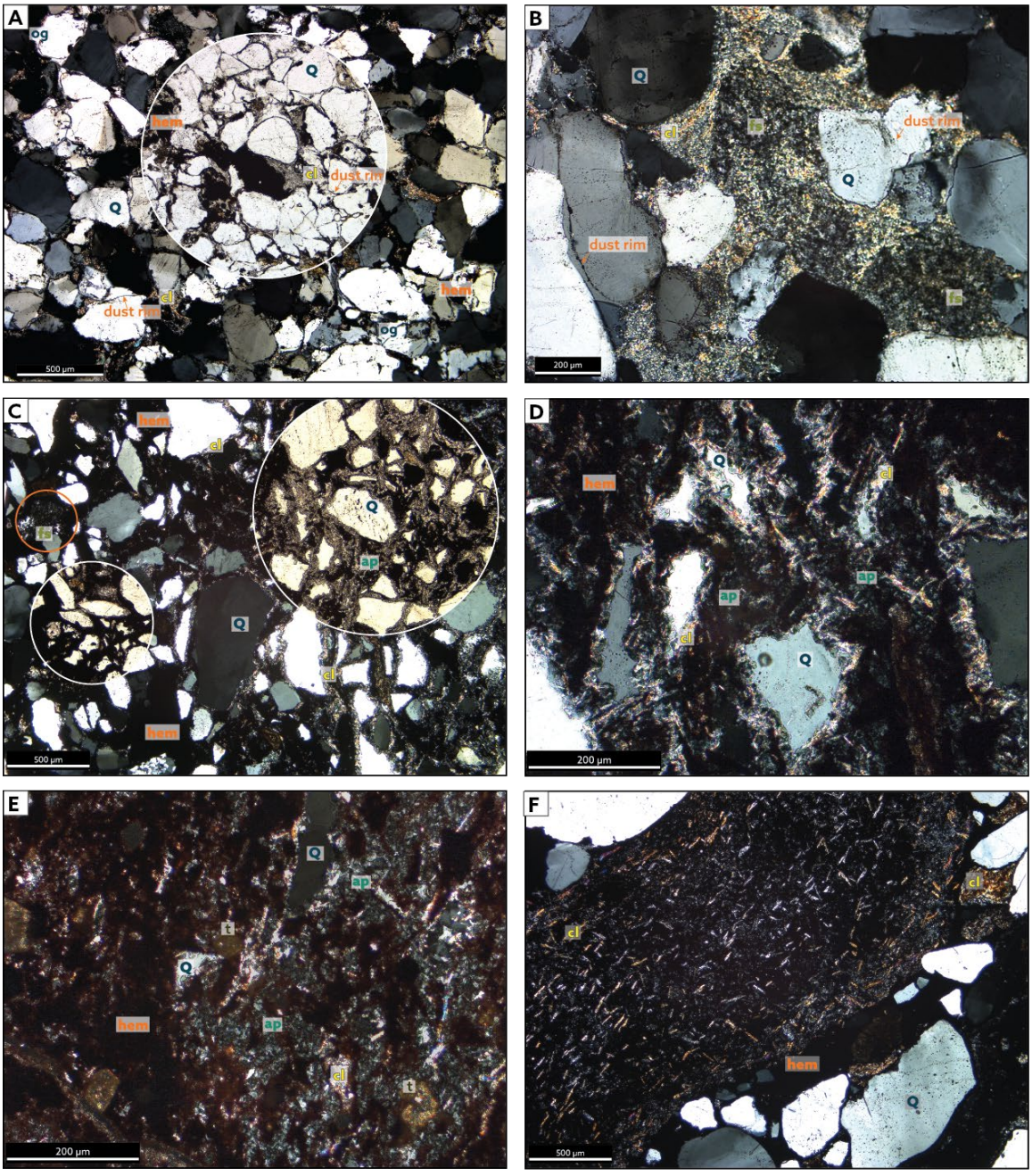
A
og
Q
hem
cl
dust rim
Q
cl
dust rim
hem
og
500 µm
B
Q
cl
fs
dust rim
Q
dust rim
fs
200 µm
C
hem
cl
Q
fs
ap
Q
cl
hem
500 µm
D
Q
hem
cl
ap
ap
cl
Q
200 µm
E
Q
ap
t
Q
hem
ap
cl
t
200 µm
F
cl
cl
hem
Q
500 µm

Figure 7. Photomicrographs from the Browns Hole Formation. (A) A PPL image of sample AP17_66MF_7, a volcaniclastic sandstone featured higher in the section. Note the overall rounding of quartz grains where not broken. Hematite and clay cements continue to be abundant. (B) PPL image of another volcaniclastic sandstone, sample AP17_66MF_8. Notice the presence of rounded lapilli clasts with feldspar phenocrysts. (C) PPL image of a quartz, feldspar, and hematite filled vesicle in sample AP17_617_17 taken from the basalt flow that caps the volcaniclastic member of the Browns Hole Formation. (D) XPL image from the same sample showing the feldspar groundmass being replaced by fine grained clays. Also note the presence of hematite pooling in pore spaces where clays do not, highlighted in the PPL circular inset. (E) PPL image of sample AP17_66MF_14 taken from the Terracotta member of the Browns Hole Formation, above the basalt flow. Observe the lack of a volcanic component, or clay cements, but still a significant amount of hematite cement. Note the lack of significant quartz overgrowths, highlighted in the circular XPL inset. Quartz grains are moderately rounded and most are heavily fractured; note that fractures do not continue across grain boundaries and are, therefore, likely not post-depositional compaction cracks.

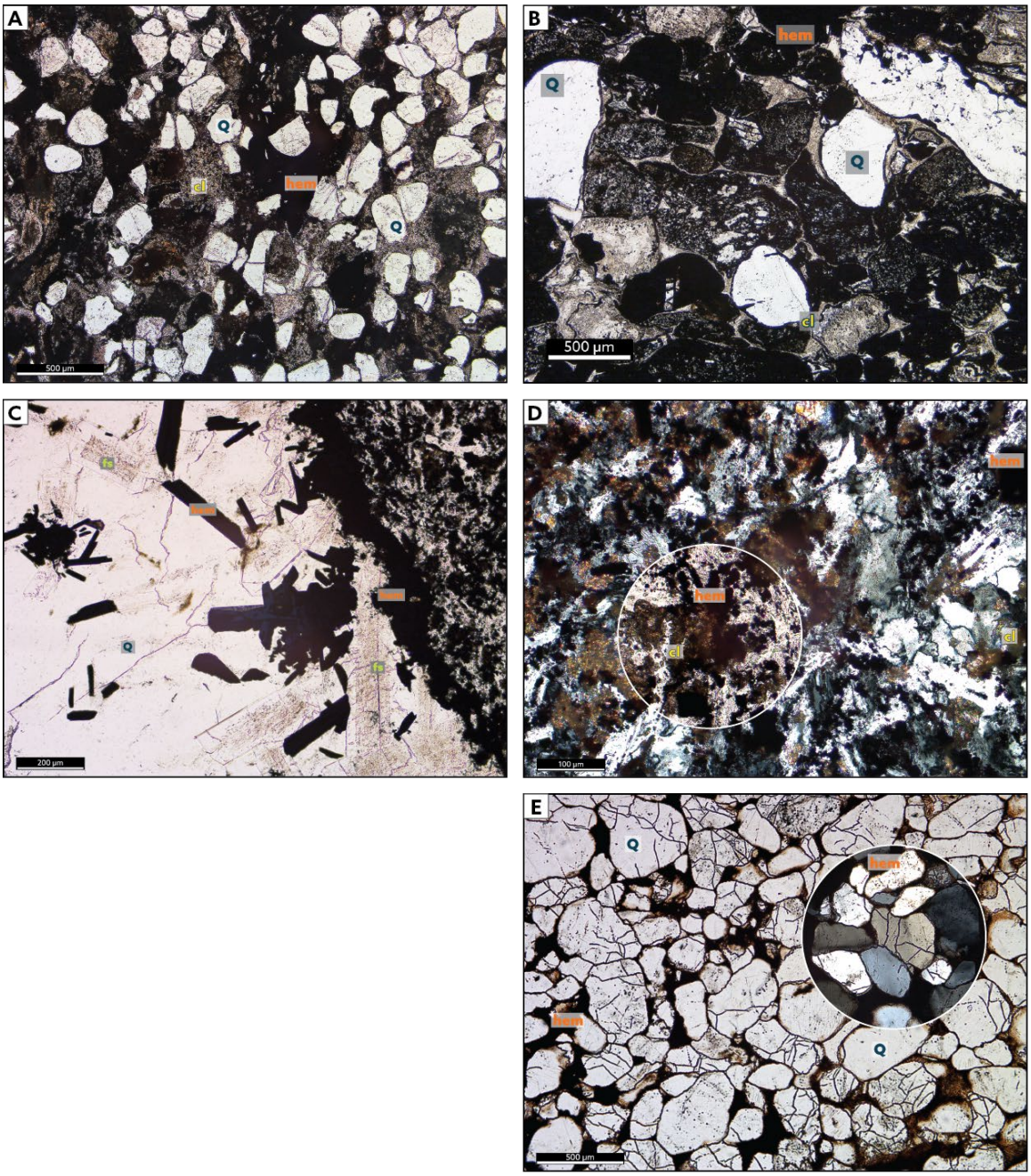
A
Q
cl
hem
Q
500 µm
B
hem
Q
Q
cl
500 µm
C
fs
hem
hem
Q
fs
200 µm
D
hem
hem
cl
cl
100 µm
E
Q
hem
hem
Q
500 µm

Monazite

Textures

Monazite occurrence is divided into three main groups based on texture and context: individual grains (Group 1), patchy cements (Group 2), and mineral inclusions in other phases (Group 3; Fig. 8a-d). Group 1, or individual monazite grains, are subhedral to euhedral and found in two of the four samples that contain monazite, AP17_66MF_4 (grains m1, m2, m3a, m3b, m5, and m6) and AP17_66MF_5 (grains m1, m2, m6, m7). They are generally associated with clays and are in two primary contexts: as a crust around pitted quartz grains and as a pore filling cement (Fig. 8a, 8b). Crusts comprise sub-micron to micron, subhedral to euhedral monazite laths with a similar texture as adjacent calcium and potassium-rich fibrous clays (Figs. 7b; 8a; sample AP17_66MF_5 grains m2, m6, and m7). These monazites are concentrated within the thin, 1 – 1.5 cm-thick layer of apatite- and hematite-cemented, fine-grained siltstone that marks the contact between the Browns Hole Formation and underlying Mutual Formation. Individual monazite grains in the pore spaces between other phases, occur as subhedral laths but are much larger, up to 10 μm thick and 20 μm long, and are associated with hematite cements and patches of fine-grained clays (Fig. 8b; sample AP17_66MF_4 grains m1, m2, m3a, m3b, m5, and m6 and sample AP17_66MF_5 grain m1).

Group 2 patchy cement monazite appear in the pore spaces between and within other phases in samples AP17_66MF_7 (grain m1) and AP17_66MF_11 (grains m1, m2, m4, m5; Fig. 8c, 8d). They are anhedral and blotchy with respect to contrast in BSE imagery. Brighter patches in BSE indicate areas with more elements that have higher atomic numbers, whereas darker patches have more elements with lower atomic numbers.

Patchy monazite cement is commonly associated with hematite and is observed in the pore spaces within individual hematite grains or clusters (Fig. 8d).

Group 3 monazites are found as rounded inclusions in other phases like quartz. Most monazite inclusions are entirely encased in quartz and have a homogeneous texture (Fig. 8f). However, two observed monazite inclusions in sample AP17_66MF_11 (grains m2 and m4) are located near the edges of their enclosing grains. These grains contain bright, tabular zones in BSE confirmed to be more Th-rich (Fig. 8e).

Because grains in Group 3 are fully encased in detrital quartz and are homogeneous with respect to texture and elemental composition, we suggest that they are also detrital grains. Monazite inclusions with patches of brighter material in BSE that reside along the edges of quartz are inferred to be detrital grains influenced by fluids that remove or alter material. Likewise, individual grains of Group 1 and cements of Group 2, that are not inclusions in other phases are likely authigenic.

Figure 8. BSE images of monazite grains. Inset images, where applicable, are zoomed to show grain detail. (A) Sample AP17_66MF_5 grain m2, individual monazite grain clusters lining pitted quartz grains and mimic adjacent fibrous clay minerals (Fig. 4b). Note that the central cluster of grains appears to be precipitating in a grain fracture. (B) Sample AP17_66MF_4 grain m1, individual monazite grains precipitating along grain boundaries. Notice the contrast in size and overall amount of clustered grains compared to the example in A. (C) Sample AP17_66MF_7 grain m1, patchy monazite cement. Regard in the inset image the porosity of the grain; due to this fact, very little or poor chemical data was acquired from grains of this category. (D) Sample AP17_66MF_11 grain m1, example of a porous hematite grain with infilling patchy monazite cement. Observe that monazite precipitation is concentrated to the pores closest to the grain boundary. (E) Sample AP17_66MF_11 grain m2, grain with Th-rich domains, brighter spots in the inset image. Notice that this grain is almost entirely encased in quartz. (F) Sample AP17_66MF_7 grain 4, detrital monazite grain entirely encased in quartz.

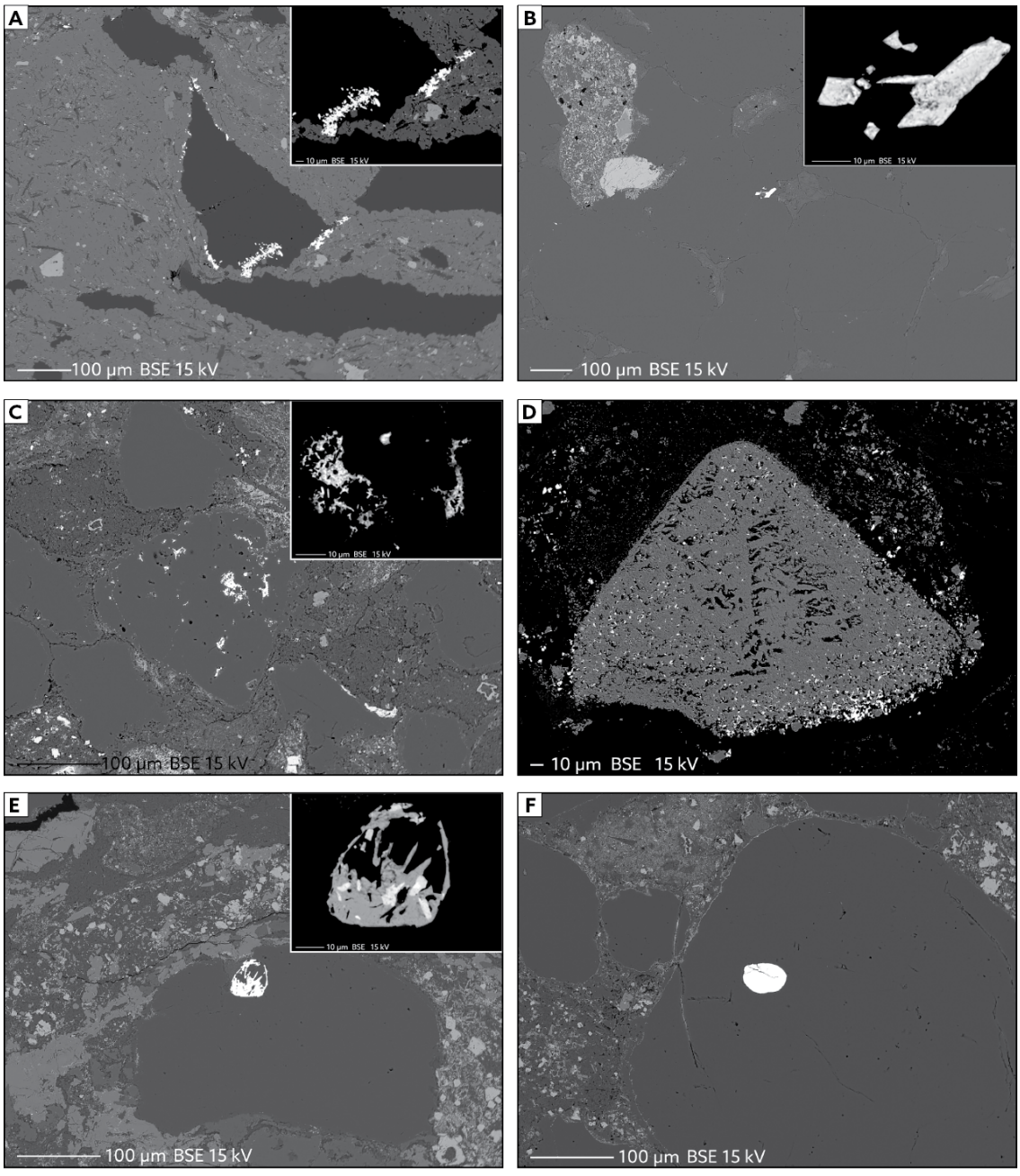
A
100 µm BSE 15 kV
B
100 µm BSE 15 kV
C
100 µm BSE 15 kV
D
10 µm BSE 15 kV
E
100 µm BSE 15 kV
F
100 µm BSE 15 kV

Monazite Geochemistry

Compositional data for Group 1 and Group 2 authigenic monazites are normalized to detrital grains (Group 3) found within these samples, chondrite, North American shale composite (NASC), and Moacyr, the typical monazite standard used during analyses (Gonçalves et al., 2016; Table 1; Fig. 9). Most authigenic grains have almost no U and <1 wt% Th and are depleted in heavy REE (HREE) and enriched in light REE (LREE) relative to detrital grains. However, several exceptions exist. First, there is a distinct enrichment in Eu in authigenic grains relative to detrital grains, and patchy cements are less enriched or even depleted. Second, there is a significant dispersion in Yb in authigenic grains relative to detrital grains that does not appear to be related to texture or sample. Approximately one-third of analyzed grains have Yb below the instrument detection limit and approximately half of the remaining analyzed grains are somewhat enriched in Yb. Third, almost all grains from sample AP17_66MF_11 are depleted in all REE, except Ce and La. In the case of La, two of the grains from this sample are noticeably more enriched than other grains (Fig. 9a).

Average concentrations of Group 1 and Group 2 monazites normalized to chondrite and NASC illustrate similar, if not identical, patterns. Grains are significantly enriched in La, Ce, and Nd and less so in the HREE: Tb, Er, Yb, and Y (Fig. 9b, 9c). Group 1 monazites are generally more enriched in all REE than Group 2 grains. Grains in Group 2 have more REE concentrations at or near the detection limit.

Group 1 and Group 2 authigenic monazites normalized to Moacyr display similar patterns to those expressed relative to Group 3 detrital grains. Authigenic monazites are generally enriched in LREE and depleted in HREE (Fig. 9d). Group 1 grains show a

significant enrichment of Eu, unlike most grains in Group 2, which are largely depleted in Eu. However, two grains in Group 2, m1 (sample AP17_66MF_7) and m5 (sample AP17_66MF_11) are significantly enriched in Eu. Additionally, most grains show a substantial dispersion in Yb concentrations unrelated to grain morphology. Group 1 grains are slightly more enriched in Gd with respect to Moacyr than grains normalized to Group 3 detrital grains.

An attempt was made to chemically date authigenic monazite using the U-Th-Pb system to determine a formation age and timing of fluid-flow (Allaz et al., 2013). However, there was insufficient actinide and Pb daughter content to determine any age in most authigenic grains. Detrital monazite inclusions in quartz were dated as being ~1-2 Ga (Table 1).

Table 1. Average geochemical compositions of authigenic and detrital monazites as well as Moacyr and other datasets used to normalize REE geochemical data. Values are in weight percent.

	Authigenic															Detrital				Standard	REE Normalization		
Sample	66mf_4						66mf_5				66mf_7	66mf_11				66mf_7							NASC
Grain	m1	m2	m3a	m3b	m5	m6	m1	m2	m6	m7	m1	m1	m2	m4	m6	n=4 m3	n=2 m4	m5a rim	m5b core	Moacyr*	Chondrite[a]	[b]	[c]
																date 1.817 ±8.63	1.067 ±0.75						
O	25.77	25.76	27.43	26.69	26.78	26.79	26.90	27.54	26.89	25.24	27.00	26.02	26.55	26.38	23.95	27.00	27.34	25.78	26.71	26.54			
Si	0.13	0.11	0.40	0.12	0.21	0.04	0.02	0.05	0.01	0.20	0.82	0.78	0.15	0.35	0.70	0.09	0.26	1.08	0.33	0.54			
S	0.32	0.56	0.54	0.56	0.53	0.43	0.73	0.53	0.32	0.36	0.34	0.14	0.05	0.05	0.10	bdl	bdl	0.09	0.02	0.02			
P	12.22	12.03	12.57	12.17	12.15	12.39	12.12	12.67	12.48	11.35	12.34	11.41	12.58	12.44	10.59	13.02	13.03	11.17	12.58	12.22			
K	0.01	0.13	0.04	0.02	0.03	0.07	0.08	0.01	bdl	0.04	0.02	0.05	0.02	0.06	bdl	bdl	bdl	0.01	bdl	0.01			
Ca	0.70	0.96	1.10	1.01	0.97	0.84	1.34	1.24	1.01	0.98	0.87	0.25	0.18	0.17	0.82	0.75	0.94	0.26	0.72	0.32			
Pb	bdl	bdl	bdl	0.00	bdl	bdl	bdl	bdl	0.00	0.01	bdl	0.00	0.02	0.02	bdl	0.65	0.44	0.96	0.85	0.14			
Th	0.03	0.22	0.06	0.07	0.13	0.29	0.01	0.01	0.02	0.02	bdl	0.04	0.71	0.87	9.68	2.68	6.93	8.21	5.69	5.81			
U	bdl	bdl	0.01	0.01	0.01	0.02	0.00	0.01	0.02	0.02	bdl	bdl	0.01	0.01	bdl	1.37	0.61	0.19	0.29	0.11			
Fe	bdl	bdl	bdl	bdl	bdl	bdl	bdl	bdl	bdl	bdl	bdl	1.82	bdl	bdl	bdl	bdl	bdl	bdl	bdl	bdl			
La	9.05	7.71	7.64	9.98	9.05	10.14	13.54	10.04	10.24	10.35	12.50	12.96	19.40	19.13	11.28	11.50	10.29	12.19	12.05	12.53	3.67×10^{-5}	31.10	
Ce	24.91	23.34	24.58	27.13	26.09	26.62	28.88	28.13	27.62	26.56	27.02	28.62	31.32	30.79	24.30	23.93	22.18	23.67	23.84	24.85	9.57×10^{-5}	67.03	
Nd	13.13	13.85	15.54	12.86	14.53	13.21	9.56	13.58	14.00	12.94	10.42	9.56	4.84	4.45	7.87	11.37	9.47	9.24	9.00	9.48	7.11×10^{-5}	30.40	
Pr	3.29	3.25	3.65	3.45	3.62	3.42	2.74	3.33	3.33	3.07	3.13	2.71	1.96	1.87	2.36	2.89	2.61	2.57	2.54	2.77	1.37×10^{-5}		7.90
Sm	1.92	2.20	2.67	1.75	2.31	2.01	0.91	1.70	1.92	1.66	0.87	0.66	0.13	0.09	0.79	2.01	1.76	1.53	1.69	1.59	2.31×10^{-5}	5.98	
Eu	0.45	0.51	0.56	0.46	0.48	0.54	0.18	0.36	0.38	0.36	0.09	0.06	0.01	0.01	0.03	0.04	bdl	0.01	0.05	0.01	8.70×10^{-6}	1.25	
Tb	0.03	0.02	0.03	0.04	0.03	0.05	0.02	0.03	0.02	0.03	bdl	bdl	0.01	0.00	0.03	0.13	0.16	0.07	0.11	0.06	5.80×10^{-6}	0.85	
Dy	0.08	0.07	0.08	0.09	0.07	0.11	0.01	0.05	0.04	0.05	0.03	bdl	0.01	bdl	0.05	0.31	0.67	0.19	0.38	0.21	3.81×10^{-5}	5.54	
Gd	0.73	0.88	0.93	0.70	0.77	0.91	0.31	0.62	0.68	0.61	0.24	0.11	0.10	0.03	0.15	1.47	1.39	0.92	1.19	0.75	3.06×10^{-5}	5.50	
Er	bdl	bdl	0.01	0.01	0.01	0.01	bdl	0.01	0.00	0.00	bdl	bdl	bdl	bdl	bdl	0.02	0.16	0.01	0.06	0.03	2.49×10^{-5}	3.28	
Yb	bdl	bdl	0.02	0.02	0.01	0.00	0.01	0.01	bdl	0.01	bdl	bdl	0.01	0.00	0.02	0.00	0.04	bdl	bdl	0.01	2.48×10^{-5}	0.85	
Y	0.12	0.24	0.20	0.07	0.08	0.16	0.01	0.08	0.07	0.05	0.18	0.03	0.04	0.05	0.05	0.43	2.00	0.39	0.89	1.00	2.10×10^{-4}		27.00
TOTAL	92.70	91.73	98.05	97.12	97.77	98.05	97.37	99.95	98.96	93.73	95.69	94.99	97.90	96.59	91.02	99.62	100.23	98.52	98.97	99.01			

Notes: bdl = below detection limit. (a) Taylor and McLennan (1985). (b) Gromet et al. (1984). (c) Haskin and Haskin (1996).

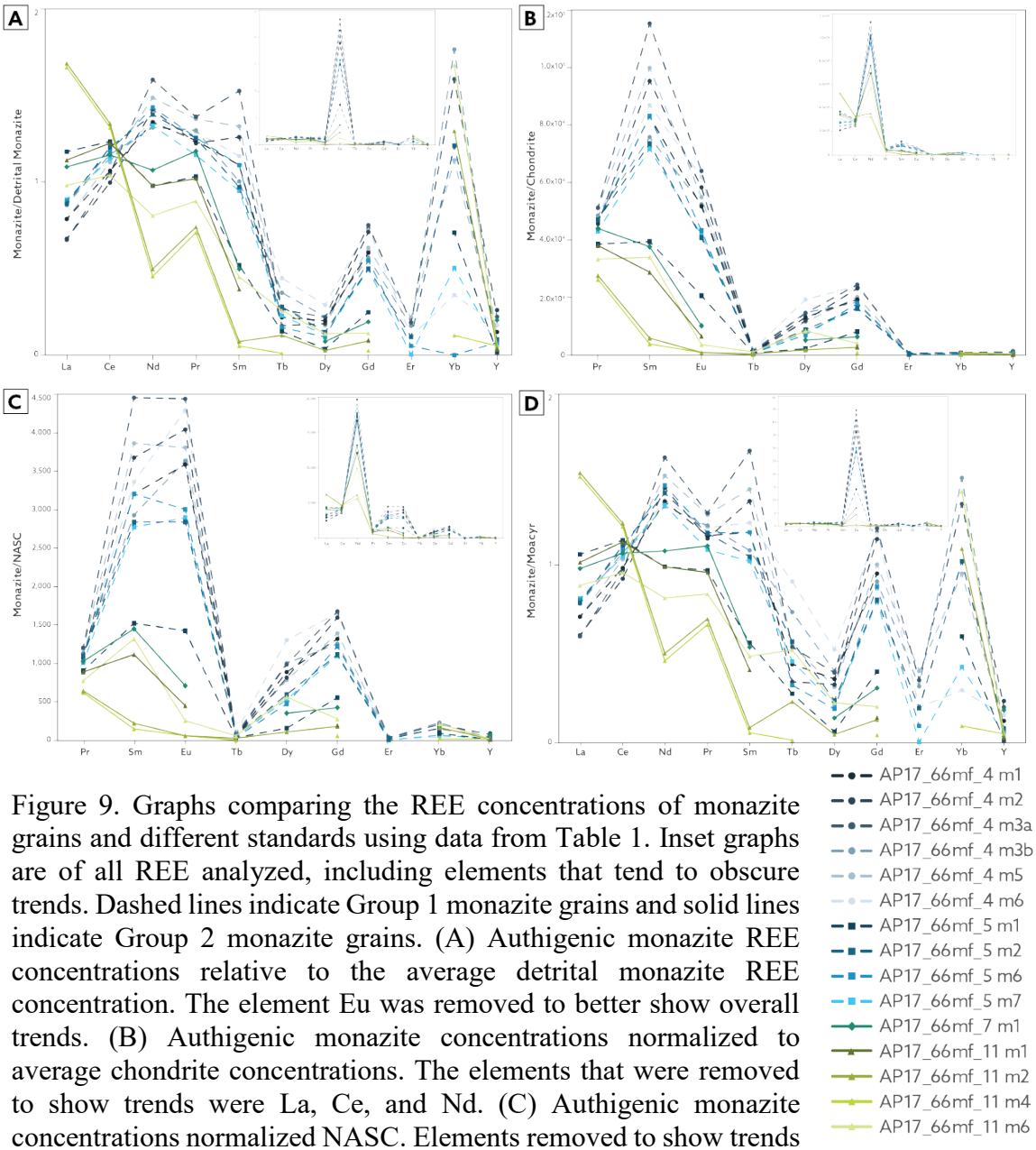

Figure 9. Graphs comparing the REE concentrations of monazite grains and different standards using data from Table 1. Inset graphs are of all REE analyzed, including elements that tend to obscure trends. Dashed lines indicate Group 1 monazite grains and solid lines indicate Group 2 monazite grains. (A) Authigenic monazite REE concentrations relative to the average detrital monazite REE concentration. The element Eu was removed to better show overall trends. (B) Authigenic monazite concentrations normalized to average chondrite concentrations. The elements that were removed to show trends were La, Ce, and Nd. (C) Authigenic monazite concentrations normalized NASC. Elements removed to show trends are La, Ce, and Nd. Note the similarities between the overall patterns relative to chondrite and NASC. (D) Authigenic monazite concentrations normalized to Moacyr. Only the element Eu was removed to show trends.

Detrital Apatite Geochronology

Morphology and textures

Apatite grains analyzed for LA-ICP-MS U-Pb geochronology and cathodoluminescence (CL) imaging were extracted from sample AP17_66MF_13. This sample is a medium- to coarse-grained volcaniclastic sandstone taken from ~10 m above the contact between the Mutual Formation and the volcanic member of the Browns Hole Formation. This sandstone contains volcanic clasts ranging in size from course sand to pebble. SEM analysis of the sample revealed that apatite grains are found only in the matrix and none are observed in volcanic lithics. Apatite crystals have euhedral to subhedral morphology, with minor transport-induced rounding. Larger grains, ≤100 μm-long, are heavily fractured with grain pieces near each other, implying that grains were broken in-situ during compaction. Smaller grains, <50 μm-long, are fully intact and unfractured (Fig. 10a). BSE imagery and EDS reveal that grains generally do not have rims or overgrowths. However, one grain does show a faint, irregular rim in BSE that is not visible in EDS (Fig. 10b). Most in-situ grains have a pitted texture along grain boundaries that extends ~5 μm into the grain (Fig. 10c, 10d). Based on these morphologies and textures, we suggest that apatite crystals are proximally-sourced detrital grains.

CL images of mounted apatite obtained after U-Pb analysis support SEM observations from in-situ grains (Fig. 10a). Smaller apatites are euhedral with tips intact or slightly rounded and larger grains generally have at least one tip missing. Missing and rounded tips are likely a result of mineral separation techniques as SEM analysis of in-situ grains reveals euhedral crystals. CL images show concentric zoning with respect to

trace element concentration (Dempster et al., 2003), which is common in magmatic grains (Fig. 10b; Rakovan and Reeder, 1994). Grains do not show any evidence of overgrowths in CL. Several grains have micron scale mineral inclusions in both the petrographic and CL analysis of mineral separates (Fig. 11).

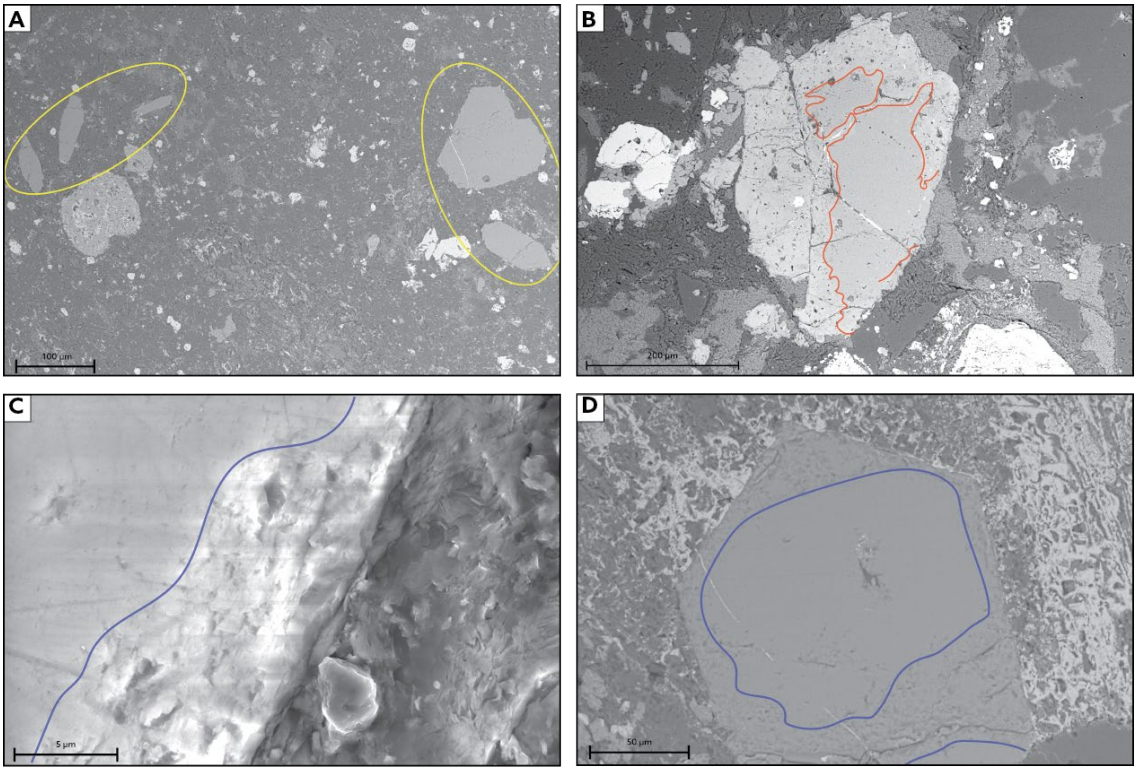

Figure 10. SEM images of in-situ apatite grains. (A) Example of intact, in-situ apatite grains, yellow circles indicate locations of grains. Note that all apatite grains shown in this image are intact except for some cracking and are euhedral to subhedral with only minimal rounding of tips. (B) Apatite grain with a faint irregular rim, outlined in orange, that is characterized by a heavily pitted texture. Observe the infilling of some cracks by more dense minerals, lighter greys to white, and pits with less dense minerals, darker greys. (C) Pitted texture that is common in most analyzed in-situ grains. This texture is different from the pitted texture in (B) in that it is not coupled with a change in material density. (D) An example of a pitted texture like the example in (C) that extends further into the grain and mimics fracture boundaries. Notice the pristine nature of the grain tip, despite the pitted texture that follows grain and fracture boundaries there is no rounding. As with the texture in (B), the nature of the contact between the pitted rim and interior of the grain is irregular. However, unlike (B) there is little to no infilling of fractures or pits and, again, there is no material density change coincident with pitting.

Figure 11. Apatite mineral separates. (A) Single polar image of representative sample of apatite separates. Notice the grain in the center with the large, dark mineral inclusion or core—similar features were found on apatite grains during in-situ SEM analysis. Also note the range of morphologies present from grain shards to the more common pill-like shape. (B) CL images of grains used for U-Pb dating. Regard the concentric zoning and inclusions (white or black spots or zones). Grains with an orange "x" were not analyzed because they were too small. (C) Zoom of grain 75 as an example of concentric zoning and euhedral grain morphology. (D) Zoom of grain 97. Note the irregular zoning, a possible reason this grain yielded an unreasonable date and error.

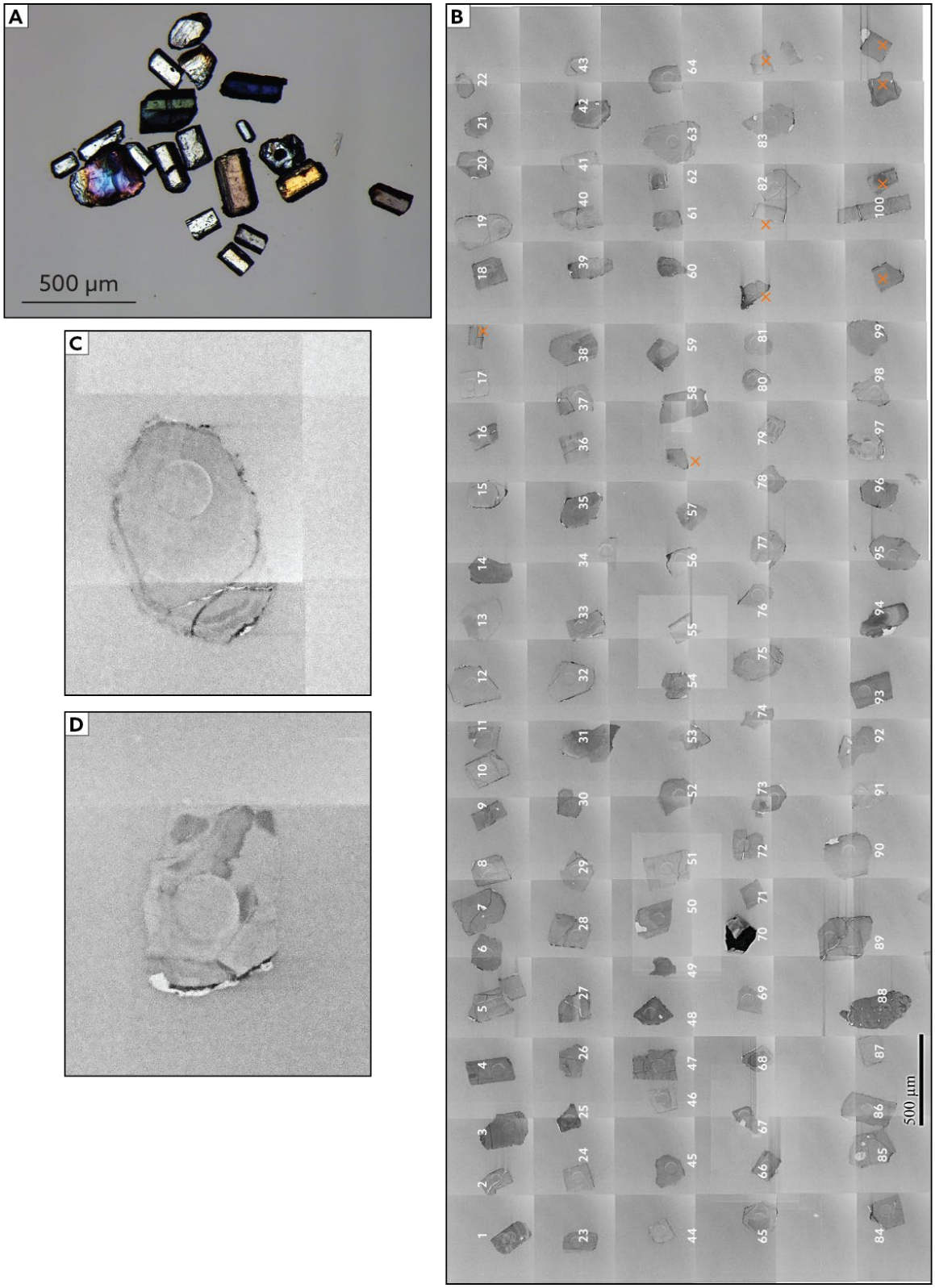
A
500 µm
B
500 µm
C
D

U-Pb Data

Detrital apatite grains from this sample yield low U concentrations (~1 ppm). Of 100 spots, 95 yield reasonable calculated dates and errors. These individual analyses range from 458 ± 63 Ma to 1140 ± 102 Ma, with a weighted mean of 612 ± 10 Ma (2σ; Fig. 12a, 12b; Table 2). Grains and corresponding error ellipses, excluding plotted on a Tera-Wasserberg concordia diagram are tightly clustered along a discordia line. The discordia line is anchored at the upper intercept of the agreed upon common Pb correction for 610 Ma (Stacey and Kramers, 1975) and regressed through the datapoints to the lower intercept of the discordia line, which represents the "true" age of the dataset of 612 ±10 Ma. At least nine grains plot to the right of the tie line, suggesting they experienced Pb-loss and are younger than expected (Fig. 12c).

Because of the low U concentration, grains have high individual uncertainties. As such, we assess the individual precision of each datapoint in the program RadialPlotter (Vermeesch, 2009). Precision is determined by dividing the 1σ error of each grain by their calculated date. RadialPlotter also colorizes each point based on measured $^{206}Pb/^{204}Pb$. Inputting the 95 datapoints reveals a maximum of four age peaks of 524 ± 25 Ma, 620.9 ± 6.2 Ma, 770 ± 37 Ma, and 1137 ± 102 Ma (errors are reported as 1σ). The youngest peak is largely defined by two grains with relatively high precision and high amounts of radiogenic Pb. One of these grains (grain 67) has downhole laser ablation data that is progressively older towards the rim of the grain. Although progressively older dates are potentially an artifact of downhole fractionation, this grain is also one of the nine that likely experienced Pb-loss and is removed from the dataset. Eliminating that grain deconvolves the data into three peaks: 616.7 ± 5.3 Ma, 767± 38 Ma, and 1137 ±

102 Ma. The new youngest peak now corresponds to approximately 94% of the data within 2σ. The second young grain was not removed from the dataset because it has a higher uncertainty that overlaps with the new youngest peak of 616.7 ± 5.3 Ma within 2σ. Using the minimum peak algorithm in RadialPlotter (Vermeesch, 2009), based on the Galbraith algorithm (Galbraith, 2005), to assess the youngest age that a dataset can realistically have, provides a minimum age of 613 ± 5.9 Ma (1σ; Fig. 12d, 12e).

Table 2. LA-ICP-MS U-Pb isotopic data for all analyzed apatite grains.

	Composition		Isotopic Ratios					Dates (Ma)			Composition		Isotopic Ratios					Dates (Ma)	
Grain	U ppm	Pbc (%)	$^{206}Pb/^{204}Pb$	$^{207}Pb/^{206}Pb^{(a)}$	±2σ (%)	$^{206}Pb/^{238}U$	±2σ (%)	$^{206}Pb/^{238}U$	±2σ (abs.)	Grain	U ppm	Pbc (%)	$^{206}Pb/^{204}Pb$	$^{207}Pb/^{206}Pb^{(a)}$	±2σ (%)	$^{206}Pb/^{238}U$	±2σ (%)	$^{206}Pb/^{238}U$	±2σ (abs.)
1	0.6	34.09	54	0.3587	12.54	0.1095	7.93	669.68	50.47	51	0.5	53.00	36	0.5541	7.15	0.1105	10.94	675.48	70.16
2	0.7	48.23	44	0.4814	10.01	0.0889	11.69	548.75	61.49	52	0.7	36.99	49	0.3798	3.46	0.0976	6.88	600.07	39.44
3	1.0	65.72	24	0.7924	0.44	0.1935	9.79	1140.05	102.35	53	0.8	37.68	50	0.3846	11.64	0.0947	8.46	583.30	47.18
4	0.8	36.70	60	0.3769	8.74	0.0973	6.41	598.71	36.63	54	0.8	43.48	43	0.4490	6.48	0.1099	10.52	672.15	67.17
5	0.7	40.48	45	0.4171	7.54	0.1059	7.51	649.01	46.34	55	0.6	56.96	31	0.6248	6.20	0.1165	15.16	710.59	102.00
6	0.7	46.94	43	0.4694	6.94	0.0898	9.71	554.53	51.62	56	0.5	37.89	42	0.4130	13.01	0.1421	18.13	856.42	145.45
7	0.8	45.62	45	0.4652	5.19	0.1023	7.41	627.89	44.32	57	1.1	40.08	40	0.4190	11.91	0.1158	12.14	706.28	81.22
8	0.4	50.55	38	0.5086	12.49	0.0931	16.15	573.95	88.68	58	0.7	45.55	49	0.4522	5.81	0.0843	8.37	521.78	41.95
9	1.0	47.44	39	0.4814	4.19	0.0993	6.85	610.41	39.91	59	0.7	51.76	40	0.5229	7.43	0.0946	14.86	582.75	82.80
10	0.5	40.12	43	0.4183	12.49	0.1140	12.11	695.77	79.89	60	1.0	46.24	32	0.5568	12.60	0.1845	26.35	1091.34	264.65
11	0.6	51.59	38	0.5028	9.65	0.0737	14.23	458.28	62.96	61	0.7	37.04	52	0.3834	7.46	0.1039	6.83	637.18	41.43
12	0.6	39.74	50	0.4045	10.93	0.0962	9.31	592.10	52.66	62	0.6	45.18	50	0.4460	13.59	0.0801	12.92	496.68	61.75
13	0.5	57.09	33	0.5892	6.63	0.0970	12.09	596.65	68.88	63	0.9	43.00	48	0.4360	8.41	0.0972	8.81	597.77	50.32
14	0.7	39.41	50	0.4039	7.67	0.1007	6.50	618.68	38.33	64	0.7	39.40	50	0.4046	7.78	0.1022	8.19	627.10	48.96
15	0.7	58.77	25	0.7554	1.97	0.0914	8.04	564.09	43.43	65	0.5	44.27	44	0.4556	6.75	0.1080	10.95	660.92	68.76
16	0.4	32.60	61	0.3455	24.97	0.1107	14.72	676.93	94.60	66	0.7	48.57	45	0.4856	6.14	0.0899	8.16	554.68	43.35
17	0.7	53.87	35	0.5561	5.09	0.1032	9.04	632.86	54.52	67	1.2	35.51	54	0.3581	6.01	0.0801	5.88	496.82	28.11
18	1.2	33.43	57	0.3532	9.96	0.1107	6.95	676.97	44.63	68	0.8	35.45	53	0.3705	4.48	0.1077	5.38	659.61	33.75
19	0.5	50.87	43	0.5069	8.38	0.0872	11.52	539.04	59.56	69	0.8	41.85	45	0.4268	6.65	0.1001	7.57	615.14	44.40
20	1.3	36.34	54	0.3733	5.59	0.0965	4.90	594.12	27.79	~~70~~	~~0.3~~	~~84.37~~	~~21~~	~~0.7382~~	~~43.60~~	~~0.0088~~	~~238.54~~	~~56.63~~	~~134.51~~
21	0.7	40.27	47	0.4128	6.17	0.1021	6.67	626.90	39.86	71	1.1	26.39	69	0.2893	6.66	0.1104	4.57	674.84	29.30
22	0.4	51.99	35	0.5413	6.49	0.1101	10.54	673.18	67.39	72	0.6	54.02	36	0.5435	8.24	0.0903	13.00	557.59	69.45
23	0.9	33.74	58	0.3579	8.57	0.1146	6.31	699.52	41.83	73	0.7	38.17	48	0.3889	10.62	0.0943	8.54	580.72	47.43
24	0.7	39.54	51	0.4074	4.75	0.1047	6.53	642.09	39.93	74	0.8	34.63	60	0.3605	8.22	0.1028	6.34	630.83	38.08
25	1.1	29.45	72	0.3101	7.76	0.0937	7.39	577.45	40.83	75	0.7	38.57	48	0.4038	10.22	0.1149	8.28	701.07	54.98
26	0.9	26.21	86	0.2856	13.45	0.1047	5.91	642.12	36.14	76	0.6	38.55	46	0.3976	10.45	0.1040	11.44	637.91	69.46
27	0.7	47.62	46	0.4773	9.21	0.0915	10.31	564.26	55.73	77	0.4	45.25	37	0.4741	8.68	0.1195	9.33	727.67	64.23
28	0.7	36.66	56	0.3768	11.65	0.0978	9.38	601.57	53.85	78	0.6	43.62	43	0.4433	4.22	0.0991	6.34	609.20	36.84
29	1.0	36.71	53	0.3796	6.86	0.1024	6.17	628.17	36.92	79	0.5	47.05	41	0.4760	12.54	0.0973	13.08	598.30	74.75
30	0.7	41.82	46	0.4221	6.74	0.0928	7.88	572.04	43.11	80	1.0	37.13	59	0.3791	7.45	0.0939	6.61	578.28	36.56
31	2.0	34.93	57	0.3609	4.18	0.0975	4.30	599.94	24.63	81	0.5	46.00	41	0.4679	5.44	0.1008	7.16	619.08	42.27
32	0.4	46.80	41	0.4651	8.08	0.0856	10.02	529.58	50.94	82	0.5	52.70	44	0.5281	8.27	0.0894	11.50	551.82	60.81
33	1.1	40.04	53	0.4016	6.16	0.0857	6.09	529.91	31.00	83	0.7	38.41	49	0.3977	8.32	0.1066	7.33	653.13	45.53
34	0.6	38.31	45	0.4007	8.56	0.1139	8.59	695.57	56.67	84	0.6	36.60	54	0.3807	18.97	0.1067	12.61	653.80	78.41
~~35~~	~~0.7~~	~~62.14~~	~~28~~	~~0.5955~~	~~10.01~~	~~0.0580~~	~~104.16~~	~~363.23~~	~~368.29~~	85	0.7	31.49	59	0.3344	10.77	0.1085	6.44	663.98	40.60
36	0.6	50.59	40	0.5054	6.52	0.0889	11.55	549.03	60.80	86	0.6	39.70	41	0.4277	14.03	0.1359	12.11	821.33	93.36
37	0.8	36.26	55	0.3745	8.17	0.1006	6.50	617.71	38.29	87	0.7	43.60	44	0.4423	6.70	0.0980	8.27	602.90	47.58
38	0.6	39.67	52	0.4052	9.03	0.0986	13.22	606.16	76.50	88	1.2	51.15	25	0.7532	1.28	0.1281	5.67	777.01	41.54
39	0.6	45.12	45	0.4561	11.31	0.0965	11.71	593.66	66.43	89	0.7	50.13	40	0.5100	3.95	0.0997	7.34	612.69	42.87
40	0.5	43.50	43	0.4445	9.22	0.1028	10.42	630.52	62.62	90	1.1	27.84	67	0.2988	10.08	0.1013	5.33	622.23	31.61
~~41~~	~~0.6~~	~~24.42~~	~~30~~	~~0.5188~~	~~15.15~~	~~0.4256~~	~~45.02~~	~~2285.95~~	~~871.66~~	91	0.5	49.29	37	0.5006	11.18	0.0992	15.36	609.79	89.35
42	0.8	32.03	62	0.3335	9.85	0.0948	6.96	583.70	38.82	~~92~~	~~0.8~~	~~43.54~~	~~28~~	~~0.4636~~	~~19.11~~	~~0.1297~~	~~247.85~~	~~785.89~~	~~1885.83~~
43	0.6	56.41	36	0.5646	3.38	0.0849	9.28	525.51	46.84	93	0.8	39.86	50	0.4072	8.12	0.0991	7.91	609.38	46.02
44	0.6	45.79	50	0.4528	8.01	0.0818	9.67	506.89	47.16	94	0.8	44.27	44	0.4465	7.63	0.0943	8.56	580.94	47.57
45	0.7	35.33	60	0.3708	11.30	0.1107	7.14	676.68	45.84	95	1.1	32.73	63	0.3404	8.26	0.0964	6.81	593.15	38.58
46	0.6	46.30	44	0.4666	10.90	0.0947	12.94	583.53	72.22	96	1.2	36.37	58	0.3643	7.24	0.0770	13.03	478.13	60.06
47	1.0	53.07	33	0.5820	5.30	0.1298	8.66	786.53	64.13	~~97~~	~~0.3~~	~~40.34~~	~~23~~	~~0.8270~~	~~1.21~~	~~1.2014~~	~~5.99~~	~~5086.89~~	~~210.84~~
48	1.1	29.38	67	0.3145	10.18	0.1065	5.78	652.61	35.86	98	0.8	37.49	51	0.3889	9.52	0.1064	8.16	652.02	50.61
49	1.1	33.63	54	0.3547	14.08	0.1100	14.98	672.71	95.72	99	1.3	38.90	51	0.3987	8.43	0.0999	7.71	613.85	45.15
50	0.6	43.42	44	0.4437	7.62	0.1028	8.11	630.92	48.76	100	0.8	33.37	52	0.3625	10.18	0.1314	8.99	796.09	67.33

[a]Uncorrected for common Pb; all other data has been corrected for common Pb using Stacey and Cramers (1975).
Crossed out datapoints are mean calculations.

Figure 12. Apatite U-Pb results. (A) Age distribution of apatite grains, green horizontal line indicates the mean age of 612 ± 10 Ma. (B) Histogram of apatite U-Pb ages. (C) Tera-Wasserburg diagram anchored through common Pb correction for 610 Ma of 0.878 (Stacey and Kramers, 1975). Blue ellipses are grains with potential Pb loss; shade of blue indicates the likelihood that grain experienced Pb-loss—darker blue is more likely and lighter blue is less likely. (D) RadialPlotter showing three age peaks. Color scale depicts relative amount of radiogenic Pb. Note that grains that plot near the oldest peak are yellow, indicating less radiogenic Pb, and grains that plot near the youngest peak are more orange and, therefore, have more radiogenic Pb. The x-axis is a measure of precision where σ is the individual error for a given point and t is the calculated age for a given point. More precise ages plot to the right, whereas less precise ages will plot to the left. (E) The same data as in (D) but redisplayed using the minimum peak algorithm. Errors on RadialPlotter diagrams are 1σ.

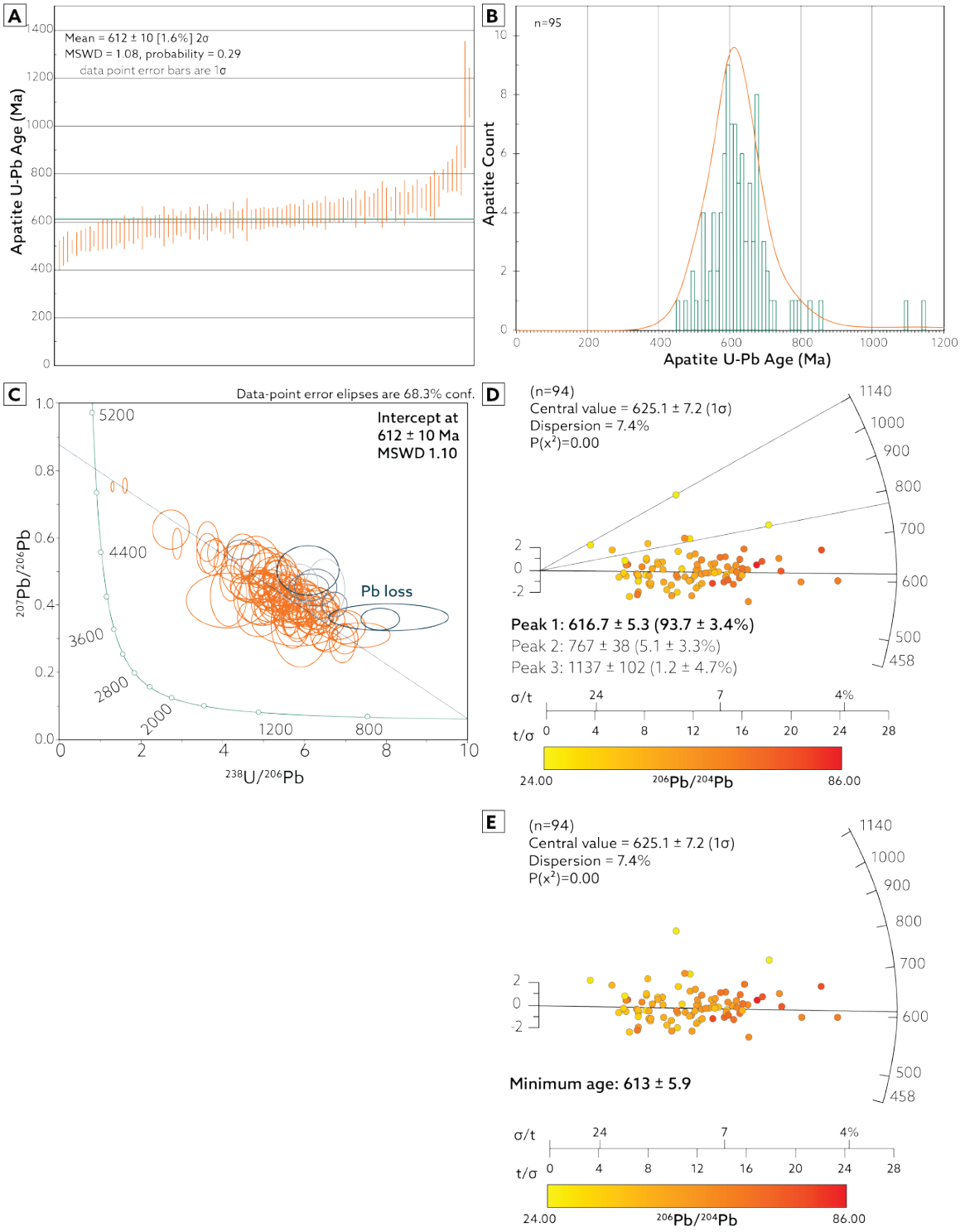
A
Mean = 612 ± 10 [1.6%] 2σ
MSWD = 1.08, probability = 0.29
data point error bars are 1σ
Apatite U-Pb Age (Ma)
B
n=95
Apatite Count
Apatite U-Pb Age (Ma)
C
Data-point error ellipses are 68.3% conf.
Intercept at
612 ± 10 Ma
MSWD 1.10
Pb loss
5200
4400
3600
2800
2000
1200
800
207Pb/206Pb
238U/206Pb
D
(n=94)
Central value = 625.1 ± 7.2 (1σ)
Dispersion = 7.4%
P(x²)=0.00
Peak 1: 616.7 ± 5.3 (93.7 ± 3.4%)
Peak 2: 767 ± 38 (5.1 ± 3.3%)
Peak 3: 1137 ± 102 (1.2 ± 4.7%)
σ/t
t/σ
24.00
206Pb/204Pb
86.00
E
(n=94)
Central value = 625.1 ± 7.2 (1σ)
Dispersion = 7.4%
P(x²)=0.00
Minimum age: 613 ± 5.9
σ/t
t/σ
24.00
206Pb/204Pb
86.00

DISCUSSION

Age of the Browns Hole Formation and Implications

We suggest a revised maximum depositional age of the volcanic member of the Browns Hole Formation of 613 ± 12 Ma (2σ), based on our detrital apatite U-Pb data. This is consistent with a previously reported U-Pb apatite date of 609 ± 25 Ma (2σ) from the overlying basalt by Verdel (2009), based the weighted mean of two multi-grain ID-TIMS analyses, n=5 and n=8, one of which was slightly discordant. The newly reported date of 613 ± 12 Ma is likely much closer to the actual depositional age than the previously reported age of 580 ± 14 Ma (2σ) (Crittenden Jr and Wallace, 1973; Christie-Blick and Levy, 1989) based on apatite morphology reflecting proximal sources. Apatite grains in sample AP17_66MF_8 are euhedral, not frosted (Figs. 10; 11), and are hosted nearly intact in the matrix of coarse-grained volcaniclastic rocks.

It is permissible that the true depositional age is <613 ± 12 Ma if these detrital apatites are sourced from a significantly older, yet proximal and easily weathered and transported deposit. However, we consider the 580 Ma date to be anomalously young based on potential problems associated with bulk $^{40}Ar/^{39}Ar$ dating. This is a total gas $^{40}Ar/^{39}Ar$ analysis on a hornblende phenocryst from a clast in the agglomerate several meters below the basalt flow (Crittenden Jr and Wallace, 1973; Christie-Blick and Levy, 1989). The $^{40}Ar/^{39}Ar$ dating method assumes a closed system and Ar-loss due to post-depositional reheating prior to analysis will result in anomalously young dates (Hodges, 2005). Modern stepwise heating methods record the incremental loss of Ar from different mineral domains to yield a reliable “plateau age” that is representative of formation (Reichow et al., 2002; Boyce et al., 2005). As this date was acquired via bulk heating

methods, it is not possible to assess the potential for Ar-loss. Furthermore, this $^{40}Ar/^{39}Ar$ date is outside the error of the previously reported apatite U-Pb date of 609 ± 25 Ma (Verdel, 2009), and the newly reported date in this study.

The new maximum depositional age of 613 Ma for the volcanic member of the Browns Hole Formation has implications for the timing and duration of deposition of regional stratigraphy. Our new date decreases the amount of time available for the deposition of ~1400 m of Browns Hole Formation and lower Brigham Group by ~33 Myr (Fig. 13). If the paleovalleys at the base of the Inkom Formation represent the end of Marinoan glaciation (Levy et al., 1994) and the Caddy Canyon Formation was deposited ca. 650 Ma (Yonkee et al., 2014), then ~1400 m of strata was deposited over ~37 Myr, from ca. 650 Ma to 613 Ma, or ~38 mm/kyr (Fig. 13a). However, if the pink dolostones overlying glacial diamictites of the Pocatello and Perry Canyon formations relate to Marinoan glaciation (Dehler et al., 2011, 2012) and the Caddy Canyon Formation was deposited at ca. 635 Ma, then ~1400 m of sediment was deposited in ~22 Myr from ca. 635 Ma to 613 Ma, or ~64 mm/kyr (Fig. 13b). Both rates are considered relatively slow (Sadler, 1981).

Revising the maximum depositional age of the Browns Hole Formation also affects the interpretation of paleovalleys at the base of the Inkom Formation. If the upper diamictites and pink dolostones of the Pocatello and Perry Canyon formations do represent the end of Marinoan glaciation (Dehler et al., 2011, 2012; Isakson, 2017; Isakson et al., in review) in western Laurentia (current orientation), then the paleovalleys at the base of the Inkom Formation are of unknown origin and more study is needed to determine their source. However, if the paleovalleys at the base of the Inkom Formation

correspond to sea level fluctuations following Marinoan glaciation, then no revision is needed (Fanning and Link, 2004; Balgord et al., 2013).

These revisions to Browns Hole Formation stratigraphy also impact interpretation of unconformities with overlying stratigraphy. For example, the unconformity that exists between the basalt flow cap of the volcanic member and overlying sandstone Terracotta member of the Browns Hole Formation may represent more missing time than previously thought. Likewise, the sequence boundary and documented unconformity that exists between the Terracotta member of the Browns Hole Formation and the overlying Geertsen Canyon Formation may represent even more missing stratigraphic time than previously thought (Fig. 13; Levy et al., 1994; Yonkee et al., 2014) .

Our geochronology data also has implications for the expression of Laurentian rifting in northern Utah. Prior geochronology and paleomagnetic data suggest that continental land masses attached to the western region of Laurentia began rifting >720 Ma and were completely separated sometime >600 Ma (Li et al., 2008; Yonkee et al., 2014). However, rift related volcanism continued until at least ~569 Ma (Colpron et al., 2002). The appearance of proximally sourced volcanic material refines this chronology and confirms that rift-related volcanism continued until at least 613 Ma. The volcanic member of the Browns Hole Formation likely represents one of the last episodes of rifting in the region before the transition to a passive margin. The presence of a basanitic "basalt" flow capping the volcanic member of the Browns Hole Formation (Verdel, 2009) is consistent with this interpretation. Basanite is a silica undersaturated lava common in continental rift and continental and oceanic mantle plume settings (Barberi et al., 1982).

Figure 13. Revised Wheeler diagrams with relevant representative regional stratigraphic sections. (A) Revised stratigraphy if the paleovalleys at the base of the Inkom Formation correspond to end Marinoan sea level fluctuations. (B) Revised stratigraphy if upper carbonates and diamictites in the Perry Canyon and Pocatello formations are related to Marinoan glaciation. (a) This research; (b) Verdel (2009). Figure is modified from Yonkee et al. (2014).

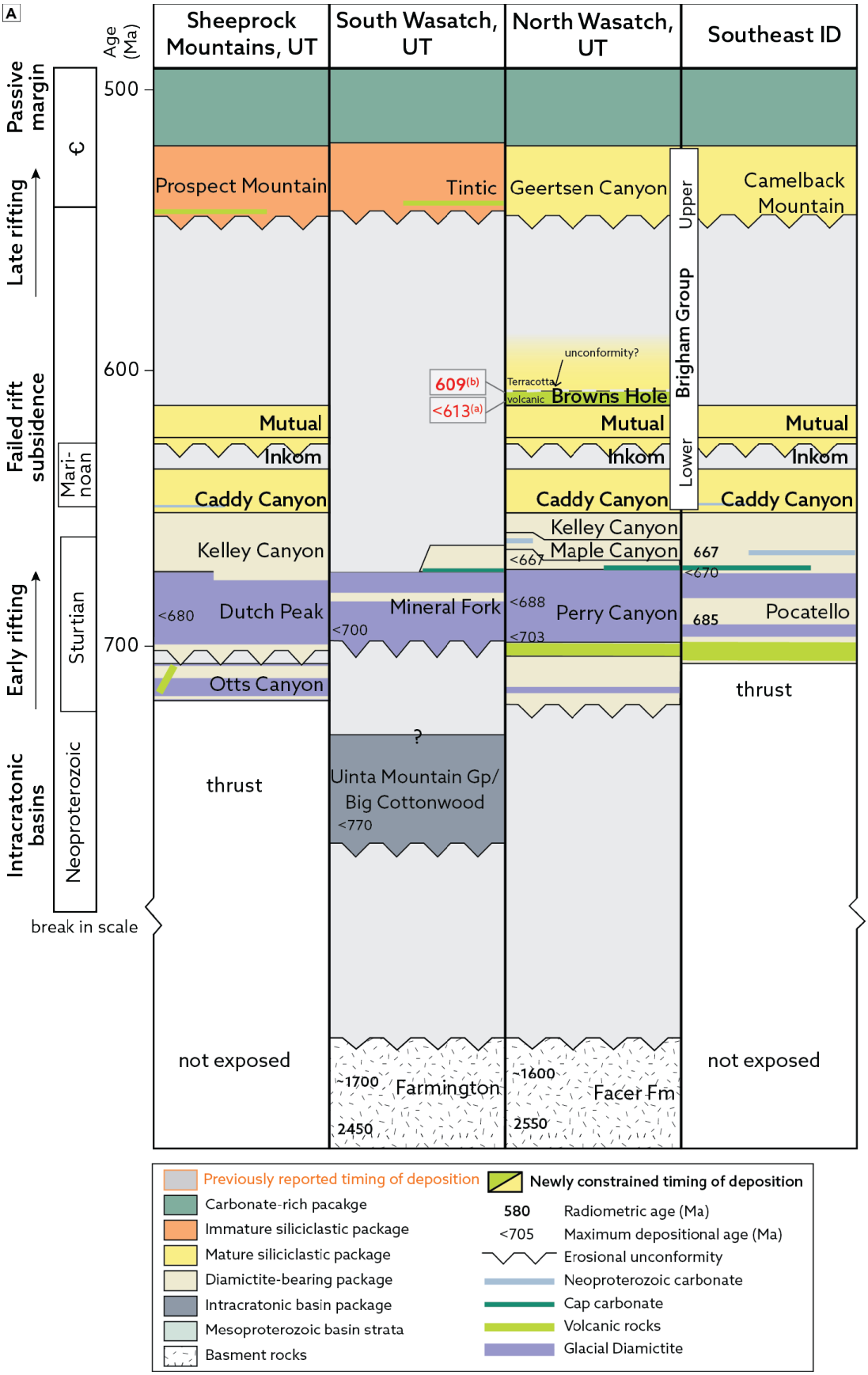
A
Age (Ma)
Sheeprock Mountains, UT
South Wasatch, UT
North Wasatch, UT
Southeast ID
Passive margin
Late rifting
Failed rift subsidence
Early rifting
Intracratonic basins
Cambrian
Mari-noan
Sturtian
Neoproterozoic
500
600
700
break in scale
Prospect Mountain
Tintic
Geertsen Canyon
Camelback Mountain
Brigham Group
Upper
Lower
unconformity?
Terracotta volcanic
Browns Hole
609(b)
<613(a)
Mutual
Inkom
Caddy Canyon
Kelley Canyon
Maple Canyon
<667
667
<670
<680
Dutch Peak
Mineral Fork
<700
<688
Perry Canyon
<703
685
Pocatello
Otts Canyon
thrust
?
Uinta Mountain Gp/
Big Cottonwood
<770
not exposed
~1700
Farmington
2450
~1600
Facer Fm
2550
Previously reported timing of deposition
Carbonate-rich pacakge
Immature siliciclastic package
Mature siliciclastic package
Diamictite-bearing package
Intracratonic basin package
Mesoproterozoic basin strata
Basment rocks
Newly constrained timing of deposition
580 Radiometric age (Ma)
<705 Maximum depositional age (Ma)
Erosional unconformity
Neoproterozoic carbonate
Cap carbonate
Volcanic rocks
Glacial Diamictite

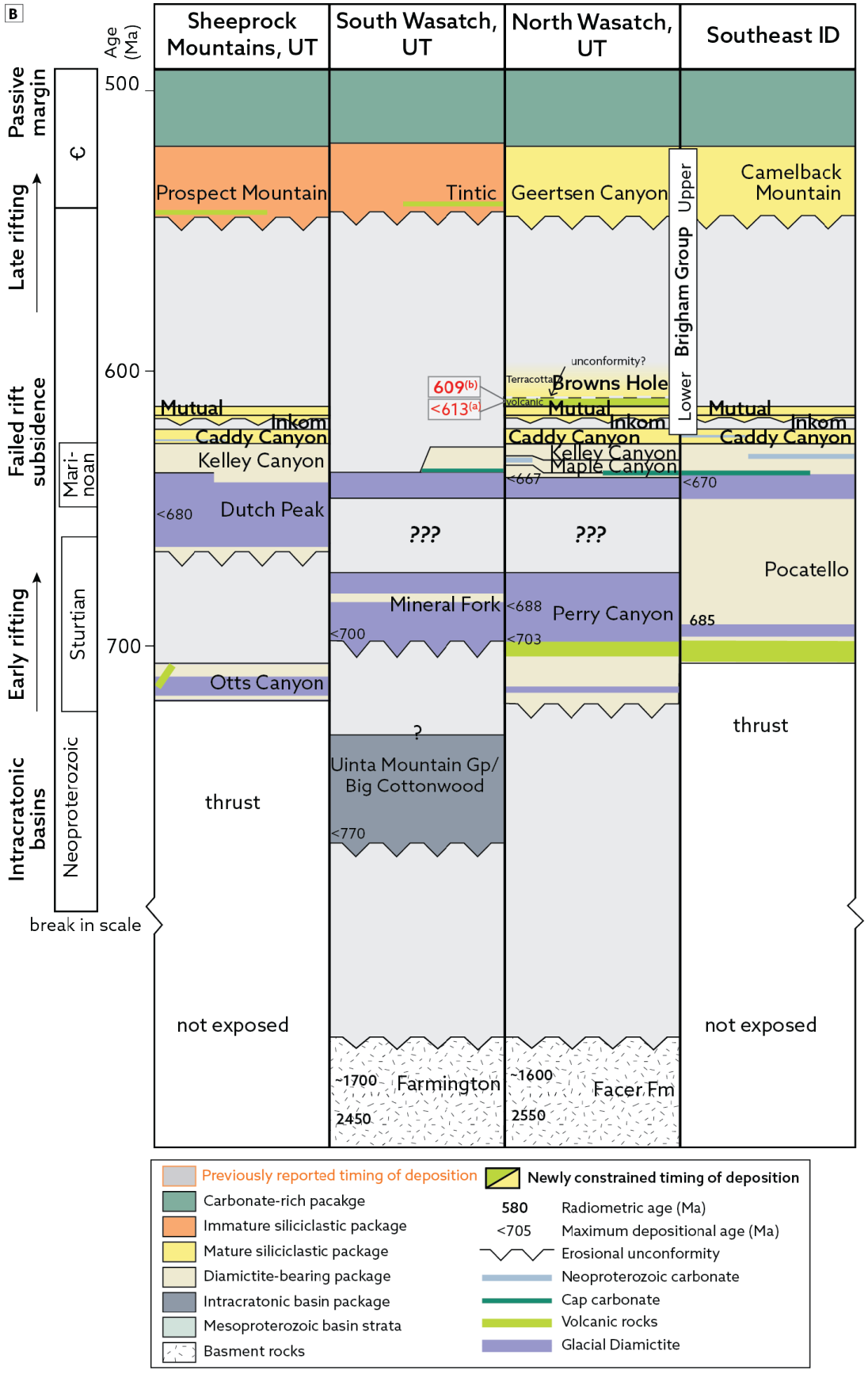
B
Age (Ma)
Sheeprock Mountains, UT
South Wasatch, UT
North Wasatch, UT
Southeast ID
Passive margin
Late rifting
Failed rift subsidence
Early rifting
Intracratonic basins
Cambrian
Mari-noan
Sturtian
Neoproterozoic
500
600
700
break in scale
Prospect Mountain
Tintic
Geertsen Canyon
Camelback Mountain
Upper
Lower
Brigham Group
unconformity?
Terracotta volcanic
Browns Hole
609(b)
<613(a)
Mutual
Inkom
Caddy Canyon
Kelley Canyon
Maple Canyon
<667
<670
<680
Dutch Peak
???
???
Pocatello
Mineral Fork
<688
Perry Canyon
685
<700
<703
Otts Canyon
?
Uinta Mountain Gp/
Big Cottonwood
<770
thrust
thrust
not exposed
not exposed
~1700
Farmington
2450
~1600
Facer Fm
2550
Previously reported timing of deposition
Carbonate-rich pacakge
Immature siliciclastic package
Mature siliciclastic package
Diamictite-bearing package
Intracratonic basin package
Mesoproterozoic basin strata
Basment rocks
Newly constrained timing of deposition
580 Radiometric age (Ma)
<705 Maximum depositional age (Ma)
Erosional unconformity
Neoproterozoic carbonate
Cap carbonate
Volcanic rocks
Glacial Diamictite

Post depositional fluid-rock interaction

Evidence for post-depositional fluid-rock interaction and diagenesis occurs on scales ranging from outcrop to microscopic. Using thin section petrography, SEM, SEM-EDS, and EMPA, we reconstruct a relative paragenetic sequence of post-depositional diagenesis for the observed section of Mutual and Browns Hole formations (Figs. 14-16). Additionally, we used the geochemical modeling program PHREEQC (Parkhurst and Appelo, 2005) to investigate the range of conditions, chiefly temperature, at which these diagenetic events may occur. PHREEQC uses the chemical properties of given mineral phases at specified temperatures to calculate the solubility index of each phase at equilibrium. Specifically, here the minerals albite, K-feldspar, quartz, hematite, and tremolite were reacted with water in PHREEQC to reach equilibrium in five steps over temperatures of 25 – 200 °C, and the resulting fluid chemistry and mineral solubility indices were calculated. The major post-depositional events observed include (1) early hematite grain-rimming cement, (2) development of quartz overgrowths and cements, (3) dissolution/alteration of feldspar grains, (4) dissolution of detrital monazite and potentially apatite, (5) partial dissolution of quartz grains, (6) precipitation of authigenic minerals including clays, monazite, and apatite cement, and (7) later stages of hematite cementation.

Evidence of fluid-rock interaction includes the ubiquitous hematite cement, which gives the volcanic member of the Browns Hole Formation and the uppermost Mutual Formation a distinct purple-red hue on both weathered and fresh surfaces. Hematite cement is less prevalent in the overlying Terracotta member of the Browns Hole Formation, and less pervasive in the rest of the Mutual Formation. This is consistent with

the composition of the primary sediments in the volcanic member of the Browns Hole Formation. Stratigraphically isolated pervasive hematite cement coupled with faint dust rims along relict grain boundaries in the remaining lower Mutual Formation suggests hematite precipitated in multiple phases: first, during early diagenesis (Walker, 1967, 1974), again during late burial, and finally during uplift diagenesis (Figs. 14b, 14f; 15f; 16).

Quartz overgrowths form over prior grain boundaries in the Terracotta member of the Browns Hole Formation and enclose faint dust rims formed during early diagenesis in the Mutual Formation. This process was likely protracted through burial diagenesis. Oxygen isotope studies show that quartz overgrowths can form under a variety of conditions, but at temperatures <60 °C require local additions of silica to pore fluids, for example from the dissolution of volcanic glass (McBride, 1989; Hiatt et al., 2007). In the Mutual Formation and Terracotta member of the Browns Hole Formation quartz is the only local source of silica, thus it is assumed that quartz overgrowth formation initiated during compaction at temperatures >60 °C (McBride, 1989; Hyodo et al., 2014). PHREEQC modeling suggests that quartz overgrowths would likely continue to form only until temperatures reach 150 °C, when quartz is more likely to dissolve.

Feldspar breakdown and hydrolysis to clays were likely protracted as many larger feldspar grains are only partially dissolved in these units. In the Mutual Formation, porous microcline and plagioclase feldspars are surrounded and infilled by fine-grained sericite and kaolinite clays. In the volcanic member of the Browns Hole Formation, smaller feldspars within volcanic clasts are completely replaced with fine grained clays (Figs. 14d; 15b, 15c; 16). Detrital feldspars are unstable even at low temperatures,

evident in the near ubiquitous authigenic clay cements in many feldspathic sandstones (Wilkinson and Haszeldine, 1996; Wilkinson et al., 2001). However, in the Mutual Formation and Geertsen Canyon Formation many feldspar grains remain partially intact, indicating that conditions did not favor full dissolution.

Authigenic phosphates (e.g., monazite and apatite) are limited to the volcanic member of the Browns Hole Formation and are more common in the reworked lithic tuff at the contact with the underlying Mutual Formation. Although detrital apatites are found in the upper units of the volcanic member, none are observed in the places where apatite cement is found. Likewise, no matrix monazite is observed anywhere in these units. Detrital monazites partially encased in quartz grains show evidence for fluid-mediated alteration. We hypothesize that detrital monazite, and potentially apatite, were dissolved and their constituents used in precipitation of authigenic grains and cements. Monazite and other REE-bearing minerals are more soluble at higher temperatures and increased fluid salinity (Allaz et al., 2013). Although monazite is soluble in both acidic and alkaline fluids at various temperatures (Ayers and Watson, 1991; Lewis et al., 1997; Oelkers and Poitrasson, 2002; Ayers et al., 2004; Poitrasson et al., 2004), apatite is only soluble in acidic fluids (Ayers and Watson, 1991). Therefore, it is likely that saline acidic fluids interacted with monazite and apatite grains to dissolve and re-precipitate as authigenic grains and cements (discussed below). Additionally, these fluids would have aided in the continued dissolution of feldspar grains, which would neutralize fluids.

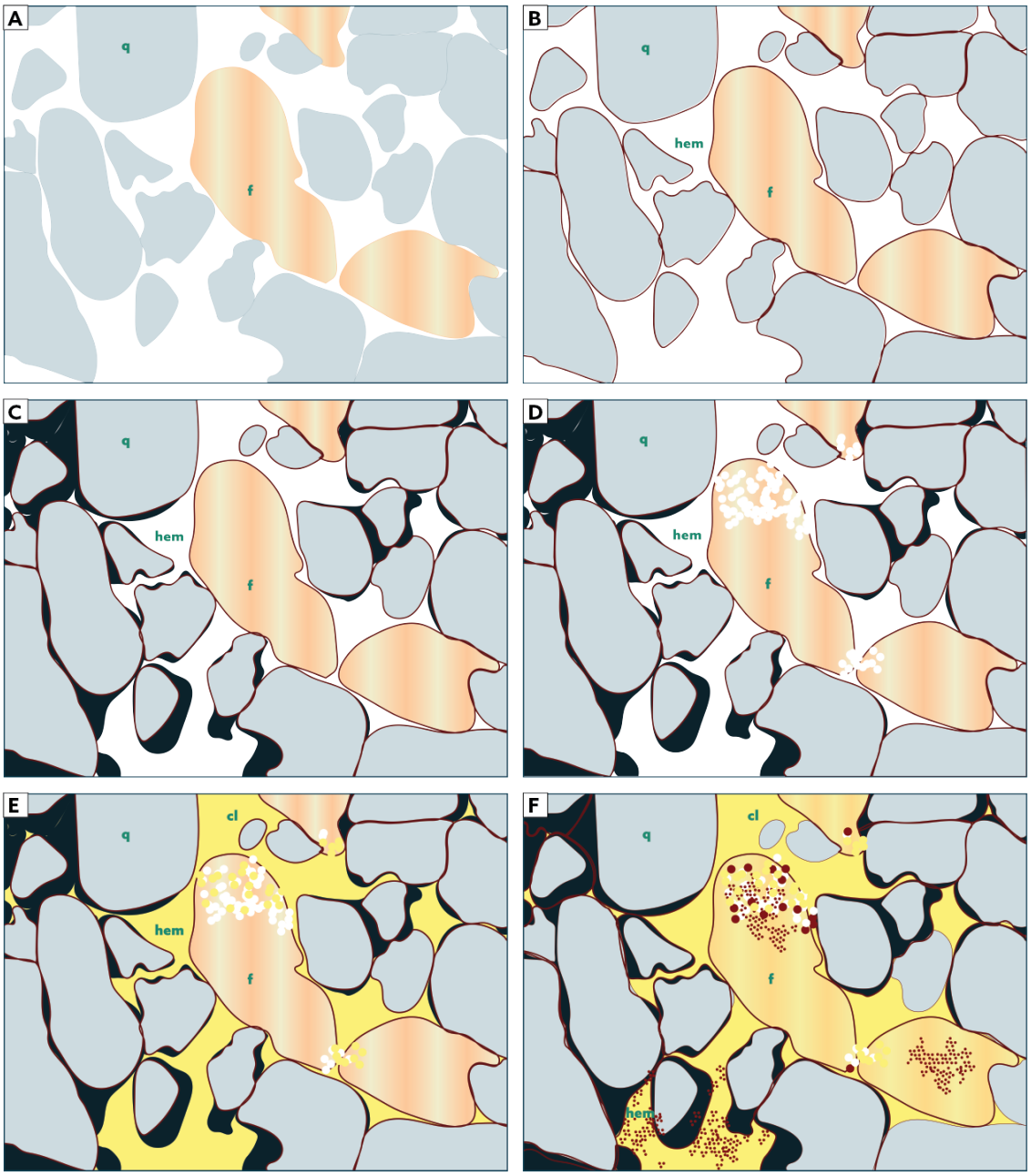

Figure 14. Generalized paragenetic sequence for the upper Mutual Formation. (A) Initial deposition. (B) First generation of hematite cement. (C) Formation of quartz overgrowths encasing initial hematite cements. (D) Initiation of feldspar breakdown. (E) Formation of fine-grained clay cements and partial replacement of feldspar grains. (F) Final phase of hematite cements and clay replacement. q=quartz; f=feldspar; hem=hematite cement; cl=clay

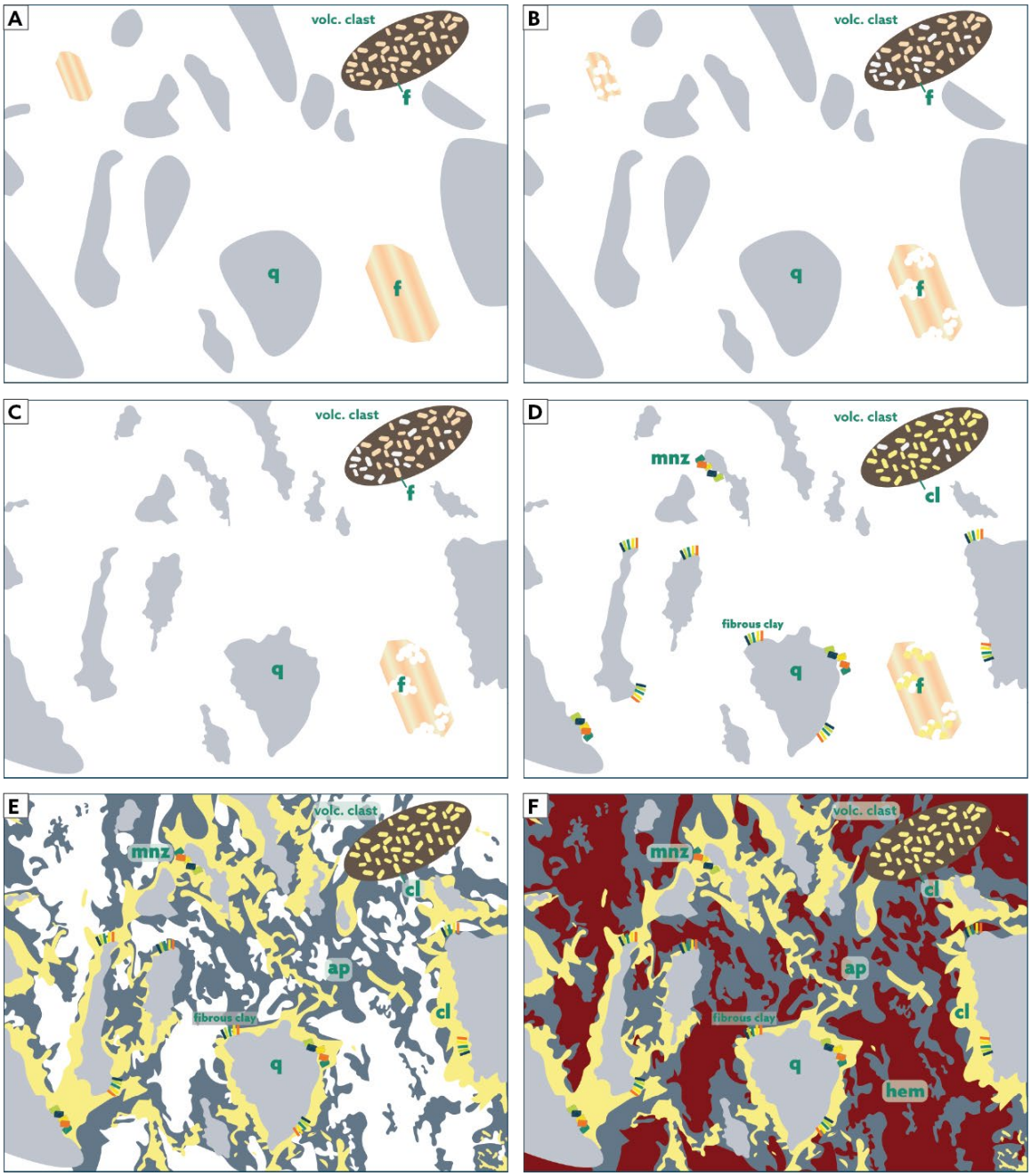

Figure 15. Generalized paragenetic sequence for the lower Browns Hole Formation. (A) Initial deposition. (B) Feldspars begin to breakdown. (C) Quartz grains are pitted, along with continued feldspar dissolution. (D) Monazite and coarse clays begin to precipitate. (E) Fine-grained clays and apatite cement are formed. (F) Final phase of hematite cement infiltrates remaining pore spaces. q=quartz; f=feldspar; cl=clay; mnz=authigenic monazite; hem=hematite cement; ap=microcrystalline apatite cement.

Phosphate dissolution may have occurred coeval with the partial dissolution of quartz grains yielding pitted textures along the edges of quartz grains at the contact between the Mutual and Browns Hole formations (Figs. 15c; 16). Because quartz will develop overgrowths at temperatures of 60 – 150 °C, pitting of quartz grains likely started at temperatures >150 °C with the addition of neutral to alkaline fluids (Figs. 15c; 16; Dove and Crerar, 1990). Quartz pitting is isolated to the contact between the Mutual and Browns Hole formations, indicating that the contact served as a conduit for increased fluid flow. Alternatively, this part of the section may have contained more reactive material, i.e. more feldspars, that allowed fluids to stay at neutral to alkaline pH.

The precipitation of fine-grained clay cements was protracted but occurred in at least two major pulses. The first pulse likely followed initial feldspar breakdown during burial diagenesis. A second episode of fine-clay followed the precipitation of other authigenic minerals, evident in clay cement found interstitially with apatite and hematite cements (Figs. 14e; 15e). Coarse clays, however, likely precipitated coincident with the final stages of other authigenic mineral precipitation including monazite, and apatite and hematite cements (Fig. 15d).

Monazite forms as a pore filling cement and as euhedral crystals alongside fibrous clay minerals in a matrix of authigenic microcrystalline apatite. Detrital monazite grains that are fully encased in quartz are featureless and unzoned in BSE imagery. Detrital grains partially encased in quartz or in contact with cracks have zones of Th-rich material, indicative of fluid mediated alteration (Hetherington and Harlov, 2008). The REE geochemistry of the pore filling and euhedral monazites show that grains are depleted in HREE, common for authigenic grains. Additionally, the euhedral shape of

some authigenic grains are indicative of low-Th monazite (Cressey et al., 1999). Low-Th monazite may be linked with low grade metamorphism (Overstreet, 1967; Mohr, 1984) and associated with fluids at temperatures <320 °C (Seydoux-Guillaume et al., 2012). However, there may be no correlation between temperature and Th content in monazite (Zhu and O'Nions, 1999). When factoring in increased salinity, normally stable detrital monazite can be altered at temperatures between 260 and 340 °C (Poitrasson et al., 2000). Additionally, Allaz et al. (2013) also suggests that a decrease in temperature during exhumation can induce the precipitation of authigenic monazite. At burial depths of ≤10 km, temperatures in these rocks likely did not exceed 275 °C. Thus, it is reasonable to assume that monazite was initially dissolved at depth by saline fluids and then precipitated as an authigenic phase as temperatures decreased during exhumation (Allaz et al., 2013). We also hypothesize that this decrease in temperature initiated the precipitation of apatite cement, concentrated at the contact between the Mutual and Browns Hole formations.

The final generation of hematite cement may have been the result of iron mobilization during protracted fluid-flow related to partial feldspar dissolution and authigenic mineral precipitation. Porous hematite grains in the volcanic member of the Browns Hole Formation contain pore filling authigenic monazite near the edges and, elsewhere in the unit, hematite cements are observed with interstitial fine-grained clays and authigenic monazite. This coupled with cross cutting relationships suggest that authigenic phosphate, clay, and hematite precipitation events likely occurred coevally (Figs. 14f; 15f; 16). It also supports interpretation that hematite cements were precipitated over a protracted period and in multiple phases.

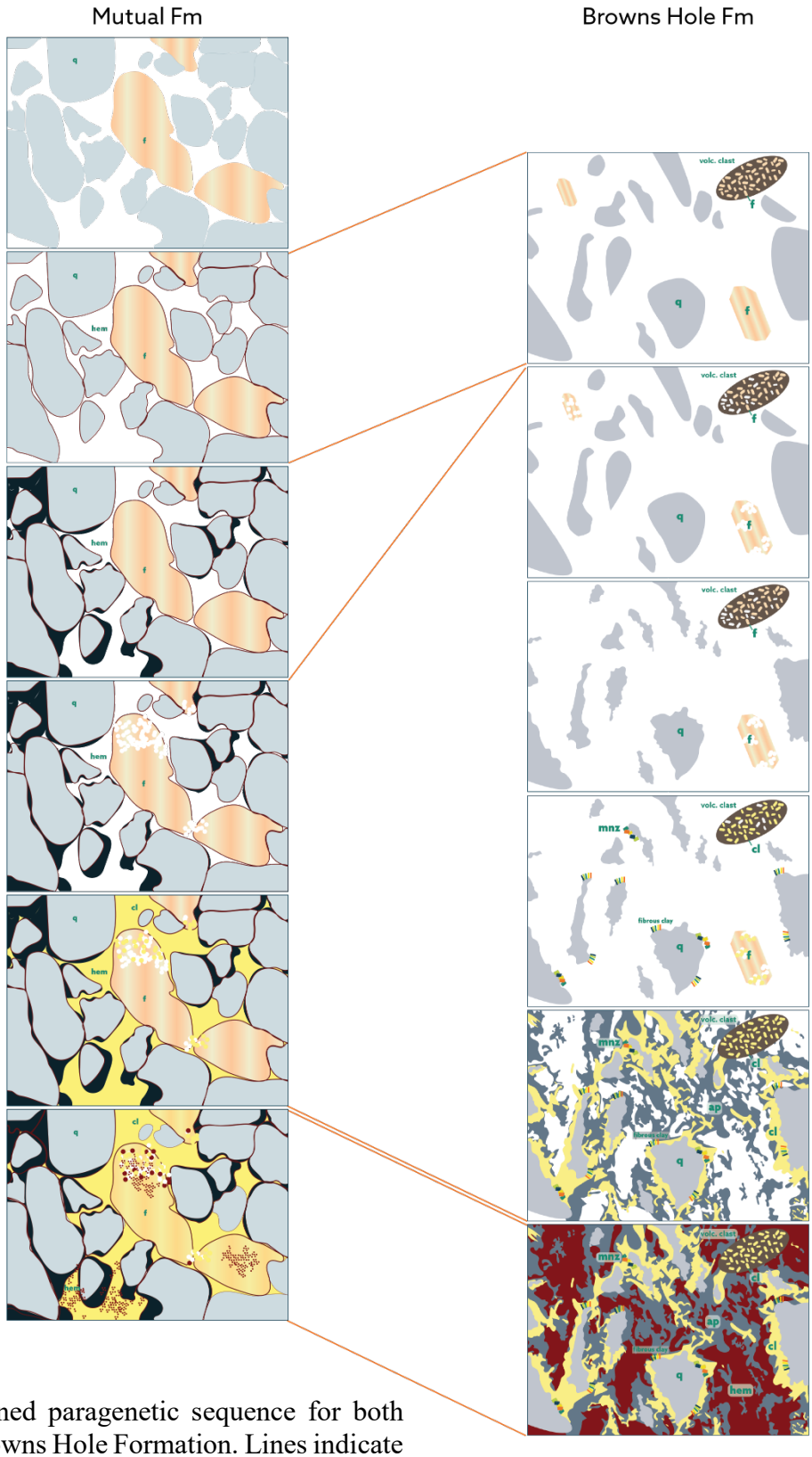

Figure 16. Combined paragenetic sequence for both the Mutual and Browns Hole Formation. Lines indicate places where things are potentially happening simultaneously.

Timing of fluid-rock interaction

Although we lack direct timing constraints of fluid-rock interaction events, we integrate diagenetic events and formation conditions into the known burial history of the Mutual and Browns Hole formations. We consider several regional tectonic events when deriving the possible timing of paragenetic episodes including the Antler Orogeny (ca. 360 – 320 Ma; Trexler and Nitchman, 1990), Ouachita-Marathon orogenies (Pennsylvanian – Permian; Kluth and Coney, 1981), and Sevier-Laramide orogenies (ca. 140 – 50 Ma; Yonkee and Weil, 2015). Because the Sevier-Laramide orogenies are directly related to the uplift of these rocks, we consider the timing of the specific thrust that initiated unroofing, the Willard Thrust (ca. 120 – 90 Ma; Yonkee and Weil, 2015), and the growth of the Wasatch Anticlinorium (75 – 65 Ma; Yonkee and Weil, 2011).

Figure 17 shows a burial and unroofing history and inferred paragenetic sequence for the Browns Hole and Mutual formations. We derived this burial history from average sediment thicknesses recorded on local geologic maps (Crittenden, 1972a; Dover, 1995; Link and Stanford, 1999; Rodgers and Orthberg, 1999; Skipp et al., 2009). This history provides the context for the inferred paragenetic sequence. Diagenetic events including early hematite cements and quartz overgrowths are ubiquitous during the initial stages of lithification and burial compaction (Walker, 1967, 1974). These events are likely unrelated to any major tectonic or fluid-infiltration event. Hematite cements were the result of early iron mobilization and quartz overgrowths formed in response to rising temperatures as burial depths increased. The later generations of hematite cements can be tentatively assigned to later iron mobilization due to fluid-infiltration during middle-to-late Paleozoic basin formation during the Antler and Ouachita-Marathon orogenies to the

west and southeast (current orientation), respectively. The last stages of hematite cement and oxidation likely occurred during the final stages of unroofing during the Sevier-Laramide orogenies and growth of the Wasatch Anticlinorium (Fig. 17).

The initial breakdown of feldspar and hydrolysis to clay minerals also does not require a major fluid-infiltration event because the increase of heat and pressure during burial is sufficient to induce this reaction. However, later stages and major pulses of feldspar dissolution were likely influenced by infiltrating saline fluids during the Antler and Ouachita-Marathon orogenies and formation of the marine Oquirrh basin (Kluth and Coney, 1981; Jansma and Speed, 1993). Additionally, these saline fluids would have dissolved monazite and apatite grains not enclosed in other phases (Allaz et al., 2013). The dissolution of feldspar grains during this time helped produce the chemistry necessary to partially dissolve the edges of quartz grains (Dove and Crerar, 1990). It is possible that whole quartz grains were dissolved in the cm-scale layer of reworked tuff as temperature increased with burial depth, but observations suggest that only the edges of grains were affected. These fluids would have also mobilized the significant amount of iron present in the volcanic member of the Browns Hole Formation. However, iron would have likely stayed in solution until temperatures decreased during unroofing (Fig. 17).

Finally, during Sevier-Laramide unroofing, temperatures decreased and initiated precipitation of authigenic minerals like monazite, coarse-grained clays, as well as apatite and hematite cements. Likewise, fine-grained clay cements would have continued to precipitate during uplift. Major pulses of precipitation were likely influenced by the growth of the Willard Thrust, Wasatch Anticlinorium, and subsequent Wasatch Fault Zone extension (Fig. 17).

Part of the diagenetic history not discussed is hydrothermal alteration related to or directly following the emplacement of the basalt flow that caps the volcanic member of the Browns Hole Formation. This includes alteration at the contact between the basalt flow and underlying volcaniclastic units that resulted in the formation of irregular veins of analcime, quartz, and specular hematite. We speculate that hydrothermal fluids also infiltrated the basalt soon after cooling to produce veins of epidote. Veins acted as weak points in the rock and were activated as slip surfaces during various episodes of faulting, likely related to the final stages of uplift or the initiation of Wasatch Fault Zone. We chose not to consider this event because it only relates to the thin basalt flow with limited impacts on the underlying sediments and, therefore, does not tie into the larger diagenetic history of these formations.

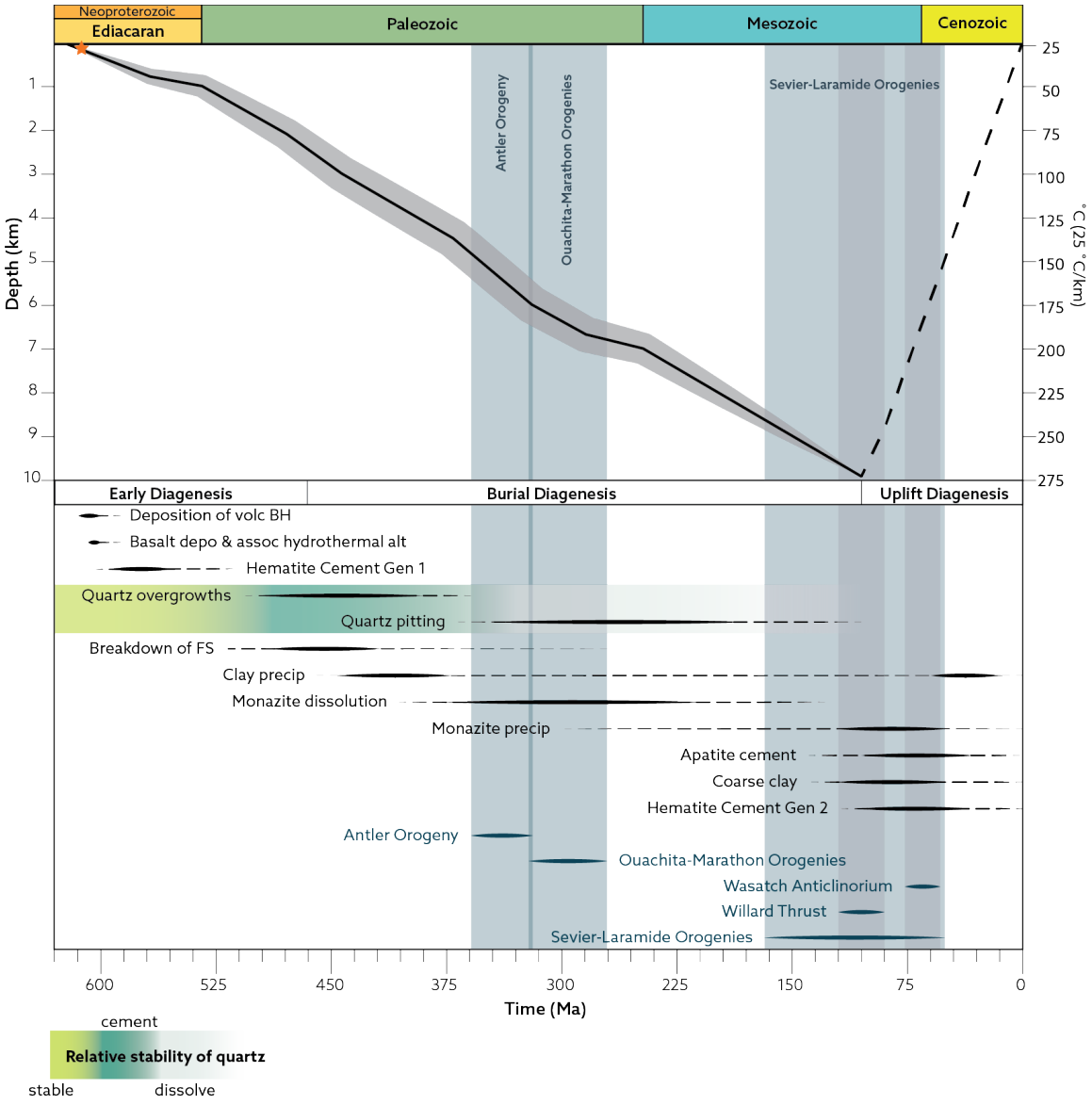

Figure 17. Burial history and paragenesis of the Mutual and Browns Hole Formations. Burial curve, black line, is constructed based on average thicknesses of overlying units, using geologic maps from the surrounding areas (i.e. Crittenden, 1972; Dover, 1995; Skipp et al., 2009). The grey bar outlining the burial curve shows the possibility for depositional thickness errors. The dashed line for uplift indicates that overall path of uplift is unknown and therefore inferred; the actual path is likely not as linear. Orange star indicates timing of deposition for the volcaniclastic member of the Browns Hole Formation as found in this study. Relative stability of quartz was determined by geochemical modeling in PHREEQC. Timing for the Antler, Ouachita-Marathon, and Sevier-Laramide orogenies are based on results from Trexler and Nitchman (1990), Kluth and Coney (1981), and Yonkee and Weil (2015), respectively. Timing for the Willard Thrust and Wasatch Anticlinorium are from Yonkee and Weil (2015) and Yonkee and Weil (2011), respectively.

SUMMARY AND CONCLUSIONS

Improving the maximum depositional age for the Browns Hole Formation has implications for the amount of time available to deposit at least ~1400 m of regional stratigraphy, interpretation of local and regional unconformities, and timing of late Neoproterozoic Laurentian rifting. New detrital apatite U-Pb geochronology reveals the maximum depositional age of the volcanic member of the Browns Hole Formation is 613 ± 12 Ma, consistent with 609 ± 25 Ma U-Pb apatite date acquired from the overlying basalt (Verdel, 2009). The new depositional age places stricter constraints on the amount of time available for the deposition of the underlying Mutual, Inkom, and Caddy Canyon formations. If the lower boundary of the Inkom Formation is temporally anchored by paleovalleys that correspond to sea-level rise associated with the end of the Marinoan glaciation (Levy et al., 1994), then ~1400 m of sediment was deposited over ~37 Myr, ~38 mm/kyr. However, if the diamictites and pink dolostones of the Pocatello and Perry Canyon Formation are related to Marinoan glaciation (Dehler et al., 2011; Isakson, 2017; Isakson et al., in review) and the base of the Caddy Canyon Formation is ca. 635 Ma, then ~1400 m of sediment accumulated over ~22 Myr at a rate of 64 mm/kyr. The second scenario would affect the interpretation for the source of the Inkom paleovalleys and further study of this and correlative formations is required to discern a likely cause.

The revised maximum depositional age also affects interpretations of unconformities between the two members of the Browns Hole Formation and between the Terracotta member of the Browns Hole and overlying Geertsen Canyon Formation. The unconformity that exists between the volcanic member and Terracotta member of the Browns Hole Formation might represent more missing stratigraphic time than previously

thought. Likewise, the unconformity and sequence boundary between the Terracotta member of the Browns Hole Formation and Geertsen Canyon Formation, or Mutual and Camelback Mountain formations, might also represent more missing stratigraphic time than previously understood.

Rifting along the western (current orientation) margin of Laurentia initiated at ~780 Ma with the Gunbarrel event (Harlan et al., 2003) and continued until ~569 Ma (Colpron et al., 2002). Refining the geochronology for the volcanic member of the Browns Hole Formation confirms that rift-related volcanism in this part of the world continued until at least 613 Ma. These proximally sourced volcanic rocks likely represent one of the final episodes of rifting along the western margin of Laurentia prior to transitioning to a passive margin.

Fluid-rock interaction in Neoproterozoic rocks is often cryptic and difficult to constrain due to insufficient datable material. However, a likely paragenetic sequence can be constructed and placed into the context of known geologic events using cross cutting relationships and expected conditions during authigenic mineral formation. In the Mutual and Browns Hole formations, the earliest diagenetic events, hematite dust rims and quartz overgrowths, occurred during initial burial. Increased heat and pressure dissolved feldspar and produced early fine-grained clay cements. The formation of marine basins above these units during the Antler and Ouachita-Marathon orogenies allowed for the infiltration of saline fluids, further dissolving feldspar grains and neutralizing fluids. Prior to neutralization, saline fluids also dissolved or altered detrital monazite and potentially apatite grains. Then, hot neutral fluids partially dissolved quartz grains, leaving a pitted texture along the edges of grains. The Sevier-Laramide orogenies and initiation of the

Willard Thrust and, later, growth of the Wasatch Anticlinorium led to unroofing and, therefore, cooling. Cooler temperatures then allowed for the precipitation of authigenic minerals including apatite, monazite, coarse and fine clays, and later hematite cements.

REFERENCES

Allaz, J., Selleck, B., Williams, M.L., and Jercinovic, M.J., 2013, Microprobe analysis and dating of monazite from the Potsdam Formation, New York: A progressive record of chemical reaction and fluid interaction: American Mineralogist, v. 98, p. 1106–1119, doi: 10.2138/am.2013.4304.

Ayers, J.C., Loflin, M., Miller, C.F., Barton, M.D., and Coath, C., 2004, Dating fluid infiltration using monazite: Proceedings of the Eleventh International Symposium on Water-Rock Interaction, p. 247–251, http://sims.ess.ucla.edu/PDF/Ayers_et_al_2004.pdf.

Ayers, J.C., and Watson, E.B., 1991, Solubility of apatite, monazite, zircon, and rutile in super critical aqueous fluids with implications for subduction zone geochemistry: Philosophical Transactions: Physical Sciences and Engineering, v. 335, p. 365–375, https://www.jstor.org/stable/53707 (accessed September 2018).

Balgord, E.A., Yonkee, W.A., Link, P.K., and Fanning, C.M., 2013, Stratigraphic, geochronologic, and geochemical record of the Cryogenian Perry Canyon ormation, northern Utah: Implications for Rodinia rifting and Snowball Earth glaciation: Bulletin of the Geological Society of America, v. 125, p. 1442–1467, doi: 10.1130/B30860.1.

Barberi, F., Santacroce, R., and Varet, J., 1982, Chemical aspects of rift magmatism: Continental and oceanic rifts, p. 223–258, http://onlinelibrary.wiley.com/doi/10.1029/GD008p0223/summary.

Boger, S.D., and Miller, J.M.L., 2004, Terminal suturing of Gondwana and the onset of the Ross-Delamerian Orogeny: The cause and effect of an Early Cambrian reconfiguration of plate motions: Earth and Planetary Science Letters, v. 219, p. 35–48, doi: 10.1016/S0012-821X(03)00692-7.

Boyce, J.W., Hodges, K. V., Olszewski, W.J., and Jercinovic, M.J., 2005, He diffusion in monazite: Implications for (U-Th)/He thermochronometry: Geochemistry, Geophysics, Geosystems, v. 6, doi: 10.1029/2005GC001058.

Cawood, P.A., Kröner, A., and Pisarevsky, S., 2006, Precambrian plate tectonics: Criteria and evidence: GSA Today, v. 16, p. 4–11, doi: 10.1130/GSAT01607.1.

Christie-Blick, N., 1982, Upper Proterozoic and Lower Cambrian rocks of the Sheeprock Mountains, Utah: Regional correlation and significance: Bulletin of the Geological Society of America, v. 93, p. 735–750, doi: 10.1130/0016-7606(1982)93<735:UPALCR>2.0.CO;2.

Christie-Blick, N., and Levy, M., 1989, Concepts of Sequence Stratigraphy, with Examples from Strata of Late Proterozoic and Cambrian Age in the Western United States, *in* Late Proterozoic and Cambrian Tectonics, Sedimentation, and Record of Metazoan Radiation in the Western United States: Pocatello, Idaho, to Reno, Nevada 20–29 July, 1989, p. 23–37, doi: 10.1029/FT331p0023.

Christie-Blick, N., Grotzinger, J.P., and von der Borch, C.C., 1988, Sequence stratigraphy in Proterozoic successions: Geology, v. 16, p. 100–104, doi: 10.1130/0091-7613(1988)016<0100:SSIPS>2.3.CO;2.

Christie-Blick, N., and Levy, M., 1989, Stratigraphic and tectonic framework of upper Proterozoic and Cambrian rocks in the western United States, *in* Late Proterozoic and Cambrian Tectonics, Sedimentation, and Record of Metazoan Radiation in the Western United States: Pocatello, Idaho, to Reno, Nevada 20-29 July, 1989, Washington, D. C., American Geophysical Union, p. 7–21, doi: 10.1029/FT331p0007.

Collins, A.S., and Pisarevsky, S.A., 2005, Amalgamating eastern Gondwana: The evolution of the Circum-Indian Orogens: Earth-Science Reviews, v. 71, p. 229–270, doi: 10.1016/j.earscirev.2005.02.004.

Colpron, M., Logan, J.M., and Mortensen, J.K., 2002, U-Pb zircon age constraint for late Neoproterozoic rifting and initiation of the lower Paleozoic passive margin of western Laurentia: Canadian Journal of Earth Sciences, v. 39, p. 133–143, doi: 10.1139/e01-069.

Condon, D., Zhu, M., Bowring, S., Wang, W., Yang, A., and Jin, Y., 2005, U-Pb ages

from the Neoproterozoic Doushantuo Formation, China: Science, v. 308, p. 95–98, https://www-jstor-org.dist.lib.usu.edu/stable/pdf/3841402.pdf?refreqid=excelsior%3Ada5fed8265739f94d36c4f88acb67807 (accessed February 2019).

Cressey, G., Wall, F., and Cressey, B.A., 1999, Differential REE uptake by sector growth of monazite: Mineralogical Magazine, v. 63, p. 813–828, http://minmag.geoscienceworld.org/content/63/6/813.abstract.

Crittenden, M.D., 1972a, Geologic Map of the Browns Hole 7.5' Quadrangle, Utah: United States Geological Survey,.

Crittenden, M.D., 1972b, Willard thrust and the Cache Allochthon, Utah: Bulletin of the Geological Society of America, v. 83, p. 2871–2880, doi: 10.1130/0016-7606(1972)83[2871:WTATCA]2.0.CO;2.

Crittenden Jr, M.D., and Wallace, C.A., 1973, Possible equivalents of the Belt Supergroup in Utah, *in* Belt symposium, v. 1, p. 116–138.

Crittenden, M.D., Schaeffer, F.E., Trimble, D.E., and Woodward, L.A., 1971, Nomenclature and correlation of some upper precambrian and basal Cambrian sequences in western Utah and southeastern Idaho: Bulletin of the Geological Society of America, v. 82, p. 581–602, doi: 10.1130/0016-7606(1971)82[581:NACOSU]2.0.CO;2.

Dalziel, I.W.D., and Soper, N.J., 2001, Neoproterozoic Extension on the Scottish Promontory of Laurentia: Paleogeographic and Tectonic Implications: The Journal of Geology, v. 109, p. 299–317, doi: 10.1086/319974.

DeCelles, P.G., 2004, Late Jurassic to Eocene evolution of the cordilleran thrust belt and foreland basin system, western U.S.A.: American Journal of Science, v. 304, p. 105–168, http://ajsonline.org/cgi/content/abstract/304/2/105.

Dehler, C.M., Anderson, K., and Nagy, R., 2011, New descriptions of the cap dolostone and associated strata, Neoproterozoic Pocatello Formation, southeastern Idaho, U.S.A.: The Geological Society of America, v. Field Guid, p. 181–192, doi:

10.1130/2011.0021(08).

Dehler, C., Gehrels, G., Porter, S., Heizler, M., Karlstrom, K., Cox, G., Crossey, L., and Timmons, M., 2017, Synthesis of the 780-740 ma Chuar, Uinta Mountain, and Pahrump (ChUMP) groups, western USA: Implications for Laurentia-wide cratonic marine basins: Bulletin of the Geological Society of America, v. 129, p. 607–624, doi: 10.1130/B31532.1.

Dehler, C.D., Yonkee, W.A., Hayes, D., Nagy, R., Link, P.K., Balgord, E., and Keeley, J., 2012, The Cryogenian-Ediacaran tectono-stratigraphic, paleoenvironmental, and biologic record of northern Utah and southeastern Idaho, *in* Geological Society of London International Symposium—The Neoproterozoic Era, Evolution, Glaciation and Oxygenation: Fermor, v. 12, p. 153–154.

Dempster, T.J., Jolivet, M., Tubrett, M.N., and Braithwaite, C.J.R., 2003, Magmatic zoning in apatite: A monitor of porosity and permeability change in granites: Contributions to Mineralogy and Petrology, v. 145, p. 568–577, doi: 10.1007/s00410-003-0471-0.

Dickinson, W.R., 2002, The Basin and Range Province as a Composite Extensional Domain: International Geology Review, v. 44, p. 1–38.

Dove, P.M., and Crerar, D.A., 1990, Kinetics of quartz dissolution in electrolyte solutions using a hydrothermal mixed flow reactor: Geochimica et Cosmochimica Acta, v. 54, p. 955–969, doi: 10.1016/0016-7037(90)90431-J.

Dover, J.H., 1995, Geologic Map of the Logan 30’ x 60’ Quadrangle Cache and Rich Counties, Utah and Lincoln and Unita Counties, Wyoming: United States Geological Survey, p. 80225.

Fanning, C.M., and Link, P.K., 2004, U-Pb SHRIMP ages of Neoproterozoic (Sturtian) glaciogenic Pocatello Formation, southeastern Idaho: Geology, v. 32, p. 881–884, doi: 10.1130/G20609.1.

Fitzsimons, I.C.W., 2003, Proterozoic basement provinces of southern and southwestern Australia, and their correlation with Antarctica: Geological Society, London, Special

Publications, v. 206, p. 93–130, doi: 10.1144/GSL.SP.2003.206.01.07.

Galbraith, R.F., 2005, Statistics for Fission Track Analysis: Chapman and Hall/CRC, Chapman & Hall/CRC Interdisciplinary Statistics Series, v. 20054283, 240 p., doi: 10.1201/9781420034929.

Gehrels, G.E., Valencia, V.A., and Ruiz, J., 2008, Enhanced precision, accuracy, efficiency, and spatial resolution of U-Pb ages by laser ablation-multicollector-inductively coupled plasma-mass spectrometry: Geochemistry, Geophysics, Geosystems, v. 9, p. 1–13, doi: 10.1029/2007GC001805.

Gonçalves, G.O., Lana, C., Scholz, R., Buick, I.S., Gerdes, A., Kamo, S.L., Corfu, F., Marinho, M.M., Chaves, A.O., Valeriano, C., and Nalini, H.A., 2016, An assessment of monazite from the Itambé pegmatite district for use as U-Pb isotope reference material for microanalysis and implications for the origin of the "Moacyr" monazite: Chemical Geology, v. 424, p. 30–50, doi: 10.1016/j.chemgeo.2015.12.019.

Harlan, S.S., Heaman, L., LeCheminant, A.N., and Premo, W.R., 2003, Gunbarrel mafic magmatic event: A key 780 Ma time marker for Rodinia plate reconstructions: Geology, v. 31, p. 1053–1056, doi: 10.1130/G19944.1.

Hetherington, C.J., and Harlov, D.E., 2008, Metasomatic thorite and uraninite inclusions in xenotime and monazite from granitic pegmatites, Hidra anorthosite massif, southwestern Norway: Mechanics and fluid chemistry: American Mineralogist, v. 93, p. 806–820, doi: 10.2138/am.2008.2635.

Hiatt, E.E., Kyser, T.K., Fayek, M., Polito, P., Holk, G.J., and Riciputi, L.R., 2007, Early quartz cements and evolution of paleohydraulic properties of basal sandstones in three Paleoproterozoic continental basins: Evidence from in situ δ18O analysis of quartz cements: Chemical Geology, v. 238, p. 19–37, doi: 10.1016/j.chemgeo.2006.10.012.

Hodges, K.V., 2005, 40Ar/39Ar Thermochronology of Detrital Minerals: Reviews in Mineralogy and Geochemistry, v. 58, p. 239–257, doi: 10.2138/rmg.2005.58.9.

Hoffman, P.F., 1991, Did the breakout of Laurentia turn Gondwanaland inside out? Science, v. 252, p. 1409–1412, https://www-jstor-org.dist.lib.usu.edu/stable/pdf/2875916.pdf?refreqid=excelsior%3Ae40fa7c66dc81c473bbe36e1201d38f4 (accessed December 2018).

Hoffman, P.F., Abbot, D.S., Ashkenazy, Y., Benn, D.I., Brocks, J.J., Cohen, P.A., Cox, G.M., Creveling, J.R., Donnadieu, Y., Erwin, D.H., Fairchild, I.J., Ferreira, D., Goodman, J.C., Halverson, G.P., et al., 2017, Snowball Earth climate dynamics and Cryogenian geology-geobiology: Science Advances, v. 3, p. e1600983, doi: 10.1126/sciadv.1600983.

Hoffman, P.F., and Li, Z.X., 2009, A palaeogeographic context for Neoproterozoic glaciation: Palaeogeography, Palaeoclimatology, Palaeoecology, v. 277, p. 158–172, doi: 10.1016/j.palaeo.2009.03.013.

Hoffmann, K.H., Condon, D.J., Bowring, S.A., and Crowley, J.L., 2004, U-Pb zircon date from the Neoproterozoic Ghaub Formation Namibia: Constraints on Marinoan glaciation: Geology, v. 32, p. 817–820, doi: 10.1130/G20519.1.

Hyodo, A., Kozdon, R., Pollington, A.D., and Valley, J.W., 2014, Evolution of quartz cementation and burial history of the Eau Claire Formation based on in situ oxygen isotope analysis of quartz overgrowths: Chemical Geology, v. 384, p. 168–180, doi: 10.1016/j.chemgeo.2014.06.021.

Isakson, V.H., 2017, Geochronology of the Tectonic, Stratigraphic, and Magmatic Evolution of Neoproterozoic to Early Paleozoic, North American Cordillera and Cryogenian Glaciation: Boise State Universitys.

Isakson, V.H., Schmitz, M.D., Dehler, C.M., Macdonald, F.A., and Yonkee, W.A. Epiclastic versus pyroclastic? Using tandem in situ and isotope dilution U-Pb zircon geochronology to improve age models for the Cryogenian Pocatello Formation, southeastern Idaho: Geosphere,.

Jacobs, J., and Thomas, R.J., 2004, Himalayan-type indenter-escape tectonics model for the southern part of the late Neoproterozoic-early Paleozoic East African-Antarctic

orogen: Geology, v. 32, p. 721–724, doi: 10.1130/G20516.1.

Jansma, P.E., and Speed, R.C., 1993, Deformation, dewatering, and decollement development in the Antler foreland basin during the Antler Orogeny: Geology, v. 21, p. 1035–1038, doi: 10.1130/0091-7613(1993)021<1035:DDADDI>2.3.CO;2.

Keeley, J.A., Link, P.K., Fanning, C.M., and Schmitz, M.D., 2012, Pre- to synglacial rift-related volcanism in the Neoproterozoic (Cryogenian) Pocatello Formation, SE Idaho: New SHRIMP and CA-ID-TIMS constraints: Lithosphere, v. 5, p. 128–150, doi: 10.1130/L226.1.

Kluth, C.F., and Coney, P.J., 1981, Plate tectonics of the Ancestral Rocky Mountains: Geology, v. 9, p. 10–15, doi: 10.1130/0091-7613(1981)9<10.

Levy, M., Christie-Blick, N., and Link, P.K., 1994, Neoproterozoic incised valley of the eastern Great basin, Utah and Idaho: fluvial response to changes in depositional base level: Incised-valley systems: origin and sedimentary sequences, v. 51, p. 3369–3382.

Lewis, A.J., Palmer, M.R., Sturchio, N.C., and Kemp, A.J., 1997, The rare earth element geochemistry of acid-sulphate and acid-sulphate-chloride geothermal systems from Yellowstone National Park, Wyoming, USA: Geochimica et Cosmochimica Acta, v. 61, p. 695–706, doi: 10.1016/S0016-7037(96)00384-5.

Li, Z.X., Bogdanova, S. V., Collins, A.S., Davidson, A., De Waele, B., Ernst, R.E., Fitzsimons, I.C.W., Fuck, R.A., Gladkochub, D.P., Jacobs, J., Karlstrom, K.E., Lu, S., Natapov, L.M., Pease, V., et al., 2008, Assembly, configuration, and break-up history of Rodinia: A synthesis: Precambrian Research, v. 160, p. 179–210, doi: 10.1016/j.precamres.2007.04.021.

Li, Z.X., Li, X.H., Kinny, P.D., Wang, J., Zhang, S., and Zhou, H., 2003, Geochronology of Neoproterozoic syn-rift magmatism in the Yangtze Craton, South China and correlations with other continents: Evidence for a mantle superplume that broke up Rodinia: Precambrian Research, v. 122, p. 85–109, doi: 10.1016/S0301-9268(02)00208-5.

Link, P.K., 1982, Geology of the Upper Proterozoic Pocatello Formation, Bannock Range, Southeastern Idaho: University of California, Santa Barbara.

Link, P., Jansen, S., Halimdihardja, P., Lande, A., and Zahn, P., 1987, Stratigraphy of the Brigham Group (Late Proterozoic-Cambrian), Bannock, Portneuf, and Bear River Ranges, southeastern Idaho, *in* The Thrust Belt Revisited; 38th Annual Field Conference Guidebook, Wyoming Geological Association, p. 133–148, http://archives.datapages.com/data/wga/data/045/045001/133_wga0450133.htm (accessed September 2016).

Link, P.K., and Stanford, L.R., 1999, Geologic Map Compilation of the Pocatello 30' x 60' Quadrangle, Idaho: United States Geological Survey,.

Ludwig, K.R., 2011, Isoplot 3.75: Berkeley, CA, Berkeley Geochronology Center.

Mahon, R.C., Dehler, C.M., Link, P.K., Karlstrom, K.E., and Gehrels, G.E., 2014, Geochronologic and stratigraphic constraints on the Mesoproterozoic and Neoproterozoic Pahrump Group, Death Valley, California: A record of the assembly, stability, and breakup of Rodinia: Bulletin of the Geological Society of America, v. 126, p. 652–664, doi: 10.1130/B30956.1.

Le Maitre, R.W., Bateman, D., Dudek, A., and Keller, J., 1989, Igneous Rocks: a Classification and Glossary of Terms: Recommendations of the International Union of Geological Sciences Subcommission on the Systematics of Igneous Rocks.: Oxford, Boston, Blackwell, doi: 10.1017/S0016756803388028.

McBride, E.F., 1989, Quartz cement in sandstones: a review: Earth Science Reviews, v. 26, p. 69–112, doi: 10.1016/0012-8252(89)90019-6.

Meert, J.G., 2003, A synopsis of events related to the assembly of the eastern Gondwana: Tectonophysics, v. 362, p. 1–40, doi: 10.1016/S0040-1951(02)00629-7.

Mohr, D.W., 1984, Zoned porphyroblasts of metamorphic monazite in the Anakeesta formation, Great Smoky Mountains, North Carolina.: American Mineralogist, v. 69, p. 98–103, http://www.minsocam.org/ammin/AM69/AM69_98.pdf (accessed September 2018).

Oelkers, E.H., and Poitrasson, F., 2002, An experimental study of the dissolution stoichiometry and rates of a natural monazite as a function of temperature from 50 to 230 °C and pH from 1.5 to 10: Chemical Geology, v. 191, p. 73–87, doi: 10.1016/S0009-2541(02)00149-3.

Overstreet, W.C., 1967, The geologic occurrence of monazite: Geological Survey, v. 530, 327 p.

Parkhurst, D.L., and Appelo, C.A.J., 2005, Description of Input and Examples for PHREEQC Version 3—A Computer Program for Speciation, Batch-Reaction, One-Dimensional Transport, and Inverse Geochemical Calculations:, doi: 10.1016/0029-6554(94)90020-5.

Paulsson, O., and Andreasson, P.G., 2002, Attempted break-up of Rodinia at 850 Ma: geochronological evidence from the Seve-Kalak Superterrane, Scandinavian Caledonides: Journal of the Geological Society, v. 159, p. 751–761, doi: 10.1144/0016-764901-156.

Peterson, D.A., and Clark, D.L., 1974, Trace Fossils Plagiogmus and Skolithos in the Tintic Quartzite (Middle Cambrian) of Utah: Journal of Paleontology, v. 48, p. 766–768.

Poitrasson, F., Chenery, S., and Shepherd, T.J., 2000, Electron microprobe and LA-ICP-MS study of monazite hydrothermal alteration: Implications for U-Th-Pb geochronology and nuclear ceramics: Geochimica et Cosmochimica Acta, v. 64, p. 3283–3297, doi: 10.1016/S0016-7037(00)00433-6.

Poitrasson, F., Oelkers, E., Schott, J., and Montel, J.M., 2004, Experimental determination of synthetic NdPO4 monazite end-member solubility in water from 21 C to 300 C: Implications for rare earth element mobility in crustal fluids: Geochimica et Cosmochimica Acta, v. 68, p. 2207–2221, doi: 10.1016/j.gca.2003.12.010.

Rakovan, J., and Reeder, R.J., 1994, Differential incorporation of trace-elements and dissymmetrization in apatite – the role of surface-structure during growth: American

Mineralogist, v. 79, p. 892–903, http://www.minsocam.org/ammin/AM79/AM79_892.pdf (accessed August 2018).

Reichow, M.K., Saunders, A.D., White, R. V., Pringle, M.S., Al'Mukhamedov, A.I., Medvedev, A.I., and Kirda, N.P., 2002, 40Ar/39Ar dates from the West Siberian Basin: Siberian flood basalt province doubled: Science, v. 296, p. 1846–1849, doi: 10.1126/science.1071671.

Rodgers, D.W., and Orthberg, K.L., 1999, Geologic Map of the Pocatello South 7.5' Quadrangle, Bannock and Power Counties, Idaho: United States Geological Survey,.

Rooney, A.D., Macdonald, F.A., Strauss, J. V., Dudas, F.O., Hallmann, C., and Selby, D., 2014, Re-Os geochronology and coupled Os-Sr isotope constraints on the Sturtian snowball Earth: Proceedings of the National Academy of Sciences, v. 111, p. 51–56, doi: 10.1073/pnas.1317266110.

Sadler, P.M., 1981, Sediment Accumulation Rates and the Completeness of Stratigraphic Sections: The Journal of Geology, v. 89, p. 569–584, doi: 10.1086/628623.

Seydoux-Guillaume, A.M., Montel, J.M., Bingen, B., Bosse, V., de Parseval, P., Paquette, J.L., Janots, E., and Wirth, R., 2012, Low-temperature alteration of monazite: Fluid mediated coupled dissolution-precipitation, irradiation damage, and disturbance of the U-Pb and Th-Pb chronometers: Chemical Geology, v. 330–331, p. 140–158, doi: 10.1016/j.chemgeo.2012.07.031.

Shields-Zhou, Graham, A., Porter, S., and Halverson, G.P., 2016, A new rock-based definition for the Cryogenian Period (circa 720 - 635 Ma): Episodes, v. 39, p. 1–10, doi: 10.18814/epiiugs/2016/v39i1/XXXXX.

Skipp, B., Snider, L.G., Janecke, S.U., and Kuntz, M. a, 2009, Geologic map of the Arco 30 x 60 minute quadrangle, Idaho: United States Geological Survey, doi: 10.1029/2003GC000661.Wood.

Smith, E.F., MacDonald, F.A., Crowley, J.L., Hodgin, E.B., and Schrag, D.P., 2015, Tectonostratigraphic evolution of the c. 780–730 Ma Beck Spring Dolomite: Basin Formation in the core of Rodinia: Geological Society, London, Special Publications,

v. 424, p. 213–239, doi: 10.1144/SP424.6.

Sorensen, M.L., and Crittenden, M.D., 1979, Geologic Map of the Huntsville Quadrangle, Weber and Cache Counties, Uah:

Stacey, J.S., and Kramers, J.D., 1975, Approximation of terrestrial lead isotope evolution by a two-stage model: Earth and Planetary Science Letters, v. 26, p. 207–221, doi: 10.1016/0012-821X(75)90088-6.

Stewart, J.H., 1972, Initial Deposits in the Cordilleran Geosyncline: Evidence of a Late Precambrian (<850 m.y.) Continental Separation: Geological Society of America Bulletin, p. 1345–1360.

Thomson, S.N., Gehrels, G.E., Ruiz, J., and Buchwaldt, R., 2012, Routine low-damage apatite U-Pb dating using laser ablation-multicollector- ICPMS: Geochemistry, Geophysics, Geosystems, v. 13, p. 1–23, doi: 10.1029/2011GC003928.

Trexler, J.H., and Nitchman, S.P., 1990, Sequence stratigraphy and evolution of the Antler foreland basin, east-central Nevada: Geology, v. 18, p. 422–425.

Verdel, C., 2009, I: Cenozoic Geology of Iran: an Integrated Study of Extensional Tectonics and Related Volcanism II: Ediacaran stratigraphy of the North American Cordillera: new observations from eastern California and northern Utah: California Institute of Technology, 287 p.

Vermeesch, P., 2009, RadialPlotter: A Java application for fission track, luminescence and other radial plots: Radiation Measurements, v. 44, p. 409–410, doi: 10.1016/j.radmeas.2009.05.003.

Walker, T.R., 1967, Formation of Red Beds in Modern and Ancient Deserts: Geological Society of America Bulletin, v. 78, p. 353–368.

Walker, T.R., 1974, Formation of red beds in moist tropical climates: A hypothesis: Bulletin of the Geological Society of America, v. 85, p. 633–638, doi: 10.1130/0016-7606(1974)85<633:FORBIM>2.0.CO;2.

Wilkinson, M., and Haszeldine, R.S., 1996, Aluminium Loss During Sandstone

Diagenesis: Journal of the Geological Society, v. 153, p. 657–660, doi: 10.1051/0004-6361:20064995.

Wilkinson, M., Milliken, K.L., and Haszeldine, R.S., 2001, Systematic destruction of K-feldspar in deeply buried rift and passive margin sandstones: Journal of the Geological Society, v. 158, p. 675–683, doi: 10.1144/jgs.158.4.675.

Yonkee, W.A., 1992, Basement-cover relations, Sevier orogenic belt, northern Utah: Geological Society of America Bulletin, v. 104, p. 280–302, doi: 10.1130/0016-7606(1992)104<0280:BCRSOB>2.3.CO;2.

Yonkee, A., 2005, Strain patterns within part of the Willard thrust sheet, Idaho-Utah-Wyoming thrust belt: Journal of Structural Geology, v. 27, p. 1315–1343, doi: 10.1016/j.jsg.2004.06.014.

Yonkee, W.A., Dehler, C.D., Link, P.K., Balgord, E.A., Keeley, J.A., Hayes, D.S., Wells, M.L., Fanning, C.M., and Johnston, S.M., 2014, Tectono-stratigraphic framework of Neoproterozoic to Cambrian strata, west-central U.S.: Protracted rifting, glaciation, and evolution of the North American Cordilleran margin: Earth-Science Reviews, v. 136, p. 59–95, doi: 10.1016/j.earscirev.2014.05.004.

Yonkee, W.A., and Weil, A.B., 2011, Evolution of the Wyoming Salient of the Sevier Fold- Thrust Belt, Northern Utah To Western Wyoming: 2011 UGA Publication 40—Sevier Thrust Belt: Northern and Central Utah and Adjacent Areas, p. 1–56.

Yonkee, W.A., and Weil, A.B., 2015, Tectonic evolution of the Sevier and Laramide belts within the North American Cordillera orogenic system: Earth-Science Reviews, v. 150, p. 531–593, doi: 10.1016/j.earscirev.2015.08.001.

Zhu, X.K., and O'Nions, R.K., 1999, Monazite chemical composition: Some implications for monazite geochronology: Contributions to Mineralogy and Petrology, v. 137, p. 351–363, doi: 10.1007/s004100050555.

APPENDICES

Appendix A. Raw Monazite EMPA Data

Table A1: Values are in weight percent.

Sample	Grain	O	Si	S	P	K	Ca	Pb	Th	U	Fe	La	Ce	Nd	Pr	Sm	Eu	Tb	Dy	Gd	Er	Yb	Y	TOTAL
66mf_4	m1	26.09	0.12	0.27	12.48	0.01	0.65	bld	0.04	bld	NA	7.66	24.06	14.67	3.49	2.46	0.57	0.03	0.08	0.97	bld	bld	0.21	93.71
		25.69	0.11	0.22	12.34	bld	0.61	bld	0.02	bld	NA	8.14	24.03	14.10	3.35	2.20	0.53	0.02	0.08	0.89	bld	bld	0.15	92.36
		25.53	0.15	0.46	11.83	bld	0.84	bld	0.04	bld	NA	11.33	26.65	10.61	3.02	1.10	0.25	bld	bld	0.33	bld	bld	0.01	92.02
	m2	25.78	0.33	0.42	12.20	0.16	0.80	bld	0.24	bld	NA	8.04	23.09	13.07	3.11	1.96	0.47	0.03	0.07	0.80	bld	bld	0.30	90.76
		25.69	0.04	0.98	11.50	0.13	1.50	bld	0.17	bld	NA	6.54	22.76	14.60	3.44	2.41	0.49	0.01	0.05	0.85	bld	bld	0.17	91.24
		25.73	0.06	0.71	11.87	0.14	1.19	bld	0.22	bld	NA	6.26	22.21	15.43	3.38	2.68	0.53	bld	0.06	0.97	bld	bld	0.24	91.53
		25.77	0.05	0.36	12.28	0.12	0.74	bld	0.23	bld	NA	7.96	23.84	13.85	3.30	2.09	0.54	0.02	0.08	0.91	bld	bld	0.26	92.31
		25.84	0.09	0.32	12.31	0.10	0.58	bld	0.22	bld	NA	9.75	24.79	12.32	3.00	1.86	0.51	0.03	0.08	0.89	bld	bld	0.23	92.81
	m3a	27.84	0.24	0.72	12.79	0.03	1.28	bld	0.03	0.02	NA	9.03	26.81	13.36	3.51	1.69	0.38	0.01	0.04	0.54	0.00	0.01	0.20	98.52
		27.29	0.26	0.83	12.19	0.05	1.58	bld	0.04	0.02	NA	5.92	22.86	17.20	3.76	3.45	0.67	0.04	0.10	1.14	0.01	0.01	0.21	97.64
		27.23	0.64	0.49	12.37	0.04	1.04	bld	0.10	0.02	NA	8.44	24.94	14.46	3.56	2.26	0.46	0.02	0.07	0.77	0.01	0.03	0.16	97.11
		27.73	0.53	0.19	13.11	0.04	0.55	bld	0.01	0.00	NA	8.08	25.07	15.43	3.72	2.64	0.64	0.04	0.11	1.11	0.02	bld	0.28	99.27
		27.05	0.33	0.47	12.41	0.05	1.05	bld	0.10	0.01	NA	6.76	23.23	17.23	3.72	3.29	0.63	0.04	0.08	1.08	0.01	bld	0.16	97.72
	m3b	26.97	0.12	0.56	12.36	0.02	0.99	bld	0.05	0.01	NA	9.80	26.91	13.13	3.42	1.88	0.52	0.05	0.11	0.80	0.01	0.02	0.11	97.83
		26.90	0.10	0.70	12.19	0.02	1.24	bld	0.02	0.01	NA	9.77	27.17	12.90	3.53	1.56	0.34	0.02	0.04	0.50	bld	0.02	0.03	97.06
		26.69	0.13	0.44	12.32	0.02	0.81	bld	0.15	bld	NA	11.85	28.25	11.11	3.22	1.28	0.34	0.04	0.05	0.44	0.01	0.02	bld	97.14
		26.00	0.12	0.62	11.56	bld	1.16	0.00	0.08	bld	NA	8.76	26.32	14.01	3.61	2.07	0.53	0.05	0.10	0.84	0.01	0.01	bld	95.81
		26.87	0.14	0.46	12.40	bld	0.85	bld	0.04	bld	NA	9.72	27.01	13.14	3.46	1.98	0.55	0.06	0.12	0.90	0.01	0.02	0.08	97.77
	m5	26.35	0.46	0.44	11.87	0.06	0.73	bld	0.09	bld	NA	11.35	27.53	11.70	3.31	1.41	0.31	0.02	0.03	0.44	bld	bld	bld	96.05
		26.40	0.12	0.23	12.29	0.03	0.44	bld	0.36	bld	NA	11.43	27.93	12.04	3.25	1.72	0.44	0.05	0.09	0.76	bld	bld	0.06	97.61
		27.14	0.15	0.84	12.11	bld	1.59	bld	0.03	0.00	NA	6.88	24.25	16.75	3.84	2.78	0.48	0.02	0.05	0.77	bld	0.01	0.05	97.70
		27.22	0.11	0.59	12.32	0.01	1.13	bld	0.03	0.01	NA	6.56	24.63	17.63	4.09	3.33	0.67	0.04	0.09	1.11	0.01	0.02	0.13	99.73
	m6	26.44	0.03	0.53	12.12	0.05	0.86	bld	0.38	0.00	NA	10.86	27.10	11.78	3.19	1.72	0.49	0.05	0.10	0.79	bld	bld	0.12	96.59
		26.83	0.03	0.85	11.90	0.06	1.33	bld	0.23	0.01	NA	9.64	26.89	13.15	3.52	1.80	0.45	0.04	0.08	0.70	bld	bld	0.11	97.62
		26.72	0.05	0.39	12.40	0.09	0.94	bld	0.25	0.03	NA	8.28	25.35	15.25	3.70	2.42	0.59	0.03	0.11	0.99	bld	0.00	0.16	97.74
		27.06	0.04	0.22	12.78	0.08	0.59	bld	0.27	0.03	NA	10.87	27.01	12.99	3.39	2.00	0.57	0.07	0.12	1.00	0.01	0.00	0.19	99.30
		26.92	0.05	0.17	12.75	0.09	0.49	bld	0.33	0.03	NA	11.06	26.72	12.90	3.28	2.10	0.58	0.07	0.15	1.08	0.00	0.01	0.21	98.98
66mf_5	m1	27.03	0.02	0.76	12.18	0.09	1.36	bld	0.01	bld	NA	14.62	28.74	8.78	2.63	0.83	0.18	0.03	0.01	0.30	bld	0.01	0.01	97.58
		26.89	0.03	0.77	12.07	0.08	1.43	bld	0.01	0.00	NA	14.66	28.85	8.58	2.56	0.76	0.15	0.00	0.02	0.24	bld	0.01	0.00	97.10
		26.79	0.01	0.66	12.12	0.08	1.24	bld	0.01	bld	NA	11.35	29.05	11.32	3.02	1.14	0.21	0.02	0.01	0.38	bld	0.00	0.03	97.43
	m2	27.33	0.03	0.47	12.58	0.01	1.07	bld	0.01	0.00	NA	11.88	28.74	12.21	3.14	1.34	0.28	0.03	0.04	0.48	0.00	0.01	0.05	99.72
		27.65	0.02	0.59	12.66	0.01	1.36	bld	bld	0.01	NA	10.39	29.20	12.58	3.30	1.47	0.30	0.03	0.04	0.47	0.01	0.01	0.08	100.17
		27.65	0.08	0.53	12.77	bld	1.29	bld	bld	0.00	NA	7.86	26.44	15.94	3.55	2.28	0.49	0.04	0.08	0.90	0.01	0.01	0.12	99.96
	m6	27.03	0.02	0.43	12.46	bld	1.31	bld	bld	0.01	NA	8.20	25.56	16.33	3.55	2.43	0.48	0.03	0.07	0.92	0.00	bld	0.09	98.85
		26.76	0.00	0.20	12.50	bld	0.72	0.00	0.02	0.03	NA	12.27	29.67	11.68	3.11	1.41	0.27	0.00	0.01	0.43	bld	bld	0.04	99.08
	m7	24.32	0.17	0.34	11.24	0.02	0.74	bld	0.01	0.01	NA	10.17	24.83	11.68	2.79	1.50	0.38	0.02	0.04	0.56	bld	bld	bld	88.72
		26.16	0.15	0.26	12.08	0.03	0.82	bld	0.01	0.02	NA	10.23	26.97	13.64	3.21	1.84	0.41	0.04	0.06	0.71	bld	bld	bld	96.60
		25.94	0.21	0.43	11.68	0.05	0.99	0.01	0.00	0.02	NA	9.81	26.90	13.64	3.15	1.83	0.40	0.02	0.05	0.70	0.00	0.01	bld	95.77
		23.19	0.44	0.23	9.77	0.03	0.66	0.02	0.01	0.01	NA	11.74	27.28	12.00	2.96	1.39	0.27	bld	0.02	0.49	bld	bld	bld	90.17
		26.61	0.03	0.54	12.01	0.07	1.70	bld	0.06	0.04	NA	9.82	26.81	13.71	3.23	1.72	0.35	0.03	0.04	0.59	bld	bld	0.05	97.37
66mf_7	m1	27.00	0.82	0.34	12.34	0.02	0.87	bld	bld	bld	NA	12.50	27.02	10.42	3.13	0.87	0.09	bld	0.03	0.24	bld	bld	0.18	95.69
	m4	27.20	0.26	bld	12.95	bld	0.93	0.43	6.84	0.60	NA	10.21	22.19	9.48	2.58	1.78	bld	0.17	0.68	1.39	0.16	0.04	1.98	99.83
		27.48	0.26	bld	13.12	bld	0.95	0.44	7.02	0.62	NA	10.36	22.16	9.46	2.63	1.74	bld	0.16	0.66	1.39	0.15	0.04	2.03	100.63
	m3	26.98	0.07	bld	12.98	bld	0.76	0.67	2.70	1.41	NA	11.46	24.08	11.41	2.95	2.02	0.05	0.12	0.31	1.42	0.01	0.00	0.42	99.78
		26.92	0.08	bld	13.00	bld	0.76	0.66	2.76	1.37	NA	11.45	23.60	11.25	2.87	2.00	0.04	0.14	0.34	1.52	0.02	0.01	0.46	99.22
		27.08	0.09	bld	13.10	bld	0.74	0.65	2.70	1.34	NA	11.40	23.91	11.33	2.88	1.99	0.04	0.14	0.33	1.47	0.02	bld	0.48	99.62
		26.95	0.09	bld	12.97	bld	0.74	0.64	2.63	1.32	NA	11.65	24.00	11.31	2.86	1.97	0.03	0.15	0.34	1.50	0.01	bld	0.46	99.56
		27.09	0.11	bld	13.05	bld	0.75	0.63	2.59	1.38	NA	11.54	24.06	11.54	2.92	2.05	0.03	0.12	0.26	1.44	0.01	bld	0.36	99.90
	m5a	25.77	1.06	0.08	11.21	0.01	0.22	1.07	8.30	0.19	NA	12.06	23.61	9.28	2.56	1.54	0.02	0.07	0.19	0.93	0.02	bld	0.36	98.53
		25.79	1.10	0.09	11.12	0.02	0.31	0.84	8.12	0.19	NA	12.32	23.72	9.20	2.57	1.52	0.01	0.07	0.19	0.91	0.01	bld	0.41	98.51
	m5b	26.71	0.33	0.02	12.58	bld	0.72	0.85	5.69	0.29	NA	12.05	23.84	9.00	2.54	1.69	0.05	0.11	0.38	1.19	0.06	bld	0.89	98.97

Table A1 continued

Sample	Grain	O	Si	S	P	K	Ca	Pb	Th	U	Fe	La	Ce	Nd	Pr	Sm	Eu	Tb	Dy	Gd	Er	Yb	Y	TOTAL
66mf_11	m1*	25.80	0.42	0.10	11.66	0.04	0.20	bld	bld	bld	0.56	13.58	30.11	10.10	2.90	0.71	0.08	bld	bld	0.15	bld	bld	bld	96.18
		26.14	1.08	0.15	11.55	0.00	0.27	bld	0.01	bld	1.01	12.83	28.48	9.44	2.66	0.62	0.05	bld	bld	0.10	bld	bld	0.03	94.21
		25.49	0.89	0.20	10.27	0.06	0.33	0.00	0.07	bld	5.08	11.96	26.50	8.81	2.44	0.61	0.05	bld	bld	0.05	bld	bld	bld	92.62
		26.68	0.72	0.11	12.16	0.09	0.21	bld	bld	bld	0.63	13.47	29.40	9.89	2.83	0.71	0.05	bld	bld	0.14	bld	bld	bld	96.96
	m2	25.94	0.55	0.07	12.01	bld	0.56	0.06	2.68	0.05	NA	15.00	28.03	7.36	2.41	0.28	bld	0.01	bld	0.34	bld	bld	0.04	95.21
		26.45	0.08	0.06	12.54	bld	0.14	0.00	0.41	bld	NA	19.16	32.18	4.80	2.03	0.09	bld	bld	bld	bld	bld	bld	bld	97.83
		26.36	0.13	0.08	12.40	0.00	0.20	0.01	1.01	0.00	NA	17.08	31.86	6.21	2.32	0.16	bld	0.01	0.00	0.05	bld	bld	bld	97.83
		27.11	0.09	0.05	12.88	0.04	0.13	0.01	0.41	0.01	NA	19.17	32.93	5.07	2.11	0.12	0.00	0.03	0.01	0.03	bld	0.01	bld	100.18
		26.66	0.06	0.03	12.75	0.02	0.09	bld	0.14	0.00	NA	23.38	30.64	3.02	1.46	0.03	0.00	0.02	bld	bld	bld	0.01	bld	98.24
		26.51	0.08	0.05	12.62	0.01	0.14	0.01	0.39	bld	NA	18.04	31.98	5.63	2.22	0.15	bld	0.01	0.01	0.03	bld	0.02	bld	97.84
		26.79	0.15	0.04	12.78	0.00	0.11	bld	0.44	bld	NA	19.40	32.19	4.46	1.95	0.10	0.02	0.02	0.02	0.05	bld	0.02	bld	98.45
		26.54	0.09	0.03	12.68	0.02	0.05	bld	0.21	0.01	NA	23.93	30.74	2.20	1.20	bld	bld	0.01	bld	bld	bld	0.01	bld	97.60
	m4	26.34	0.26	0.06	12.50	0.08	0.12	0.00	0.60	0.01	NA	18.67	31.40	4.33	1.93	0.05	bld	bld	bld	bld	bld	bld	0.08	96.32
		26.80	0.23	0.03	12.83	0.05	0.09	bld	0.33	bld	NA	20.93	31.38	3.44	1.63	0.02	bld	bld	bld	bld	bld	0.00	0.04	97.70
		26.25	0.55	0.04	12.27	0.11	0.14	0.03	0.82	0.01	NA	17.46	30.78	5.19	2.08	0.13	bld	bld	bld	bld	bld	bld	0.07	95.79
		26.08	0.37	0.04	12.10	0.07	0.25	0.02	1.86	0.01	NA	21.05	29.87	3.44	1.58	0.03	bld	bld	bld	bld	bld	bld	0.03	96.66
		26.44	0.33	0.06	12.52	0.01	0.23	bld	0.73	bld	NA	17.52	30.51	5.83	2.15	0.21	0.01	0.00	bld	0.03	bld	bld	0.01	96.50
	m6	26.23	0.26	0.13	12.43	bld	0.38	bld	2.13	bld	NA	13.08	28.59	9.54	2.92	1.09	0.03	0.03	0.05	0.27	bld	0.02	0.05	95.82
		21.67	1.13	0.06	8.76	bld	1.25	bld	17.23	bld	NA	9.48	20.01	6.21	1.80	0.48	bld	bld	bld	0.04	bld	bld	bld	86.21
Moacyr SecStd		26.57	0.54	0.02	12.28	bld	0.32	0.14	5.83	0.12	NA	12.32	24.87	9.45	2.77	1.58	bld	0.06	0.20	0.76	0.02	0.02	1.00	98.86
		26.59	0.55	0.02	12.26	bld	0.33	0.14	5.85	0.13	NA	12.34	24.87	9.40	2.78	1.60	bld	0.06	0.21	0.76	0.04	0.02	1.07	99.01
		26.58	0.57	0.02	12.25	bld	0.32	0.14	5.81	0.12	NA	12.46	24.91	9.47	2.78	1.60	bld	0.06	0.20	0.76	0.03	0.01	0.94	99.00
		26.62	0.54	0.02	12.29	bld	0.32	0.14	5.82	0.12	NA	12.41	24.87	9.53	2.76	1.59	bld	0.05	0.20	0.75	0.04	0.01	0.98	99.05
		26.59	0.53	0.02	12.27	bld	0.32	0.14	5.87	0.12	NA	12.43	24.88	9.47	2.75	1.59	0.01	0.06	0.21	0.75	0.03	0.01	1.01	99.08
		26.46	0.54	0.02	12.20	bld	0.32	0.14	5.83	0.11	NA	12.36	24.95	9.42	2.80	1.61	bld	0.05	0.19	0.74	0.04	0.02	0.88	98.69
		26.58	0.55	0.02	12.26	bld	0.32	0.14	5.83	0.12	NA	12.36	24.80	9.50	2.78	1.59	bld	0.06	0.20	0.75	0.02	0.01	1.03	98.92
		26.62	0.56	0.02	12.28	bld	0.33	0.14	5.87	0.12	NA	12.37	24.85	9.52	2.79	1.61	0.01	0.05	0.21	0.73	0.02	0.01	0.97	99.08
		26.63	0.55	0.02	12.23	bld	0.32	0.14	5.81	0.11	NA	12.73	25.01	9.48	2.79	1.59	0.01	0.05	0.21	0.78	0.04	0.00	1.00	99.49
		26.57	0.54	0.02	12.20	bld	0.33	0.14	5.80	0.11	NA	12.75	24.94	9.42	2.81	1.57	0.01	0.06	0.21	0.76	0.03	0.01	1.00	99.28
		26.58	0.54	0.02	12.20	bld	0.33	0.14	5.80	0.11	NA	12.66	24.98	9.55	2.79	1.60	0.02	0.07	0.22	0.76	0.03	0.02	1.00	99.40
		26.64	0.54	0.02	12.25	bld	0.32	0.14	5.82	0.10	NA	12.71	25.00	9.50	2.77	1.58	0.02	0.07	0.21	0.74	0.02	0.02	1.00	99.47
		26.58	0.54	0.02	12.21	bld	0.32	0.14	5.81	0.10	NA	12.73	24.98	9.45	2.81	1.60	0.02	0.06	0.21	0.76	0.04	0.02	1.00	99.39
		26.53	0.54	0.02	12.17	bld	0.32	0.14	5.82	0.10	NA	12.65	24.95	9.48	2.79	1.60	0.01	0.07	0.22	0.75	0.03	0.02	1.00	99.21
		26.64	0.55	0.02	12.25	bld	0.32	0.14	5.83	0.10	NA	12.71	24.98	9.54	2.76	1.58	0.02	0.06	0.21	0.76	0.03	0.00	1.01	99.51
		26.63	0.54	0.02	12.25	bld	0.32	0.14	5.82	0.10	NA	12.67	24.91	9.48	2.78	1.62	0.00	0.05	0.21	0.77	0.04	0.02	1.00	99.37
		26.62	0.55	0.02	12.24	bld	0.33	0.14	5.81	0.12	NA	12.66	24.93	9.46	2.79	1.59	0.01	0.05	0.21	0.75	0.03	0.02	1.06	99.37
		26.58	0.55	0.02	12.20	0.01	0.32	0.14	5.80	0.12	NA	12.70	24.87	9.54	2.76	1.61	0.01	0.06	0.21	0.76	0.04	0.01	1.05	99.36
		26.59	0.55	0.02	12.19	0.02	0.33	0.14	5.83	0.12	NA	12.65	24.98	9.48	2.77	1.59	0.01	0.06	0.20	0.75	0.04	0.01	1.06	99.40
		26.61	0.55	0.02	12.25	0.01	0.32	0.14	5.81	0.12	NA	12.54	24.88	9.52	2.75	1.61	0.02	0.05	0.20	0.74	0.04	0.01	1.06	99.26
		26.37	0.53	0.02	12.15	bld	0.32	0.14	5.78	0.11	NA	12.46	24.60	9.53	2.73	1.57	0.02	0.05	0.21	0.75	0.04	0.01	0.99	98.36
		26.41	0.52	0.02	12.18	bld	0.32	0.14	5.76	0.11	NA	12.45	24.75	9.52	2.75	1.54	0.01	0.06	0.21	0.74	0.03	0.01	0.99	98.51
		26.34	0.53	0.02	12.16	bld	0.33	0.14	5.77	0.12	NA	12.32	24.60	9.50	2.72	1.55	0.01	0.06	0.22	0.74	0.03	0.00	0.99	98.14
		26.32	0.52	0.02	12.14	bld	0.32	0.14	5.79	0.12	NA	12.38	24.62	9.40	2.73	1.56	0.02	0.05	0.21	0.77	0.03	0.00	0.99	98.11
		26.42	0.53	0.02	12.19	bld	0.33	0.14	5.80	0.11	NA	12.46	24.62	9.45	2.72	1.61	0.01	0.05	0.21	0.75	0.03	0.02	1.00	98.45
		26.45	0.53	0.02	12.19	bld	0.33	0.14	5.79	0.12	NA	12.51	24.62	9.49	2.77	1.58	0.01	0.05	0.21	0.77	0.03	0.01	1.00	98.63

Appendix B. Additional Photomicrographs

Figure A1. Mutual Formation and contact with the Browns Hole Formation. (A) XPL image of sample AP17_79MF_21, taken from the lowest accessible outcrop of the Mutual Formation. Central grain is a mottled feldspar surrounded by quartz grains with quartz overgrowths. Note the fine-grained clay cement and hematite dust rims. (B) XPL image from the same sample showing several quartz triple junctions. (C) XPL and PPL (inset) images of Mutual Formation sample AP17_66MF_4, from near the contact between the Mutual and Browns Hole Formations. Note the significantly smaller and more angular grains. (D) Whole thin section image of the contact between the Mutual and Browns Hole Formations.

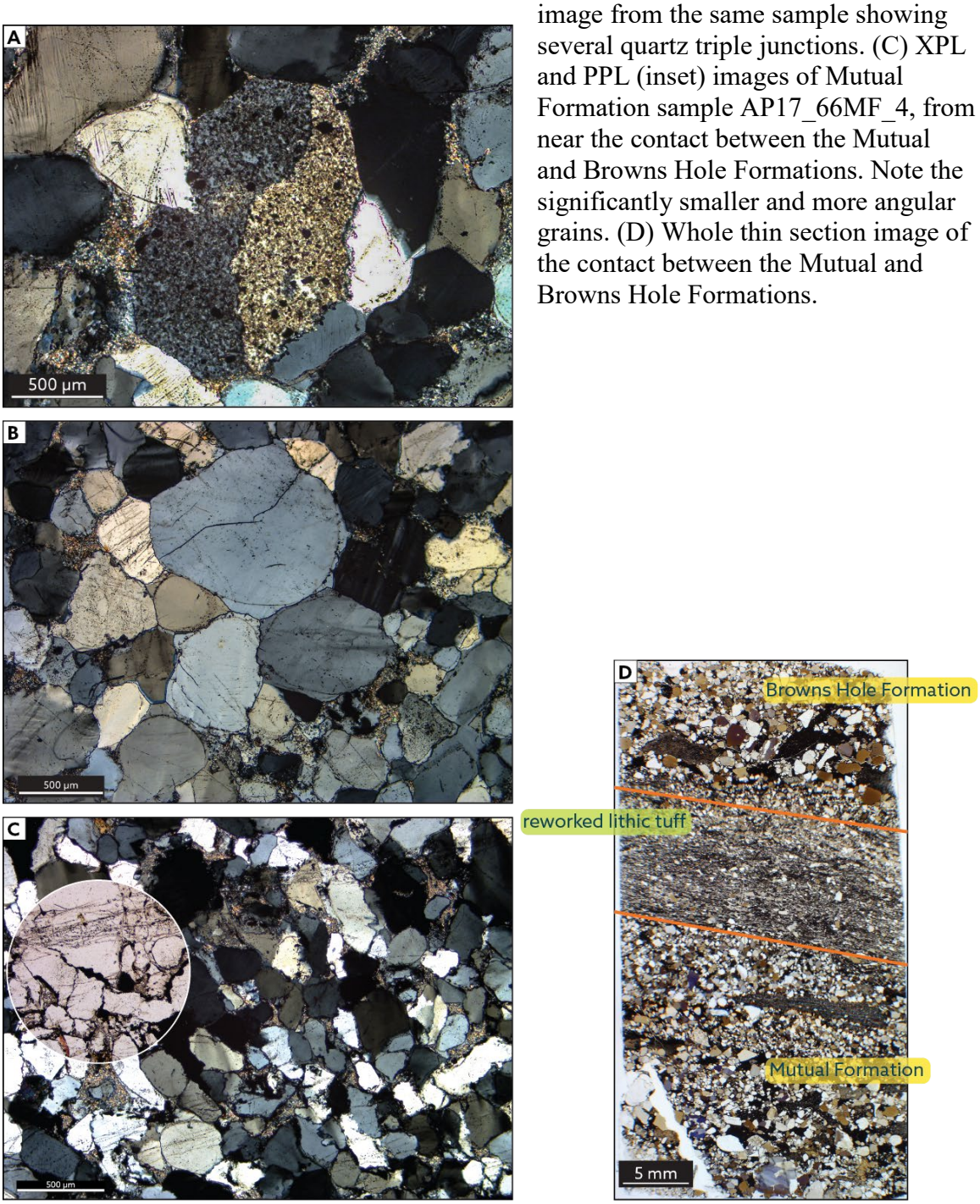

Appendix B continued

Figure A2. Examples of sericitized feldspars in the Browns Hole Formation. (A) From volcaniclastic sandstone sample AP17_66MF_8, large volcanic clast with fine-grained clays pseudomorphic to feldspar laths. (B) Zoomed image of the same grain showing the partial replacement of feldspar grains by fine-grained clays.

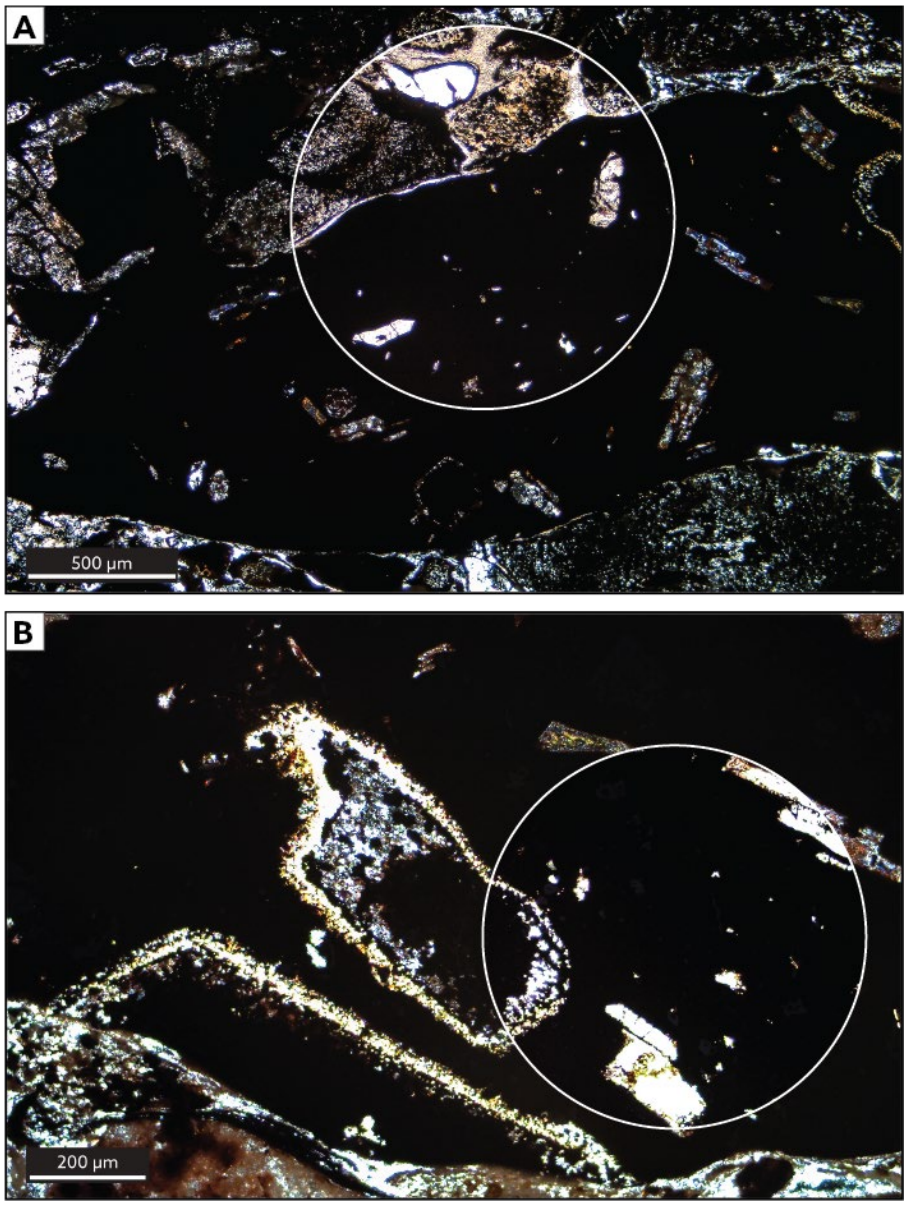

Appendix B continued

Figure A3. Basalt flow capping the volcanic member of the Browns Hole Formation. (A) full thin section image. Note the vesicles lined with feldspar, hematite, and filled with quartz. (B) XPL image of the feldspar groundmass with irregular pockets of fine-grained clay and hematite. (C) XPL and PPL (inset) of another area of the groundmass showing rounded pockets of feldspar, reminiscent of lapilli, that are lined with fine-grained hematite.

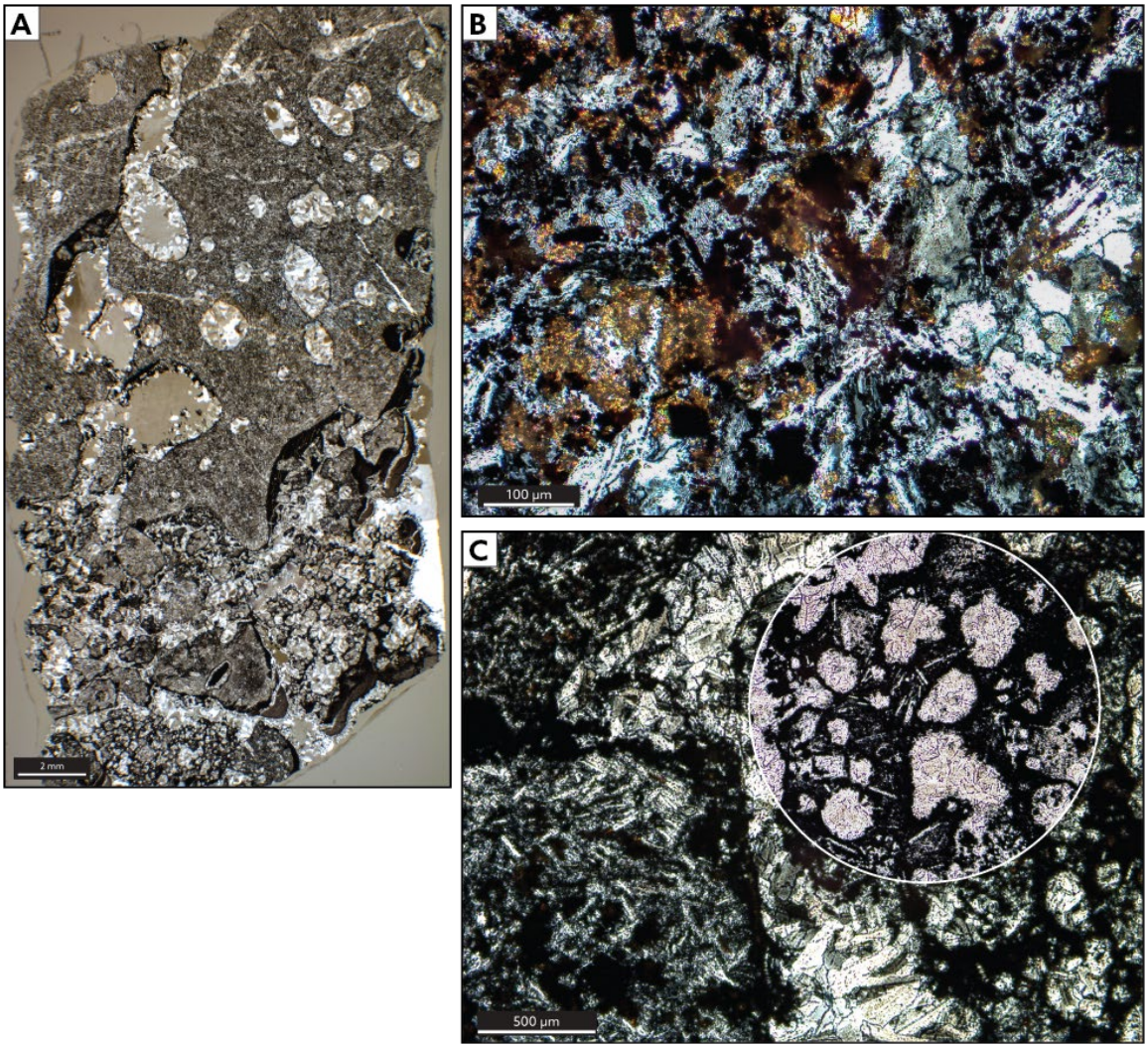

Appendix B continued

Figure A4. Iron-oxide cement in the Terracotta member of the Browns Hole Formation. XPL and PPL (insets) thin section images of sample AP17_66MF_14, from the Terracotta member of the Browns Hole Formation. (A) Fine-grained, dendritic iron-oxide cement, surrounding rounded quartz grains. (B) Fine-grained iron oxide cement lining sub-rounded quartz grains. Note the fractures in several quartz grains that are filled with fine-grained iron-oxide cement.

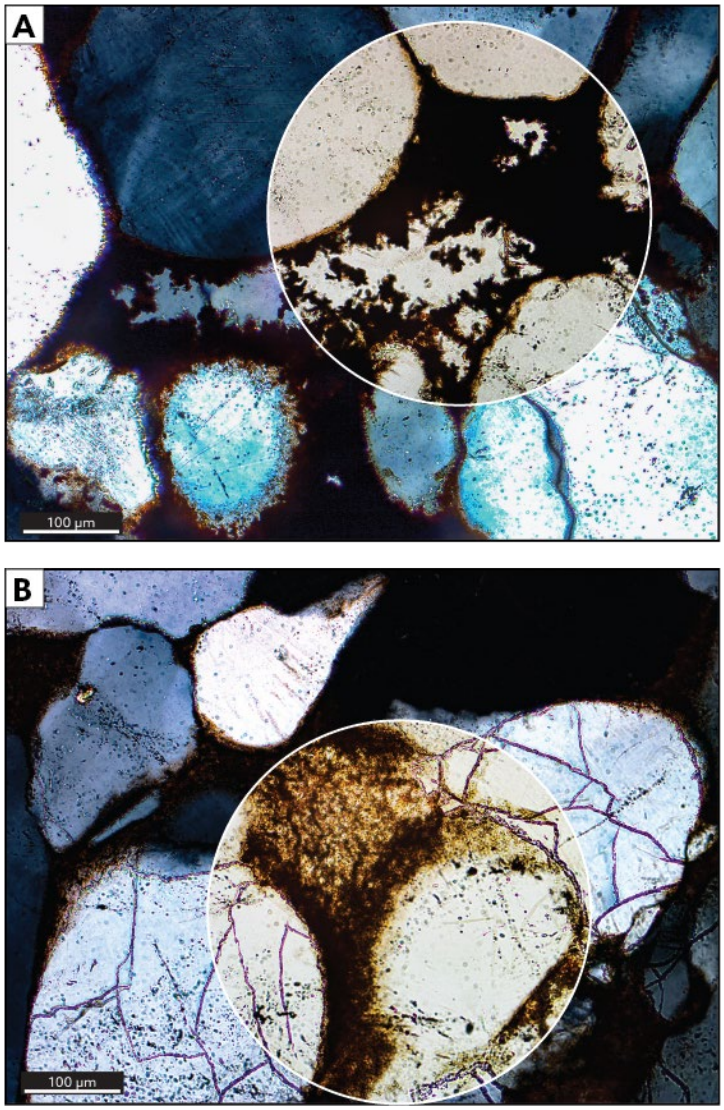

Appendix B continued

Figure A5. Abundant clay cement in the Geertsen Canyon Formation. (A) Sub-rounded quartz grains surrounded by fine-grained cements. Note the cracked quartz grains filled with fine-grained clay. (B) Partially degraded feldspar grain surrounded by and infilled with fine-grained clay cements. (C) More intact but mottled feldspar grain still surrounded by fine-grained clays. Note, in all three images, the appearance of more sutured quartz grains compared to sandstone samples from the Mutual and Browns Hole formations.

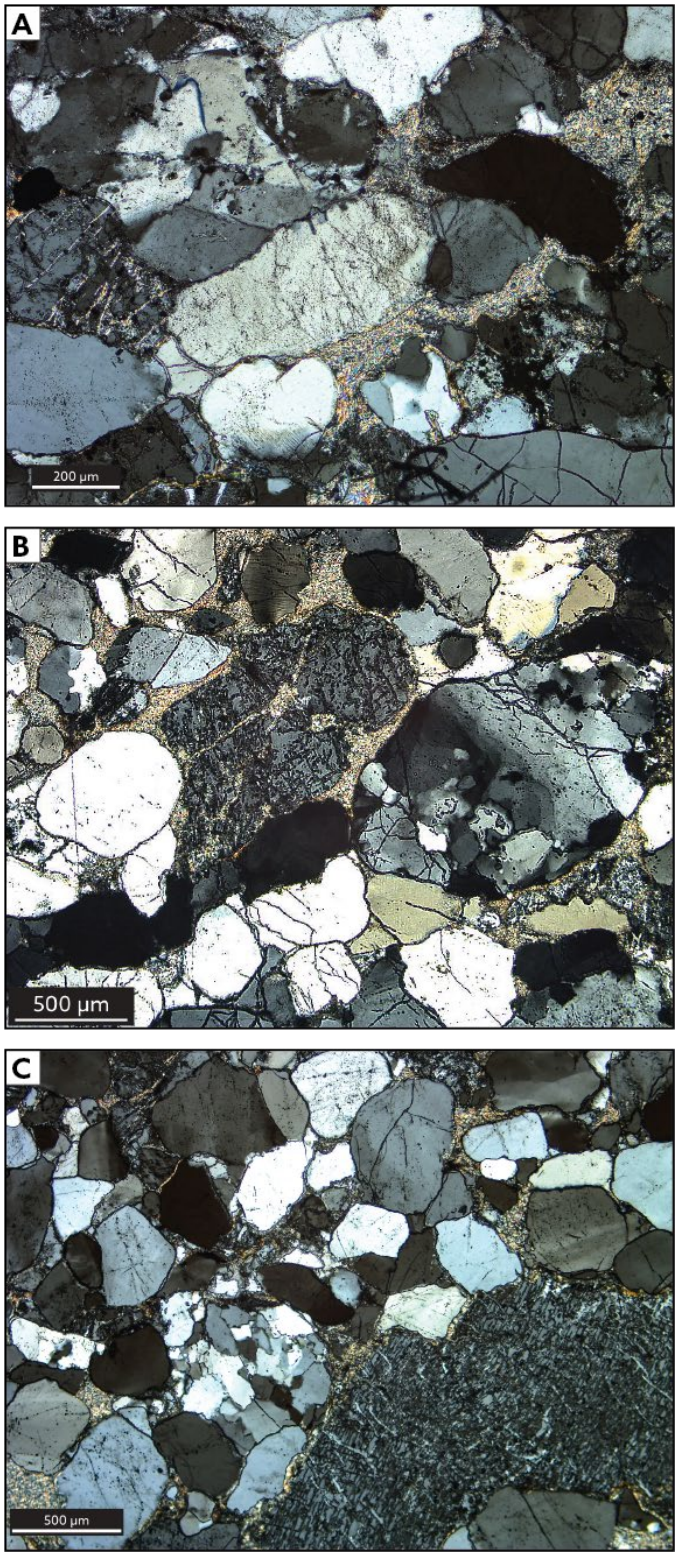

Appendix C. Additional BSE images of monazite grains

Figure A6. BSE images of additional monazite grains. (A) Group 1 monazite grain (m3; white) from sample AP17_66MF_5 found between quartz grains (dark grey) with hematite cement (medium grey) and titanite grain (light grey). (B) Also from sample AP17_66MF_5, Group 3 detrital monazite (m4) entirely encased in an angular, pitted quartz grain. (C) Euhedral Group 1 monazite grains (m5) from the same sample. Grains are surrounded by fine-grained clays. (D) Euhedral Group 1 monazite grains (m6) surrounding an angular, pitted quartz grain in the same sample. (E) Additional example of euhedral monazites (m7) surrounding an angular, pitted quartz grain from the same sample. (F) Small, Group 2 monazite grains (m5) from sample AP17_66MF_11 surrounded by fine-grained clays and adjacent to a partially degraded feldspar grain.

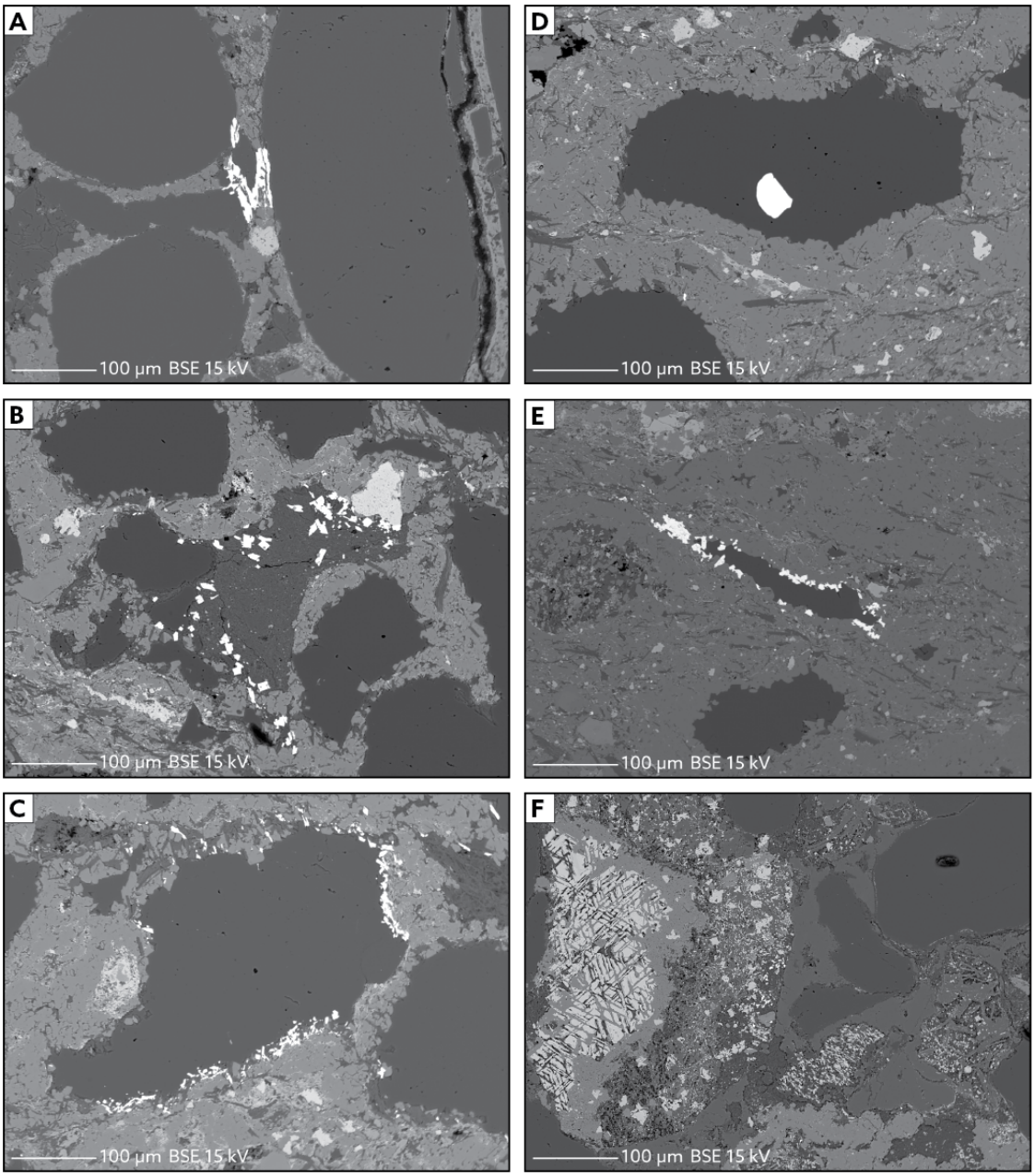

Appendix D. PHREEQC input file
Used with Lawrence Livermore National Laboratory database (llnl.dat)

```
SOLUTION 1 Pure Water
    temp      25
    pH        7
    pe        4
    redox     pe
    units     mmol/kgw
    density   1
    -water    1 # kg

EQUILIBRIUM_PHASES 1
    CO2(g)    -1.0 10

SAVE SOLUTION 1
END

REACTION_TEMPERATURE 1
    25 200 in 5 steps
EQUILIBRIUM_PHASES 2
    Albite    0 10
    K-feldspar 0 10
    Quartz    0 10
    Hematite  0 10
    Tremolite 0 10

USE Solution 1
```